Laboratory Experiments of High-Energy-Density Shocks in Magnetized Supersonic Plasma Flows

by

Rishabh Datta

Submitted to the Department of Mechanical Engineering
in partial fulfillment of the requirements for the degree of

Master of Science in Mechanical Engineering

at the

MASSACHUSETTS INSTITUTE OF TECHNOLOGY

February 2022

Author . . . .
Department of Mechanical Engineering
15 January, 2022

Certified by . . . .
Jack D. Hare
Assistant Professor, Department of Nuclear Science and Engineering
Thesis Supervisor

Certified by . . . .
Ahmed F. Ghoniem
Ronald C. Crane Professor, Department of Mechanical Engineering
Thesis Reader

Accepted by . . . .
Nicolas Hadjiconstantinou
Graduate Officer, Department of Mechanical Engineering

Laboratory Experiments of High-Energy-Density Shocks in Magnetized Supersonic Plasma Flows

by

Rishabh Datta

Submitted to the Department of Mechanical Engineering
on 15 January, 2022, in partial fulfillment of the
requirements for the degree of
Master of Science in Mechanical Engineering

Abstract

Magnetized shocks are of interest in many astrophysical environments, in which high Mach number flows interact with ambient media, planetary obstacles, and/or spacecraft to generate strongly radiating shocks. Some examples include extrastellar jets from radio galaxies, relativistic jets from quasars and blazars, Herbig-Haro jets from Young Stellar Objects, and shocks in core-collapse supernovae and supernova remnants. In this study, we mimic these extreme astrophysical environments using pulsed-power driven high-energy-density-plasma laboratory experiments, by generating hypersonic, magnetized large-Reynolds' number plasma flows, using exploding z-pinch wire arrays on the MAGPIE facility (1.4 MA peak current, 250 ns rise time). Plasma flows from adjacent wire cores expand and generate oblique shock structures, resulting in modulation of the plasma flow. These flows collide with inductive probes placed in the flow, which serve both as the obstacles that generate the magnetized bow shocks, and as diagnostics of the advected magnetic field. The oblique shocks, which are represented by oblique discontinuities in electron density, are observed to exhibit hollow density profiles. A detached bow shock forms ahead of the probe and exhibits a fully 3D structure, with a larger opening angle in the plane parallel to the magnetic field, than in the plane normal to it. We use the shock Mach angle to determine the upstream Mach number ($5-8$) of the flow. We also introduce a novel technique to estimate the flow velocity and temperature of pulsed-power driven plasmas, via simultaneous imaging of inductive probes and measurement of the inductive probe signal. The velocity and temperature estimated using this method are consistent with values reported in literature. Experimental results are compared with full 3D simulations performed using the resistive MHD code GORGON, and synthetic Thompson scattering spectra are generated, which form the basis of future experiments.

Thesis Supervisor: Jack D. Hare
Title: Assistant Professor, Department of Nuclear Science and Engineering

Acknowledgments

I would like to thank my advisor, Jack D. Hare, for the his advice, support and guidance. I am also grateful to Sergey Lebedev, Danny Russell, Iek Lee, and Thomas Clayson at the MAGPIE facility at Imperial College London, where the data presented in this thesis was collected. I am also thankful to Jerry P. Chittenden for use of the GORGON code for simulations presented in this thesis. I would also like to thank Prof. Ahmed F. Ghoniem, for serving as reader for the thesis.

Finally, I am grateful to my friends and family for their support during this process.

Contents

1 Introduction 23

1.1 Shocks in Astrophysical Plasmas . . . 26

1.2 Laboratory Astrophysics Shock Experiments . . . 27

1.3 Outline of Thesis . . . 32

2 Magnetohydrodynamic Shocks 33

2.1 Preliminary Equations . . . 33

2.2 Linear MHD Waves . . . 35

2.3 MHD Shock Jump Conditions . . . 37

2.4 Hydrodynamic Shocks . . . 39

2.4.1 Normal Shock . . . 39

2.4.2 Oblique Shock . . . 40

2.4.3 Bow Shocks . . . 42

2.5 MHD Shocks . . . 43

2.5.1 Parallel Shocks . . . 43

2.5.2 Perpendicular Shocks . . . 44

2.5.3 Oblique MHD Shocks . . . 46

2.5.4 MHD Bow Shocks . . . 49

2.6 Mach Wave . . . 50

2.7 Adiabatic index of a plasma . . . 53

2.8 Summary of MHD Shocks . . . 55

3 Pulsed Power and Z-pinch Wire Arrays 57

3.1 Pulsed Power Generators 57

3.2 Wire Array Z-Pinches 60

3.2.1 Rocket Model of Mass Ablation 64

3.3 Resitive MHD Simulations of Wire Arrays 65

3.4 Diagnostics 68

3.4.1 Inductive Probes 68

3.4.2 Laser Interferometry 69

3.4.3 Optical Thompson Scattering 74

3.5 Summary of Pulsed-Power Machines and Z-Pinch Wire Arrays 78

4 Bow Shocks in Supersonic Super-Alfvénic aluminum Plasma 81

4.1 Experimental and Diagnostic Setup 82

4.1.1 Inductive Probes 83

4.1.2 Laser Interferometry 84

4.2 Electron Density Measurements and Shock Morphology 85

4.3 Magnetic Field Measurements 88

4.4 Comparison with Simulation 91

4.5 Future Work 96

4.5.1 Shadowgraphy and Schlieren Imaging 96

4.5.2 Optical Thompson Scattering 96

4.6 Summary 98

5 Oblique Shocks in Inverse Z-Pinch Wire Arrays 101

5.1 Experimental and Diagnostic Setup 101

5.2 Oblique Shock Morphology 102

5.3 Comparison with Simulation 108

5.4 Summary and Future Work 110

6 Conclusions 113

A Derivation of the Electromagnetic Wave Dispersion Relation in Plasmas 117

B Derivation of the Thompson scattering Spectral Density Function 125

B.1 Scattered Power Spectrum 125
B.2 Spectral Density Function 128
B.3 Electric Susceptibility 131
B.4 Thompson Scattering Summary 133

List of Figures

1-1 Shadowgraph of a bullet travelling supersonically through air (Davidhazy [2015]). A detached curved shock front is visible ahead of the obstacle. Adapted from Davidhazy [2015], An Overview of High Speed Photographic Imaging. 24

1-2 Convective steepening of a pressure pulse. 25

1-3 (a) Twin jets from a young stellar object HH111 [Nasini, 2021]. The hypersonic outflows from the young star are characterized by a string of radiating "knots", which are conical or oblique internal shocks generated due to the collision of material moving at different speeds. Image courtesy of ESA/Hubble NASA. (b) Artist's illustration of relativistic jets from a supermassive blackhole [Chiaberge, 2015]. Extragalactic jets typically terminate in a bow shock, where the hypersonic outflows impinge on the ambient media. Image courtesy of NASA,ESA STScl. 26

1-4 3D representation of an exploding wire array, which is commonly used as a plasma source in pulsed-power plasma experiments. 28

2-1 Friedrichs I diagrams representing the normalized phase velocity of fast (black line), slow (blue line), and Shear Alfvén (red line) waves as a function of the angle of propagation relative to the magnetic field. Note that the phase velocity is normalized using the magnetosonic wave speed V_{MS}. (a) Friedrichs I diagram for $C_S/V_A = 1$. The fast wave phase velocity varies from a maximum of V_{MS} perpendicular to the magnetic field, to a minimum velocity, equal to the higher of the sound and Alfvén speeds, along the magnetic field. The slow wave does not propagate perpendicular to the magnetic field, and has a maximum velocity, equal to the lower of the sound and Alfvén speeds, along the magnetic field. The shear Alfvén wave propagates at the Alfvén speed along the magnetic field, and does not propagate perpendicular to the field. (b) Friedrichs I diagram for $C_S/V_A = 0.25$. The fast wave speed is approximately isotropic and approaches the Alfvén speed. (c) (b) Friedrichs I diagram for $C_S/V_A = 4$. The fast wave speed is approximately isotropic and approaches the sound speed. 37

2-2 (a) Hydrodynamic oblique shock geometry. The upstream velocity vector is defected by an angle ϕ across the shock front. The shock front forms at an angle σ to the upstream velocity vector. (b) Shock angle as a function of defection angle for different upstream Mach number M_1. The shock angle can vary between $\pi/2$ (normal shock) and the Mach angle (Mach shock). For a given defection angle, there are two possible solutions - weak shock and strong shock - for the shock angle. (c) Detached bow shock ahead of a blunt obstacle. The bow shock represents an oblique shock with varying shock and deflection angles. The shock is strongest at the nose, where the shock angle is 90^o; this constitutes a normal shock. Far away from the obstacle, the shock becomes an infinitesimally weak Mach shock. 41

2-3 Types of MHD shocks (a) Parallel shock. The upstream magnetic field is parallel to the shock normal. The magnetic field remains continuous, and the shock is hydrodynamic. (b) Switch on shock. There is no tangential upstream magnetic field, but the downstream magnetic field has a non-zero tangential component. (c) Perpendicular shock. The upstream magnetic field is perpendicular to the shock normal. The downstream magnetic field is compressed. Perpendicular shocks represent super-fast to sub-fast transitions. (d) Slow shock. Slow shocks represent super-slow to sub-slow transitions in which the post-shock magnetic field is deflected towards the shock normal. (e) Intermediate shock. These represent super-Alfvénic to sub-Alfvénic or sub-slow transitions. The magnetic field changes direction across the shock. (f) Fast shock. These represent super-fast to sub-fast transitions. The magnetic field is compressed and deflected away from the shock normal. 44

2-4 (a) Perpendicular shock solution for the compression ratio r and downstream fast Mach number $M_{f,2}$ as a function of the upstream fast Mach number. Entropically permitted shocks are compressive ($r \geq 1$) shocks, which represent super-fast to sub-fast transitions. The compression ratio represents the ratio of the post-shock density and magnetic field to the upstream density and magnetic field. In the strong shock limit ($M_{f,1} \rightarrow \infty$), the compression ratio approaches 4 for $\gamma = 5/3$. The solution is a weak function of the plasma β. (b) Solution of the distilled MHD energy jump condition for $\beta = 0.5$ and $\vartheta_1 = \pi/4$. The $M_{A,1} = M_{A,2}$ line separates entropically permitted solution from the entropically forbidden solutions (red). There are three types of permissible MHD shocks. For Mach numbers larger than point A, we get fast shocks, where the upstream velocity is super-fast and the downstream velocity is sub-fast. Between B and C, we get intermediate shocks, where the upstream velocity is super-Alfvénic and the downstream velocity is sub-Aflvéic or sub-slow. Between C and D, we get slow shocks, where the upstream velocity is super-slow and the downstream velocity is sub-slow. 47

2-5 (a) Fast bow shock ahead of a cylindrical obstacle (De Sterck et al. [1998]). The upstream magnetic field is aligned with the flow and points from the left to the right. The shock front is concave to the cylinder everywhere ahead of the obstacle. (b) Shock front with a dimpled shape. At the nose, the shock is a switch-on shock, which is followed by an intermediate shock. The upper part of the shock represents a fast shock. (c) Bow shock with 2 interacting shock fronts. The leading shock front exhibits fast, intermediate and hydrodynamic parts, while the secondary shock front exhibits intermediate shock transitions. Reprinted from De Sterck et al. [1998] - "Complex magnetohydrodynamic bow shock topology in field-aligned low-flow around a perfectly conducting cylinder. Physics of Plasmas, 5(11), 4015–4027," with permission of AIP Publishing. (d) Optical self-emission images of bow shocks ahead of a conducting cylindrical obstacle (top), and a non-conducting cylindrical obstacle (bottom) (Burdiak et al. [2017]). Flux pile-up ahead of the conducting obstacle creates a bow shock with a larger opening angle and stand-off distance compared to the non-conducting case. Reprinted from Burdiak et al. [2017] - "The structure of bow shocks formed by the interaction of pulsed-power driven magnetised plasma flows with conducting obstacles. Physics of Plasmas, 24(7)," with permission of AIP Publishing 49

2-6 Mach cone in a hydrodynamic fluid. The disturbance, initially at position A, moves with a supersonic velocity u form the left to the right. The disturbance emits spherical sound waves which travel outwards at the sound speed C_S. At some time $t = 2\Delta t$, the disturbance is at position C and has traveled a distance $2u\Delta t$ from its initial position. The tangential surface which connects the spherical wavefronts forms the surface of the Mach cone. 50

2-7 (a) Determination of the Fast Mach angle using Friedrichs I diagram. The velocity circle (dashed line) is centered at $(0, v/2)$. The magnetic field vector makes an angle of $\pi/4$ with the velocity vector. The fast magnetosonic phase-speed (solid black line) has a minimum value along the magnetic field and a maximum value perpendicular to the field. The Mach lines (sold grey lines) are determined by connecting the origin to the points of intersection of the velocity circle and the Friedrichs I diagram. Here, the sound Mach number and the Alfvén Mach number are equal to 3.3. (b) Determination of the Fast Mach angle using Friedrichs II diagram. 51

3-1 Schematic of a pulsed-power machine Magnetically Insulated Transmission Line (MITL) and load setup. The MITL is a coaxial line with a tapering cross-section which delivers the signal from the large-diameter OTL to the load, that sits in a vacuum chamber on top of the MITL. 58

3-2 (a) 3D representation of of an imploding wire array. The global magnetic pressure acts on the outside edge of the wires and causes radially converging flows of plasma. (b) 3D representation of of an exploding wire array. The wires are arranged around a central conductor. The global magnetic pressure acts on the inside edge of the wires and causes radially diverging outflows of plasma. 59

3-3 Current-carrying coronal plasma around the central wire core. 61

3-4 (a) Side-on (r-z plane) view of an exploding wire array. In the derivation of the rocket model, we assume that the wire cores remain stationary and the magnetic pressure accelerates the coronal plasma to a constant velocity V in a thin skin region of width δr. (b) Top (r-θ) view of an exploding wire array. At t= 0s, the total current enclosed within the Amperian loop outside the array is zero, while the current enclosed within the Amperian loop inside the array is non-zero. The net magnetic pressure thus pushes the plasma radially outwards. 63

3-5 Comparison of LTE Thomas-Fermi (TF) and Saha ionziation models with a non-LTE tabulated ionization model for an Aluminum plasma. Darker colors represent increasing ion density. Thomas-Fermi tends to overpredict the ionization state, while the Saha model tends to underpredict the ionization state compared to the nLTE model 67

3-6 Schematic of a simple inductive probe with two oppositely-wound loops of conducting wire. A time-varying magnetic field induces a voltage in a wire loop equal to the time rate of change of the magnetic flux through the loop, which is read by the oscilloscope. 68

3-7 Schematic of a simple Mach-Zehnder interferometer. 70

3-8 (a) Synthetic electron density map. The plasma electron density is modeled as a radially varying Gaussian function with a standard deviation of 50 λ. We have normalized the spatial axis with the probing laser wavelength. (b) Synthetic interferogram in a spatially homodyned system, where there is no misalignment between the probing and reference beams. (c) Background interferogram in the absence of plasma in a spatially heterodyned system. A slight misalignment between the probe and laser beams produces an interference pattern of dark and bright fringes. (d) Synthetic interferogram in the presence of the plasma. The phase introduced by the plasma distorts the pattern of bright and dark fringes. We have ignored any shadowgraphy effects due to density gradients, and any emission and absorption of radiation by the plasma in generating the synthetic interferograms. 72

3-9 (a) Schematic of a simple Optical Thompson Scattering setup. An electromagnetic wave with the wave vector $\mathbf{k_i}$ illuminates the scattering volume. We collect the scattered radiation (which has some wave vector $\mathbf{k_s}$) at an angle θ to the incident wave. The spectrum of the scattered radiation is measured with a spectrometer. (b) A synthetic spectral density function showing well separated ion acoustic peaks. The spectral density function is convolved with the spectrometer response function (a Gaussian function with $\sigma = 2$Å to generate the expected signal. The spectral density function is Doppler shifted due to the velocity of the moving plasma. 75

4-1 Experimental setup showing the exploding wire array and obstacle configuration. (a) End-on (xy-plane) view of the experimental geometry, showing a cylindrical array of 16 equally-spaced 30 µm Al wires around a central cathode. The array diameter is 16 mm and the array height is 16 mm. An inductive probe serves as the obstacle and is placed ~ 5.5 mm from the array surface. The magnetic field lines lie parallel to the end-on plane, and point in the azimuthal direction with respect to the center of the array. (b) Side-on (xz-plane) view of the experimental geometry. In the side-on plane, the magnetic field lines ahead of the obstacle lie perpendicular to the plane, and point out of the page. 82

4-2 (a) Raw end-on interferogram of the experimental set-up the the absence of plasma. This view is illuminated using a 532 nm pulsed Nd-YAG laser. (b) Raw side-on interferogram of the experimental set-up the the absence of plasma. This view is illuminated using a 1053 nm Nd:Glass laser. The probe and reference beams are slightly misaligned to generate a spatially heterodyned system. In the absence of plasma, this creates a linear pattern of bright and dark interference fringes. 84

4-3 (a) End-on spatially heterodyned raw interferogram captured at 300 ns after current start using a Mach-Zehnder interferometry system with a 532 nm laser. The red shaded region is the shadow of the inductive probe, measured by blocking the reference beam and therefore backlighting the inductive probe using the probing laser beam. (b) End-on line-integrated electron density map determined using laser plasma interferometry. (c) Side-on raw interferogram captured at 300 ns after current start using a 1053 nm laser. (d) Side-on line-integrated electron density map determined using laser plasma interferometry. A detached bow shock is visible ahead of the probe in both side-on and end-on views. The shock opening half-angle is larger in the end-on view than in the side-on view. Note that regions in black near the obstacle and the wire array surface represent locations where the probing beam is lost. 86

4-4 Schematic overlay showing bow shock geometry observed ahead of the inductive probe in the end-on view. The shock front is represented by the dashed green line. The opening half-angle is the angle between the obstacle axis and the shock front. The shock angle is the angle between the upstream velocity and the shock front. 87

4-5 Load current and magnetic field measurements from inductive probes. (a) Voltage signal from inductive probes. The grey line represents the signal from the probe located near the magnetically insulated transmission line (MITL). The black line represents the voltage signal from the inductive probe placed in the flow. (b) Normalized load current and the advected post-shock magnetic field. The advected magnetic field is determined from integration of the voltage signal from the probe. (c) Velocity of the plasma at the probe determined from the time of flight of the plasma to the position of the probe. The time of flight is determined from the time interval between the corresponding features on the load and the probe signals respectively, as shown in (a). The blue solid curve is a linear fit through the velocity measurements, and the blue shaded region is the ±1 standard deviation bounds of the fit. 90

4-6 GORGON resistive MHD simulation with an electron density slice of the ablating plasma at 300 ns. A detached bow shock is seen ahead of the obstacle. Note that the left half of the electron density slice is clipped for clarity. 91

4-7 (a) End-on slice of electron density at 300 ns from 3D resistive MHD GORGON simulation of the experimental geometry. (b) End-on line-integrated electron density at 300 ns from 3D resistive MHD GORGON simulation of the experimental geometry. (c) Experimental end-on line-integrated electron density at 300 ns from plasma interferometry (reproduced here from Figure 4-3). In each image, the plasma flow is from the left to the right, and the magnetic field lies in the plane of the page. A bow shock, characterized by a discontinuous increase in electron density, is visible ahead of the obstacle. Far from the obstacle, the opening half-angle in the end-on plane approaches $\approx 21^o$ in the simulation, and $\approx 30^o$ in the experiment. 93

4-8 (a) Side-on slice of electron density at 300 ns from 3D resistive MHD GORGON simulation of the experimental geometry. (b) Side-on line-integrated electron density at 300 ns from 3D resistive MHD GORGON simulation of the experimental geometry. (c) Experimental side-on line-integrated electron density at 300 ns from plasma interferometry (reproduced here from Figure 4-3). In each image, the plasma flow is from the left to the right, and the magnetic field points into the page. A bow shock, characterized by a discontinuous increase in electron density, is visible ahead of the obstacle. Far from the obstacle, the opening half-angle in the side-on plane approaches $\approx 7^o$ in both the simulation and experiment. 93

4-9 (a) Magnetic field lines overlaid on the electron density map generated in GORGON at 300 ns after current start. The magnetic field lines point in the azimuthal direction, and remain mostly unaffected by the shock front, confirming the hydrodynamic nature of the shock. (b) Line-outs of the magnetic field and electron density along the obstacle-axis. The magnetic field exhibits a negligible perturbation at the shock front. 94

4-10 (a) Pile-up of magnetic flux ahead of the 3D obstacle in the end-on plane. The field lines drape around the obstacle, and the magnetic tension of the bent field lines opposes the upstream ram pressure. (b) Pile-up and slipping of magnetic field lines ahead of a 3D obstacle in the side-on plane. Some of the field lines will pile-up ahead of the obstacle, and some will slip past the obstacle. If the obstacle is resistive, magnetic field may also resistively diffuse through it. The accumulation of the magnetic field will depend on the competition between the rates of pile-up, diffusion and slipping 95

4-11 Synthetic optical Thompson scattering spectra generated using simulated properties. (a) Position of the TS collection volumes overlaid onto the simulated electron density slice at 300 ns. (b) Synthetic TS spectral density function at $\theta = 90°$ scattering angle. (c) Synthetic TS spectral density function at $\theta = 135°$ scattering angle. The sythetic spectra show well-defined ion acoustic peaks. We can determine the electron and ion temperatures from the peak separation and peak width respectively, and the velocity along the scattering vector from the Doppler shift of the response. Note that the red solid line represents the spectral density function (black solid line) convolved with the spectrometer response (black dashed line). The spectrometer response is assumed to be a $\sigma = 0.2$Å gaussian function. . . . 97

5-1 End-on (xy-plane) view of the experimental geometry, showing a cylindrical array of 16 equally-spaced 30 µm Al wires around a central cathode. The array diameter is 16 mm and the array height is 16 mm. Collision of the azimuthally expanding plasma from the wire cores results in the formation of oblique shocks between the ablating plasma jets. 102

5-2 (a) End-on line-integrated electron density map obtained from laser interferometry. Oblique shocks form between the ablating plasma jets from the wire cores, and appear as dense regions of post-shock plasma bounded by oblique shock fronts. The oblique shocks exhibit a hollow density profile with high density near the shock fronts and low density near the shock center-line. We use a coordinate system centered on the array axis. (b) Lineouts of the line-integrated electron density along the azimuthal direction at radial distances of R = 12 mm, 12.5 mm and 13 mm from the array center (dashed blue lines in (a)). The electron density rises sharply at the oblique shock fronts. Close to the array (R = 12 mm), the post-shock electron density is mostly uniform, but the density profile becomes hollow at $R \geq 12.5$ mm. 103

5-3 Schematic of the oblique shock geometry with the radial and azimuthal components of the upstream magnetic field. In the limit of small $\alpha/2-\theta$ and $B_r/B_\theta \ll 1$, the upstream magnetic filed is approximately parallel to the shock normal, and the shock becomes a hydrodynamic-like oblique shock. 103

5-4 (a) The upstream velocity makes an angle θ_{u1} with the horizontal, and is deflected by an angle ϕ across the shock front. The tangential velocity remains continuous across the shock front while the normal velocity decreases abruptly, which causes the velocity vector to deflected counter-clockwise away from the horizontal. The shock front forms at an angle σ to the upstream velocity. (b) The upstream velocity makes a negative angle to the horizontal and the magnitude of this angle is $|\theta_{u1}| > \pi/2-\alpha/2$. In this case, the tangential velocity is in the negative direction, and the velocity vector is deflected clockwise away from the horizontal. (c) The upstream velocity makes a negative angle to the horizontal and the magnitude of this angle is $|\theta_{u1}| \le \pi/2-\alpha/2$. In this case, the tangential velocity is in the positive direction, and the velocity vector is deflected counter-clockwise towards the horizontal. 105

5-5 (a) Upstream Mach number as a function of the upstream velocity angle θ_{u1} for the case $\theta_{u2}=0$ and $\alpha/2 \approx 10$ degree. The upstream Mach number for $\gamma = 1$, 1.13 and 5/3 are represented by the blue curves. The deflection and shock angles are represented by the red and black dashed lines respectively. For the given shock geometry, we expect the upstream Mach number to very between $4 < M_1 < 6$ for $\gamma = 1.13$. (b) $\sigma-\phi-M_1$ diagram representing possible upstream Mach number curves for possible values of shock and deflection angles at $\gamma = 1.13$. The blue curves represent the solution of Equation 5.5 for different M_1. The grey line represents the geometric relationship between the shock and deflection angles. Possible solutions of the upstream Mach number can be determined from the points of the grey and blue curves. 107

5-6 (a) Simulated electron density map from 2D resistive MHD GORGON simulation at 300 ns after current start, showing oblique shocks with hollow density profiles. (b) Line-out of the simulated electron density along the azimuthal direction at radial distances of R = 13 mm from the array center. We compare the line-out of electron density from the simulation (red line) with the line-averaged electron density measured using laser interferometry from the experiment (black line). The magnetic field (green line) changes negligibly across the shock fronts. 108

List of Tables

3.1 Characteristic parameters for a pulsed-power driven Aluminum plasma on a ~ 1 MA facility during the ablation phase 62

5.1 Upstream Mach number determined from shock geometry and fluid properties from GORGON simulation. The experimental Mach numbers are calculated for a deflection angle of 5° 110

Chapter 1

Introduction

The vast majority of matter in the visible universe is composed of plasma — a quasi-neutral gas of ions, free electrons, and/or neutrals. Astrophysical plasmas span an impressive range of densities and temperatures, from the relatively cold low-density plasma of planetary ionospheres ($\sim 10^{11}$ particles m^{-3}, $\sim$ 100 K or 10^{-2} eV) and interstellar media ($\sim 10^{6}$ particles m^{-3}, $\sim$ 100 K or 10^{-2} eV) , to the hot dense plasma of stellar cores ($\sim 10^{32}$ particles m^{-3}, $\sim$ 100,000,000 K or 10^{3} eV) (Chen [1974]; Drake [2013]). An important mechanism of mass and energy transfer in astrophysical environments is via hypersonic directed flows of magnetized plasmas (Smith [2012]). The interaction of such high-velocity plasma flows with ambient media or planetary obstacles results in the abrupt dissipation of kinetic energy via shock waves. Due to the ubiquity of high Mach number astrophysical flows, shocks represent a fundamental process in most astrophysical plasmas.

Shocks are defined as internal surfaces of discontinuity in a fluid. Across a shock front, thermodynamic properties (density, temperature, and pressure) and flow properties (velocity) change discontinuously (Anderson [2001]). In a magnetized plasma, the magnetic field advected by the flow may also change discontinuously across the shock front (Goedbloed et al. [2010]). In general, shocks form when a disturbance travels faster than the speed at which compressive perturbations can travel in a medium. In a hydrodynamic fluid, the sound speed determines the speed of propagation of linear perturbations. As such, shocks form when an object travels faster than the sound speed in a given medium (or equivalently, when a supersonic flow collides with a stationary obstacle). For example, Figure 1 shows the bow shock around a bullet travelling supersonically through air (Davidhazy [2015]). When the object travels sub-sonically, sound waves can propagate through the fluid ahead of the object, providing information of the disturbance, and cause adiabatic changes to the fluid. However, when the object travels su-

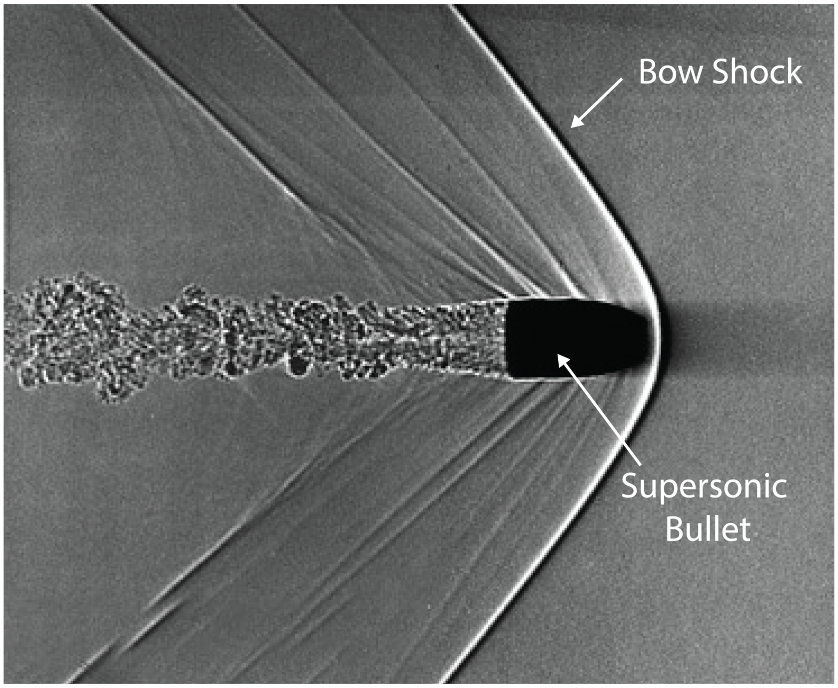

Figure 1-1: Shadowgraph of a bullet travelling supersonically through air (Davidhazy [2015]). A detached curved shock front is visible ahead of the obstacle. Adapted from Davidhazy [2015], An Overview of High Speed Photographic Imaging.

personically, trailing wavefronts can catch up with and overtake the leading wavefronts. Since the fluid cannot receive information of the disturbance before the arrival of the disturbance itself, the fluid will experience a discontinuous non-isentropic change in its thermodynamic properties. In a magnetohydrodynamic (MHD) fluid such as a plasma, linear perturbations can travel at three distinct speeds associated with the three linear MHD waves - the shear Alfvén wave, the fast magnetosonic wave, and the slow magnetosonic wave. These waves are closely associated with the three kinds of shocks possible in an ideal MHD fluid - intermediate, fast, and slow shocks (Goedbloed et al. [2010]).

The wave-steepening picture of shock waves provides an intuitive description of shock formation. A non-linear pressure pulse traveling in a medium will steepen because the local sound speed $C_s \propto p^{(\gamma-1)/\gamma}$ is higher at peak of the pulse. Here, p is the pressure and γ represents the polytropic index. However, the rate of dissipation typically increases with gradients in fluid properties, i.e. $E_{\text{dis}}/\tau \sim D(u/\delta)^2$, where E_{dis} is the energy dissipated over time τ and length scale δ, D is the diffusion coefficient and u is the dissipated fluid quantity. Therefore, pulse steepening results in large gradients which further increase dissipation. The pulse will continue to steepen until dissipative effects are strong enough to balance the convective steepening, resulting in a steady shock front. Therefore, shock formation and the width of the shock are determined by a competi-

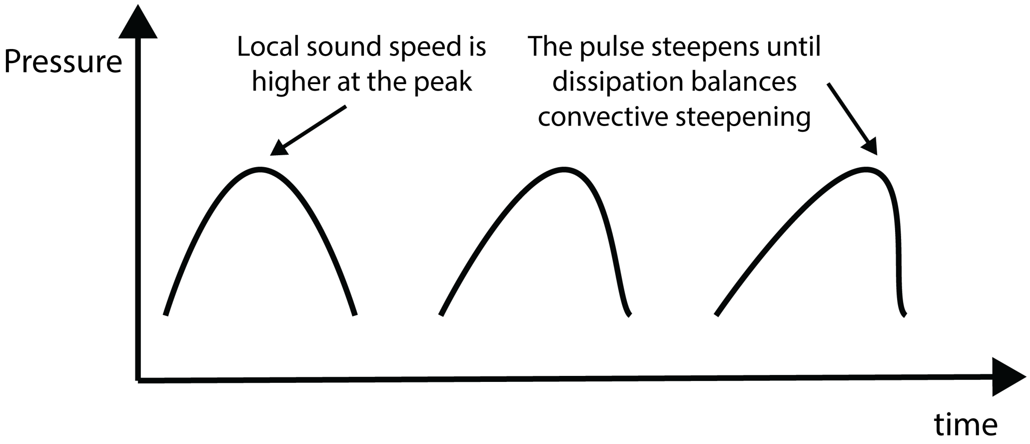

Figure 1-2: Convective steepening of a pressure pulse.

tion between convective steepening and dissipation, and the shock thickness is set by the relevant dissipative length scale. In the fluid framework, dissipative processes which facilitate the shock transition are resistivity $\bar{\eta}$, viscosity ν and thermal conductivity κ, which smooth out gradients in the magnetic field, momentum and temperature respectively. Therefore, we can estimate the width of the shock front by determining the length scale over which dissipated energy becomes comparable to kinetic energy. This is accomplished by setting the Reynolds number $Re = U\delta/\nu$ (for viscous dissipation) or the magnetic Reynolds' number $Re_m = U\delta/\bar{\eta}$ (for resistive dissipation) to order unity.

The dissipative length scale ($\delta \sim \nu/U$) is typically comparable a few ion-ion collisional mean free paths $\lambda_{\mathrm{mfp},ii}$. We typically consider the ion-ion mean free path $\lambda_{\mathrm{mfp},ii}$ because ions, which are much more massive than the electrons, carry most of the momentum in the plasma. The shocks in which dissipative processes are responsible for the transition between the upstream and downstream states are called collisional shocks (Boyd and Sanderson [2003]). Since the shock thickness is comparable to the mean free path, the fluid model is not applicable within the shock (a fluid model is applicable when $\lambda_{\mathrm{mfp}}/a << 1$); a kinetic description is required to determine the full evolution of parameters within the shock. Nevertheless, the fluid model can be used to determine the equilibrium states asymptotically upstream and downstream of the shock, where temporal and spatial scales of collision are small enough, such that the velocity distribution is Maxwellian (Goedbloed et al. [2010]).

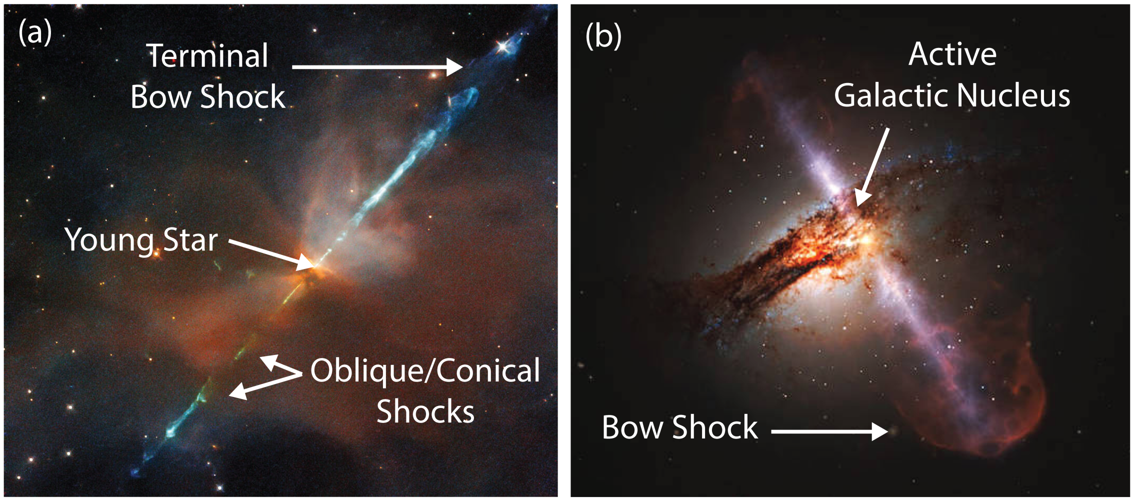

Figure 1-3: (a) Twin jets from a young stellar object HH111 [Nasini, 2021]. The hypsersonic outflows from the young star are characterized by a string of radiating "knots", which are conical or oblique internal shocks generated due to the collision of material moving at different speeds. Image courtesy of ESA/Hubble NASA. (b) Artist's illustration of relativistic jets from a supermassive blackhole [Chiaberge, 2015]. Extragalactic jets typically terminate in a bow shock, where the hypersonic outflows impinge on the ambient media. Image courtesy of NASA,ESA STScl.

1.1 Shocks in Astrophysical Plasmas

Large astrophysical objects can generate high Mach number flows which interact with ambient media, planetary obstacles, and/or spacecraft to generate strongly radiating shocks. Some examples include extrastellar jets from radio galaxies, relativistic jets from Active Galactic Nuclei (AGN) like quasars and blazars, Herbig-Haro (HH) jets from Young Stellar Objects (YSOs), and shocks in core-collapse supernovae and supernova remnants. Such flows can often exhibit dynamically significant magnetic fields, and shock formation in such systems is often accompanied by strong radiative cooling, both hydrodynamic and magnetohydrodynamic (MHD) instabilities, and turbulence, which can significantly modify the shock dynamics (Remington et al. [2006]).

Astrophysical jets, such as those from radio galaxies, AGN or YSOs, often exhibit a string of compact knots (Hartigan et al. [1990]; Smith [2012]). These knots represent regions of intense radiation where the kinetic energy of the jet is abruptly dissipated as heat via shock waves. In HH objects, these knots are called "internal working surfaces", and are thought to be internal oblique or conical shocks generated due to the interaction of flows moving at different velocities within the jet. HH objects also terminate in strongly radiating bow shocks generated due to the interaction of the hypersonic jet with the circumstellar medium (Smith et al. [2003]). Protostellar and HH jets exhibit speeds $\sim 100\,\mathrm{km\,s^{-1}}$, with typical Mach numbers in the range $M_s \sim 10-100$ (Smith [2012]). Similarly, twin jets from radio sources like FRI/FRII galaxies terminate in two distinct lobes, characterized by shocked regions of enhanced radio emission (called ‘hot spots’), where the jet impinges on the extragalactic medium (Smith [2012]). Bends have also been observed in the structure of extrastellar jets (Miley [1980]). The bending of such jets is thought to be facilitated by oblique shocks generated during the interaction of the flow with dense molecular clouds (Smith and Norman [1981];Choi et al. [2007]). Extragalactic jets typically exhibit speeds between $\sim 0.01c - 1c$, with Mach numbers $M_s \sim 1 - 10$ (Duncan and Hughes [1994]; Choi et al. [2007]).

Many hypersonic astrophysical flows, such as flows from YSOs or flows generated by supernovae explosions, represent highly collisional flows, where the collisional mean free path λ_{ii} is small compared to the characteristic length of the plasma (Lebedev et al. [2019]). The flows can be described well using an MHD fluid model, and shocks in such flows can be defined as collisional. In contrast, astrophysical shocks can also be collisionless, i.e. the shock thickness is much smaller than the dissipative length scale. In collisionless shocks, diffusion cannot provide the dissipation required for the transition between the upstream and downstream states, and dispersive effects facilitate this transition (Goldstein et al. [1984]). Examples of collisionless shocks include planetary bow shocks generated due to the interaction of solar wind with the ionospheres, magnetospheres, or atmospheres of planetary obstacles (Russel [1985]; Petrinec and Russell [1997]). Although MHD theory cannot accurately capture the complete physics of collisionless shocks, MHD and hydrodynamic theories have been successfully used to determine the shape and Mach angles of planetary bow shocks in our solar system (Spreiter and Alksne [1969]; Spreiter and Stahara [1985]). Collisionless shocks represent an active area of research in plasma physics. The focus of this thesis, however, is on shocks in collisional laboratory plasmas.

1.2 Laboratory Astrophysics Shock Experiments

The only way to study distant astrophysical shocks is via the radiation that reaches the Earth. Although astronomical observations have provided us with a wealth of information, local direct measurements of relevant quantities like the magnetic field or current are not possible. Moreover, astrophysical plasmas typically exhibit a range of interacting physics, which evolve on extremely large length and time scales. Dynamically similar laboratory experiments allow us to isolate and probe the physics of astrophysical plasmas on comparatively manageable length and time scales. Furthermore, laboratory

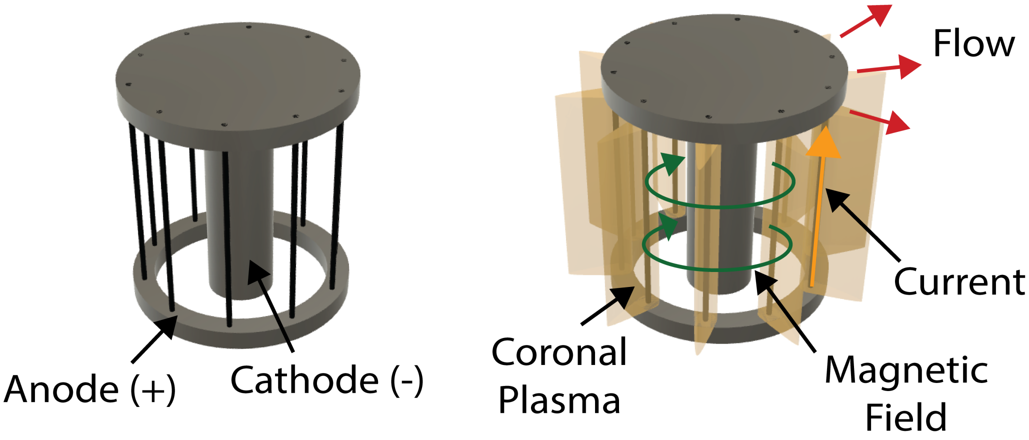

Figure 1-4: 3D representation of an exploding wire array, which is commonly used as a plasma source in pulsed-power plasma experiments.

experiments provide important benchmarks for numerical and theoretical models of astrophysical systems.

Laboratory experiments of shock dynamics are typically performed at high-energy-density (HED) facilities with pulsed-power Z-pinch devices or laser plasmas. High-energy lasers, such as those at the National Ignition Facility (1.8 MJ, Lawrence Livermore National Laboratory) (Miller et al. [2004]) and the OMEGA facility (30 kJ, University of Rochester) (Boehly et al. [1995]), generate HED plasmas ($\sim 10^{25}\,\mathrm{m}^{-3}$, $\sim 100\,\mathrm{eV}$) by depositing large amounts of energy onto small targets. Laser plasmas have been used extensively to study astrophysical shock dynamics, such as the evolution of hydrodynamic instabilities in shocks relevant to supernova explosions (Remington et al. [1997]; Kane et al. [1999]), interaction of shocks with low-density media or clumps relevant to supernova remnants (Drake et al. [1998]; Robey et al. [2002]), and bow shock formation and turbulent interaction of jets with ambient media relevant to YSO jets (Foster et al. [2005]). Laser plasmas, however, typically do not exhibit dynamically significant magnetic fields.

Pulsed-power driven Z-pinch wire arrays provide an excellent platform to study magnetized shocks. Pulsed-power machines generate plasma by applying a large current to a load, typically an array of thin wires, as illustrated in Figure 1-4, over a short period of time. Pulsed-power driven plasmas ($10^{24}\,\mathrm{m}^{-3}, 10\,\mathrm{eV}$) have been used to study physics relevant to YSO jets, such as the interaction of plasma jets with neutral gases (Suzuki-Vidal et al. [2012]; Suzuki-Vidal et al. [2013]), the fragmentation of radiatively-cooled bow shocks in counter-propagating jets (Suzuki-Vidal et al. [2015]), and radiatively-cooled shocks in nested wire arrays (Ampleford et al. [2010]). The ablation of plasma from wire arrays produces highly collisional ($\lambda_{ii}/a << 1$), upstream flows with frozen-in magnetic flux ($Re_m >> 1$) (Suttle et al. [2019]). In a cylindrical wire array, current flows in a thin skin region along the surface of the stationary wire cores, and the global magnetic field acts only in the azimuthal direction. Plasma ablated from the wires is accelerated by the radial $\mathbf{j} \times \mathbf{B}$ force; creating radially converging, or radially diverging (for an inverse wire array) plasma flows, which advect magnetic field and current with them. The plasma flows produced during the ablation phase are typically supersonic, super-Alfvénic, high Reynolds number plasma flows, and their interaction with obstacles of varying geometry have been used to study the behavior of quasi-1D planar shocks (Lebedev et al. [2014]) and quasi-2D bow shocks (Burdiak et al. [2017]; Suttle et al. [2019]; Bott-Suzuki et al. [2015]). In addition, imploding wire arrays have also been used to study oblique shocks generated from the collision of adjacent azimuthally-expanding jets (Swadling et al. [2013]).

Lebedev et al. [2014] studied the formation of a planar magnetized shock due to the interaction of pulsed-power driven (MAGPIE generator peak current = 1.4 MA, rise time = 250 ns) super-fast ($M_f \sim 4.5$), high Reynolds number ($Re_m \sim 50$) Aluminum plasma flows with a planar conducting obstacle. In addition to a thin primary post-shock layer of high density, high temperature stagnated plasma at the obstacle surface, a detached sub-shock was observed to form ahead of the obstacle at a distance comparable to ion inertial length $\sim c/\omega_{\mathrm{pi}}$ (Lebedev et al. [2014]). The detached sub-shock is thought to be a consequence of magnetic flux pile-up in front of the conducting obstacle, and the transition facilitated by two-fluid effects. In the precursor, the ions are unmagnetized ($r_{Li} >> \delta_m$) and the electrons are magnetized ($r_{Le} << \delta_m$). Furthermore, the precursor thickness is comparable to the ion inertial length $\sim c/\omega_{pi}$. The ion and electron fluids decouple over this length, because the electrons, being less massive, can respond to the electric field, but the ions, due to their inertia, cannot. The magnetic pressure decelerates the electrons preferentially. Over time, the ion-electron separation creates a cross-shock electric field, which decelerates the ions at the sub-shock. Similar modification of shock morphology due to magnetic flux accumulation, where two-fluid effects facilitate the shock transition, has been observed in quasi-2D magnetized bow shocks formed from super-fast flows around conducting cylindrical obstacles (Suttle et al. [2019]; Burdiak et al. [2017]).

The orientation of the advected magnetic field relative to the obstacle axis affects bow shock structure (Burdiak et al. [2017]). When the obstacle axis is perpendicular to the advected magnetic field, magnetic draping occurs, i.e. magnetic field lines accumulate and bend near the obstacle. The shape of the resulting bow shock is, thus, modified by the accumulated magnetic flux, and is determined by a competition between the upstream ram pressure and the magnetic tension of the bent field lines. This results in wide bow shocks with large stand-off distance and opening angles, and a relatively small compression ratio of $\rho_2/\rho_1 \sim 2$.

In contrast, when the obstacle axis is parallel to the advected magnetic field, magnetic field lines slip past the obstacle and do not accumulate ahead of the obstacle. The result is a sharp bow shock with a smaller stand-off distance and larger compression ratio $\rho_2/\rho_1 \sim 5$, consistent with an MHD description of shock formation. For dielectric obstacles, the bow shock structure resembles that of the parallel orientation, suggesting that magnetic field diffuses through the resistive obstacle faster than it can accumulate. In addition, no magnetic precursor is observed for conducting obstacles of smaller diameter.

We can predict whether the magnetic field will pile-up from the resistive diffusion time through the obstacle, which is $t_D \sim R^2/\bar{\eta}$, where R is the obstacle length scale, and $\bar{\eta} = \eta/\mu_0$ is the resistive diffusion coefficient. Therefore, we can see that increasing the obstacle resistivity η or decreasing the obstacle size R will result in a smaller diffusion time and prevent magnetic flux accumulation. Suttle et al. [2019] also investigated bow shock formation around magnetized obstacles with private magnetic fields parallel to the advected field. Bow shocks around the magnetized obstacles were observed to have a higher stand-off distance. Additionally, the magnetic pressure near the obstacle was observed to hold off the incoming plasma flow, resulting in low plasma density near the obstacle surface. Although quasi-1D and quasi-2D shocks in magnetized plasmas have been examined extensively, full 3D shocks in magnetized pulsed-power plasmas have received less attention as they require careful diagnosis for proper interpretation.

In this thesis, we investigate oblique shocks and 3D bow shocks in a highly collisional magnetized Aluminum plasma, generated during the ablation phase of an inverse Z-pinch wire array, on the MAGPIE facility (1.4MA peak current, 250 ns rise time, Imperial College London). Ablation of plasma from the wire array generates radially diverging, supersonic, super-Alfvénic flows with frozen-in magnetic flux ($Re_m >> 1$). Plasma flows from adjacent wire cores expand azimuthally and generate oblique shock strictures, resulting in azimuthal modulation of the flow in the end-on plane. These flows collide with inductive probes placed in the flow, which serve both as the obstacles that generate the magnetized bow shocks, and as diagnostics of the advected magnetic field. Plasma interferometry is used to diagnose the line-integrated electron density. The oblique shocks, which are represented by abrupt discontinuities in electron density, exhibit hollow density profiles. A detached bow shock forms ahead of the probe and exhibits a fully 3D structure, with a larger opening angle in the end-on plane than in the side-on plane. The shock Mach angle is used to determine the upstream Mach number ($3 < M_1 < 8$) of the flow. Experimental results are compared with full 3D simulations performed using the resistive MHD code GORGON. Synthetic optical Thompson scattering spectra are generated, which form the basis of future experiments.

The laboratory experiments presented here provide insight into the fundamental physics of radiatively cooled oblique shocks and 3D bow shocks in magnetized collisional plasmas, relevant to internal shocks in astrophysical flows, and external shocks around obstacles such as planetary bodies and spacecraft. The results provide a benchmark for theoretical models and numerical codes of astrophysical plasma shocks. Furthermore, even though inductive probes are widely used in HED experiments, their perturbative nature leads to questions about how reliably they can reconstruct the magnetic field in plasma flows. These experiments additionally aim to resolve this question by careful comparison between numerical simulations and experimental data.

1.3 Outline of Thesis

The rest of the thesis is organized as follows:

In Chapter 2, we introduce preliminary equations and present the fundamental theory of shocks in a magnetohydrodynamic fluid.

In Chapter 3, we provide a review of pulsed-power devices and Z-pinch wire arrays. The experimental results presented in this thesis are supported by, and interpreted using resistive MHD simulations in GORGON. The use of GORGON for simulation of shock experiments is discussed in §3.3. The diagnostics employed and proposed here include inductive probes, plasma interferometry, and optical Thompson scattering. These are summarized in §3.4.

Chapter 4 presents the experimental results and analysis of bow shocks generated due to the collision of magnetized upstream plasma flows with inductive probes. We report experimental results of electron density measured using plasma interferometry, and magnetic field measured using inductive probes. Experimental results are compared with full 3D resistive MHD simulations of bow shocks in exploding wire arrays.

Chapter 5 presents the experimental results and analysis of oblique shocks generated due to the collision of plasma flows from adjacent wire cores of the exploding Z-pinch array. Experimental results are compared with 2D resistive MHD simulations of oblique shocks in exploding wire arrays.

Finally, we summarize our primary findings and present conclusions in Chapter 6.

Chapter 2

Magnetohydrodynamic Shocks

2.1 Preliminary Equations

The governing equations in a collision-dominated plasma with sufficiently large temporal and spatial scales are the magnetohydrodynamic (MHD) equations. The MHD model provides a single-fluid description of the macroscopic behavior of a plasma. We can write the resistive MHD equations as:

$$\begin{aligned}
\frac{\partial \rho}{\partial t} &= -\nabla \cdot (\rho \mathbf{v}) \\
\rho \left(\frac{\partial}{\partial t} + \mathbf{v} \cdot \nabla \right) \mathbf{v} &= -\nabla p + \mathbf{j} \times \mathbf{B} = -\nabla p + \frac{1}{\mu_0} (\nabla \times \mathbf{B}) \times \mathbf{B} \\
\left(\frac{\partial}{\partial t} + \mathbf{v} \cdot \nabla \right) p &= -\gamma p \nabla \cdot \mathbf{v} + (\gamma - 1) \frac{\eta}{\mu_0^2} (\nabla \times \mathbf{B})^2 \\
\frac{\partial \mathbf{B}}{\partial t} &= \nabla \times (\mathbf{v} \times \mathbf{B}) + \frac{\eta}{\mu_0} \nabla^2 \mathbf{B} \\
\nabla \cdot \mathbf{B} &= 0
\end{aligned} \tag{2.1}$$

Here, ρ is the density, $\mathbf{v}$ is the velocity, p is the pressure, $\mathbf{j}$ is the current density, $\mathbf{B}$ is the magnetic field, η is the resistivity, and γ is the adiabatic index of the fluid, defined as the ratio of specific heat at constant pressure to that at constant volume, i.e. $\gamma = c_p / c_v$. In a typical plasma, the ion mass far exceeds the electron mass $m_i / m_e << 1$, so the momentum is carried primarily by the electrons. We assume that $m_e \to 0$, so the density described in Equation(s) 2.1 refers to the density of the ions. The velocity $\mathbf{v}$ describes the mass-averaged velocity, which in this case becomes identical to the ion velocity in the limit $m_i / m_e << 1$.

The first equation in Equation 2.1 is a statement of mass conservation. It equates the time rate of change of mass in a given system to the mass flux entering the boundaries of the system. It is true for all plasmas which do not have additional source/sink terms. The second equation is a statement of conservation of momentum. It says that the total time rate of change of momentum in an MHD fluid is due to the pressure gradient force ∇p and the Lorentz force $\mathbf{j} \times \mathbf{B}$. The third equation is a statement of conservation of energy. The internal energy of an MHD fluid may change due to compression $-\gamma p \nabla \cdot \mathbf{v}$, or due to resistive heating $\eta \mathbf{j}^2$. Finally, the last two equations describe the evolution of the magnetic field. The fourth equation is called the induction equation, and is derived from combining Maxwell's equations with Ohm's law. It shows that the magnetic field can be advected by the plasma due to the $\nabla \times (\mathbf{v} \times \mathbf{B})$ term, and can also diffuse resistively due to the $(\eta/\mu_0)\nabla^2 \mathbf{B}$ term. The final equation $\nabla \cdot \mathbf{B}$ says that there can be no sources or sinks of magnetic field.

We can define a dimensionless quantity called the magnetic Reynolds' number $Re_m = UL/(\eta/\mu_0)$ by taking the ratio of the convective and diffusive terms in the induction equation. Here, U and L represent the characteristic velocity and length scale of the fluid. The magnetic Reynolds' number describes the relative importance of convection to resistive diffusion. When the magnetic Reynolds' number is large, i.e. $Re_m \gg 1$, resistive diffusion is negligible and the magnetic field is primarily advected by the flow. The magnetic field is then said to be 'frozen into' the flow. This effect is mathematically identical to the Helmholtz vorticity freezing theorem for inviscid flows.

The resitive MHD equations are derived from the single-fluid equations under a strict set of assumptions, which are, in turn, derived from moments of the Boltzmann equation. In general, the resistive MHD equations are valid when (1) the plasma is collisionally dominated, i.e. $(m_i/m_e)^{1/2}\lambda_{ii}/a << 1$, and (2) the ion gyro-radius r_{Li} is small compared to the length scale of the plasma $r_{Li}/a << 1$ (Freidberg [2014]). Here, λ_{ii} is the ion-ion mean free path and a is the characteristic length scale of the plasma. Furthermore, when $(m_e/m_i)^{1/2}(r_{Li}/a)^2(a/\lambda_{ii}) << 1$, we can assume that the resistivity is small $\eta \to 0$ (Freidberg [2014]). This limit is known as the ideal MHD limit, and it allows us to drop the resistive terms in the energy and magnetic field equations. However, even when the resistivity is small, its contribution may not be negligible. This is because the resistive contribution in Equation(s) 2.1 is a combination of resistivity and gradients of the magnetic field. Therefore, in plasmas with large gradients of the magnetic field, such as within a shock layer, the resistive contribution can become significant even when the resistivity is small. In collisional shocks, resistive dissipation facilitates the transition between upstream and downstream states.

2.2 Linear MHD Waves

We can derive the dispersion relations for linear MHD waves from the linearized ideal MHD equations. Consider an infinite homogeneous medium defined by equilibrium quantities — $\mathbf{v_0}$, $\mathbf{j_0} = 0$, p_0, ρ_0 and $\mathbf{B_0} = B_0\hat{\mathbf{e}}_\mathbf{z}$, and subject to linear perturbations of the form $\tilde{Q}(\mathbf{r}, t) = Q_1 e^{-i\omega t} e^{i\mathbf{k}\cdot\mathbf{r}}$, such that $\partial_t \to -i\omega$ and $\nabla \to i\mathbf{k}$. Here, $\tilde{Q}$ represents a small perturbation $\tilde{Q}/Q_0 << 1$ to the background quantity Q_0. We assume, for simplicity, a coordinate frame where $\hat{\mathbf{e}}_\mathbf{z}$ is parallel to the background magnetic field, and the wavevector $\mathbf{k} = k_\parallel \hat{\mathbf{e}}_\mathbf{z} + k_\perp \hat{\mathbf{e}}_\mathbf{y}$ lies in the z-y plane. Linearizing the MHD equations, and keeping only the first-order terms, we get (Freidberg [2014]):

$$\begin{aligned} \omega\rho_1 &= \rho_0\,(\mathbf{k}\cdot\mathbf{v}_1) \\ \rho_0\omega\mathbf{v_1} &= i\mathbf{j_1}\times\mathbf{B_0} + \mathbf{k}p_1 \\ \omega p_1 &= \gamma p_0\,(\mathbf{k}\cdot\mathbf{v}_1) \\ \omega\mathbf{B}_1 &= -\mathbf{k}\times(\mathbf{v}_1\times\mathbf{B}_0) \\ \omega\mu_0\mathbf{j}_1 &= -i\mathbf{k}\times[\mathbf{k}\times(\mathbf{v}_1\times\mathbf{B}_0)] \\ \mathbf{k}\cdot\mathbf{B_1} &= 0 \end{aligned} \tag{2.2}$$

These equations can be combined and expressed as an eigenvalue problem:

$$\begin{bmatrix} \omega^2 - k_\parallel^2 V_A^2 & 0 & 0 \\ 0 & \omega^2 - (k_\parallel^2 C_S^2 + k^2 V_A^2) & -k_\parallel k_\perp C_S^2 \\ 0 & -k_\parallel k_\perp C_S^2 & \omega^2 - k_\parallel^2 C_S^2 \end{bmatrix} \begin{bmatrix} v_x \\ v_y \\ v_z \end{bmatrix}_1 = 0 \tag{2.3}$$

Here, $V_A = B_0^2/\sqrt{\mu_0\rho_0}$ is the Alfvén speed, and $C_S = \sqrt{\gamma p_0/\rho_0}$ is the sound speed. Setting the determinant to 0 gives us the dispersion relations for the shear Alfvén, the slow magnetosonic wave, and the fast magnetosonic wave:

$$\begin{aligned} &\omega^2 = k_\parallel^2 V_A^2 \qquad \text{(Shear Alfvén Wave)} \\ &\omega^2 = \frac{1}{2}k^2\left(V_A^2 + C_s^2\right)\left[1 \pm \left(1-\alpha^2\right)^{1/2}\right] \qquad \text{(Magnetosonic Wave)} \\ \text{Where}\quad &\alpha^2 = 4\cos^2\theta\,\frac{C_S^2 V_A^2}{\left(C_S^2 + V_A^2\right)^2} \end{aligned} \tag{2.4}$$

Here, θ is the angle between the direction of propagation of the wave and the background magnetic field.

The phase speed ω/k of the shear Alfvén wave is:

$$(\omega/k)_A^2 = V_A^2 \cos^2\theta \tag{2.5}$$

The shear Alfvén wave is a transverse wave that propagates along magnetic field lines at the Alfvén speed, and results in field line bending, but no magnetic compression. It represents a competition between inertial effects and magnetic tension.

Similarly, for the magnetosonic wave, the phase velocity is:

$$(\omega/k)_{f,s}^2 = \frac{V_A^2 + C_S^2}{2}\left(1 \pm \sqrt{1 - 4\cos^2\theta \frac{V_A^2 C_S^2}{(C_S^2 + V_A^2)^2}}\right) \tag{2.6}$$

The slow and fast magnetosonic waves are compressional waves which represent a competition between inertial effects, and plasma and magnetic field compression. Their speed of propagation depends on the angle between the magnetic field and the direction of propagation.

We can visualize the anisotropy of MHD waves via a Friedrichs I diagram, as shown in Figure 2-1. The Friedrichs I diagram represents the phase velocity of the principal MHD modes in velocity space as a function of the direction of propagation. The fast wave phase velocity varies from a maximum of $V_{MS} = \sqrt{C_S^2 + V_A^2}$ perpendicular to the magnetic field, to a minimum velocity, equal to the higher of the sound and Alfvén speeds, along the magnetic field. The slow wave does not propagate perpendicular to the magnetic field, and has a maximum velocity, equal to the lower of the sound and Alfvén speeds, along the magnetic field. The shear Alfvén wave propagates at the Alfvén speed along the magnetic field, and does not propagate perpendicular to the field.

The sound speed C_S and the Alfvén speed V_A can be related using the plasma β, which represents the ratio of thermal to magnetic pressure in a plasma:

$$\frac{C_S^2}{V_A^2} = \frac{\gamma p/\rho}{B^2/(\rho\mu_0)} = \frac{\gamma}{2}\beta \tag{2.7}$$

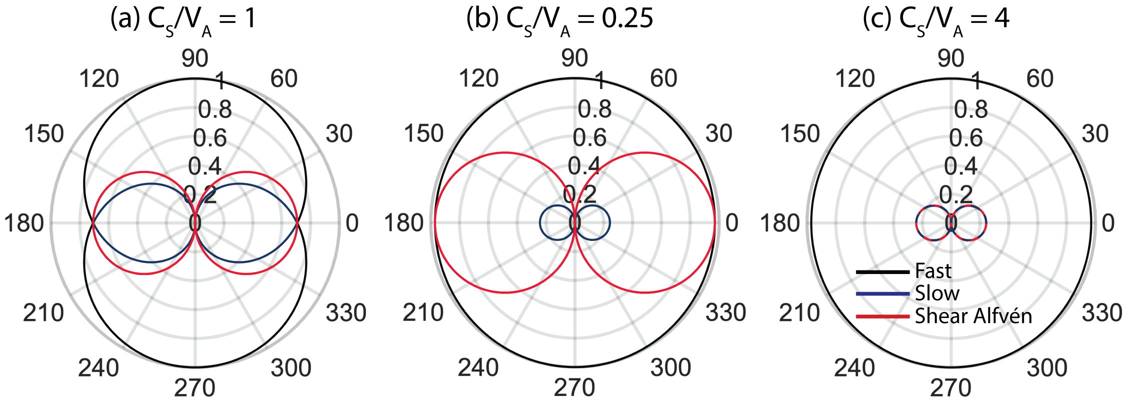

Figure 2-1: Friedrichs I diagrams representing the normalized phase velocity of fast (black line), slow (blue line), and Shear Alfvén (red line) waves as a function of the angle of propagation relative to the magnetic field. Note that the phase velocity is normalized using the magnetosonic wave speed V_{MS}. (a) Friedrichs I diagram for $C_S/V_A = 1$. The fast wave phase velocity varies from a maximum of V_{MS} perpendicular to the magnetic field, to a minimum velocity, equal to the higher of the sound and Alfvén speeds, along the magnetic field. The slow wave does not propagate perpendicular to the magnetic field, and has a maximum velocity, equal to the lower of the sound and Alfvén speeds, along the magnetic field. The shear Alfvén wave propagates at the Alfvén speed along the magnetic field, and does not propagate perpendicular to the field. (b) Friedrichs I diagram for $C_S/V_A = 0.25$. The fast wave speed is approximately isotropic and approaches the Alfvén speed. (c) (b) Friedrichs I diagram for $C_S/V_A = 4$. The fast wave speed is approximately isotropic and approaches the sound speed.

For small $\beta << 1$, the sound speed is much smaller than the Alfvén speed, and the fast magnetosonic wave becomes the compressional Alfvén wave, which propagates isotropically at the Alfvén speed. This is illustrated in Figure 2-1b. For large $\beta >> 1$, the sound speed is much larger than the Alfvén speed, and the fast magnetosonic wave becomes the ion sound wave i.e. $V_f \approx C_S$. This situation is illustrated in Figure 2-1c.

2.3 MHD Shock Jump Conditions

Within the shock, the evolution of thermodynamic properties, magnetic field, and the flow velocity constitute a non-linear problem, and must be solved accounting for collisional dissipative effects which convert the upstream state to the downstream state. Since ideal MHD does not account for dissipation, these equations cannot be used to describe plasma evolution within the shock. However, asymptotically upstream and downstream of the shock, ideal MHD accurately describes the equilibrium fluid states, and we can use the conservation of mass, momentum, and energy to relate the upstream and downstream states.

To derive the jump conditions, we first express the ideal MHD equations in conservative form (Goedbloed et al. [2010]):

$$\begin{aligned}
\partial_t \int_V \rho \, dV &= -\int_S \rho \mathbf{v} \cdot \mathbf{dA} \\
\partial_t \int_V \rho \mathbf{v} \, dV &= -\int_S \left(\rho \mathbf{v}\mathbf{v} + (p + \frac{B^2}{2\mu_0})\mathbf{I} - \frac{\mathbf{B}\mathbf{B}}{\mu_0} \right) \cdot \mathbf{dA} \\
\partial_t \int_V \left(\rho \frac{v^2}{2} + \frac{p}{\gamma - 1} + \frac{B^2}{2\mu_0} \right) dV &= -\int_S \left(\rho \frac{v^2}{2} + \frac{\gamma p}{\gamma - 1} \right) \mathbf{v} \cdot \mathbf{dA} - \int_S \frac{\mathbf{E} \times \mathbf{B}}{\mu_0} \cdot \mathbf{dA} \\
\partial_t \int_V \mathbf{B} \, dV &= \int_S \hat{\mathbf{n}} \times (\mathbf{v} \times \mathbf{B}) \, dA \\
\int_S \mathbf{B} \cdot \mathbf{dA} &= 0
\end{aligned} \tag{2.8}$$

We transition to a frame moving with the shock front $\mathbf{u} = \mathbf{v} - u_s \hat{\mathbf{n}}$. Here, $\mathbf{v}$ is the fluid velocity in the laboratory frame, u_s is the shock velocity, and $\hat{\mathbf{n}}$ is the unit vector normal to the shock front. Carrying out the integral over across a control volume surrounding the shock, and setting the shock thickness $\delta \to 0$, we get (Boyd and Sanderson [2003]):

$$[\![\rho u_n]\!] = 0 \tag{2.9}$$

$$[\![\rho \mathbf{u}(u_n) + \left(p + B^2/2\mu_0\right) \hat{\mathbf{n}} - (B_n)\mathbf{B}/\mu_0]\!] = 0 \tag{2.10}$$

$$\left[\!\!\left[\left(\frac{\rho u^2}{2} + \frac{\gamma p}{\gamma - 1} + \frac{B^2}{\mu_0} \right) u_n - \frac{(\mathbf{B} \cdot \mathbf{u}) B_n}{\mu_0} \right]\!\!\right] = 0 \tag{2.11}$$

$$[\![\hat{\mathbf{n}} \times (\mathbf{u} \times \mathbf{B})]\!] = 0 \tag{2.12}$$

$$[\![B_n]\!] = 0 \tag{2.13}$$

Furthermore, entropy must increase across the shock. So, entropically permitted shocks satisfy (Goedbloed et al. [2010]):

$$\left[\!\!\left[\frac{p}{\rho^\gamma} \right]\!\!\right] \leq 0 \tag{2.14}$$

Here, the double square brackets represent $[\![\phi]\!] = \phi_1 - \phi_2$, where ϕ_1 is the upstream state and ϕ_2 is the downstream state. Equations 2.9 - 2.14 relate the upstream and downstream equilibrium states once all dissipative effects are accounted for. They are called the Rankene-Hughniot relations.

2.4 Hydrodynamic Shocks

We can obtain the hydrodynamic jump conditions by taking the limit $\mathbf{B} \to 0$. The jump conditions Equations 2.9 - 2.13 then become:

$$\begin{aligned}
[\![\rho u_n]\!] &= 0 \\
[\![\rho u_n^2 + p]\!] &= 0 \\
[\![\rho \mathbf{u_t}(u_n)]\!] &= 0 \\
\left[\!\!\left[\left(\frac{\rho u^2}{2} + \frac{\gamma p}{\gamma - 1}\right) u_n\right]\!\!\right] &= 0
\end{aligned} \tag{2.15}$$

Since the mass flux across the boundaries of the shock is constant $\rho_1 u_{1,n} = \rho_2 u_{2,n}$, the tangential velocity is also continuous across the shock front, i.e. $\rho_1 u_{n,1} [\![\mathbf{u_t}]\!] = 0 \Rightarrow [\![\mathbf{u_t}]\!] = 0$. Therefore, in a hydrodynamic shock, the tangential velocity remains unaltered while the normal velocity, pressure, and density are discontinuous.

2.4.1 Normal Shock

Consider a shock where the upstream flow $\mathbf{u_1} = u_1 \hat{\mathbf{n}}$ is normal to the shock front. Since the tangential velocity remains continuous across the shock $[\![\mathbf{u_t}]\!] = 0$, the tangential component of the downstream velocity is also zero $\mathbf{u_{t,2}} = 0$. We can combine the mass, momentum, and energy jump conditions to express the downstream Mach number $M_2 = u_{n,2}/C_{s,2} = \rho_2 u_{n,2}/(\gamma p_2)$ in terms of the upstream Mach number $M_1 = \rho_1 u_{n,1}/(\gamma p_1)$ (Kundu et al. [2012]):

$$M_2^2 = \frac{(\gamma - 1)M_1^2 + 2}{2\gamma M_1^2 + 1 - \gamma} \tag{2.16}$$

The entropy jump condition Equation 2.14 implies that for permitted jumps, $M_1 \geq 1$, i.e. the upstream flow is supersonic. Given the upstream parameters, we can also determine the downstream parameters as a function of the upstream Mach number M_1 (Kundu et al. [2012]):

$$\frac{\rho_2}{\rho_1} = \frac{u_{1,n}}{u_{2,n}} = \frac{(\gamma+1)M_1^2}{(\gamma-1)M_1^2+2} \tag{2.17}$$

$$\frac{p_2}{p_1} = 1 + \frac{2\gamma}{(\gamma+1)}(M_1^2-1) \tag{2.18}$$

In the strong shock limit $M_1 >> 1$, the compression ratio approaches $\rho_2/\rho_1 \rightarrow (\gamma+1)/(\gamma-1)$. For the ideal gas value of $\gamma = 5/3$, the maximum compression ratio is 4.

2.4.2 Oblique Shock

Consider a shock where the shock front forms at some angle σ to the upstream velocity, as shown in Figure 2-2. Relative to the shock, the incoming flow has a component parallel and a component orthogonal to the shock front, i.e. $\mathbf{u_1} = u_{1,n}\hat{\mathbf{n}} + \mathbf{u_{1,t}}$. From Equations 2.15, we see again that the tangential component of velocity remains continuous, while the normal component is discontinuous, such that the downstream flow will now form at an angle to the upstream flow. The effect is that the flow vector is rotated by an angle ϕ across the shock front. The angle $\sigma = \tan^{-1}(u_{n,1}/u_{t,1})$ at which the shock forms relative to the shock front is called the shock angle, while the angle ϕ by which the flow vector is rotated is called the deflection angle.

Since the jump conditions 2.15 remain unchanged, we can determine the upstream and downstream states across the oblique shock simply by expressing the normal Mach number in terms of the total Mach number and the shock angle, i.e. $M_{1,n} = u_1 \sin\sigma / C_{s,1} = M_1 \sin\sigma$. Replacing $M_1 \rightarrow M_1 \sin\sigma$ into the normal shock relations, we get:

$$\frac{p_2}{p_1} = 1 + \frac{2\gamma}{\gamma+1}\left(M_1^2\sin^2\sigma - 1\right) \tag{2.19}$$

$$\frac{\rho_2}{\rho_1} = \frac{(\gamma+1)M_1^2\sin^2\sigma}{(\gamma-1)M_1^2\sin^2\sigma+2} \tag{2.20}$$

$$M_2^2\sin^2(\sigma-\phi) = \frac{(\gamma-1)M_1^2\sin^2\sigma+2}{2\gamma M_1^2\sin^2\sigma+1-\gamma} \tag{2.21}$$

The deflection angle ϕ can also be expressed as a function of the upstream Mach num-

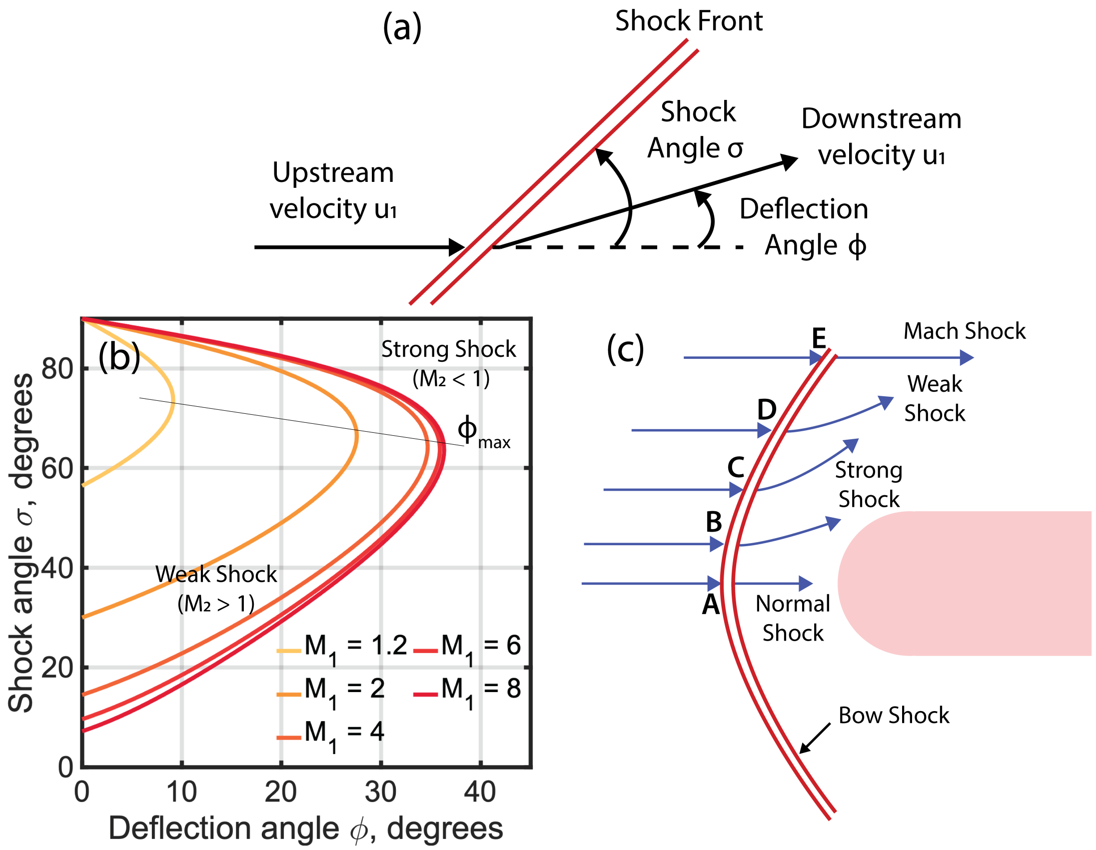

Figure 2-2: (a) Hydrodynamic oblique shock geometry. The upstream velocity vector is defected by an angle ϕ across the shock front. The shock front forms at an angle σ to the upstream velocity vector. (b) Shock angle as a function of defection angle for different upstream Mach number M_1. The shock angle can vary between $\pi/2$ (normal shock) and the Mach angle (Mach shock). For a given defection angle, there are two possible solutions - weak shock and strong shock - for the shock angle. (c) Detached bow shock ahead of a blunt obstacle. The bow shock represents an oblique shock with varying shock and deflection angles. The shock is strongest at the nose, where the shock angle is 90^o; this constitutes a normal shock. Far away from the obstacle, the shock becomes an infinitesimally weak Mach shock.

ber M_1 and the shock angle σ (Kundu et al. [2012]):

$$\tan\phi = 2\cot\sigma \frac{M_1^2 \sin^2\sigma - 1}{M_1^2(\gamma + \cos 2\sigma) + 2} \tag{2.22}$$

Note that for entropically permitted shocks, the upstream normal Mach number $M_1 \sin\sigma$ should still exceed unity.

From the solution of 2.22, as shown in Figure 2-2b, we can summarize key aspects of oblique shocks:

- Setting $\phi = 0$, in Equation 2.22, we get two possible solutions for which there is no deflection — $\sigma = \sin^{-1}(1/M_1) \equiv \mu$ and $\sigma = \pi/2$. The first case corresponds to the Mach wave, which represents an oblique shock of infinitesimal strength. Substituting $\sigma \rightarrow \mu \equiv \sin^{-1}(1/M_1)$, it can be shown that $\rho_2/\rho_1 \rightarrow 1$, i.e. (no compression). The second case ($\sigma = \pi/2$) represents normal shocks, for which the velocity is perpendicular to the shock front. This case represents the maximum possible compression ratio.

- For constant M_1, and $\mu \leq \sigma \leq \pi/2$, a straight oblique shock solution only exists for $\phi \leq \phi_{\max}$. The maximum deflection angle $\phi_{\max}$ increases with M_1.

- For $\phi < \phi_{\max}$ and constant M_1, there are two possible solutions for σ. If the solution lies above the $\phi = \phi_{\max}$ line, the shock is said to be strong, otherwise it is said to be weak. For a strong shock, the downstream flow is always subsonic, while for a weak shock, the downstream flow is usually supersonic, except for in a narrow range where ϕ is close to $\phi_{\max}$. In reality, most oblique shocks are weak shocks, such that the post-shock flow remains supersonic (Anderson [2001]).

- For a weak shock, increasing the deflection angle ϕ increases the shock angle σ, while for a strong shock, increasing the deflection angle ϕ decreases the shock angle σ.

- When the deflection angle is increased beyond the maximum deflection angle $\phi > \phi_{\max}$, a straight oblique shock solution is not possible. In this case, we get a detached curved shock front at some distance from the nose of the obstacle. Therefore, an attached oblique shock becomes a detached bow shock for large deflection angles $\phi > \phi_{\max}$. For a blunt obstacle, we always get a detached bow shock instead of an attached oblique shock (Anderson [2001]).

2.4.3 Bow Shocks

Bow shocks are detached shocks characterized by curved shock fronts. They appear when a supersonic flow collides with a blunt object, or with a sharp object for which the deflection angle is greater than the maximum permissible deflection angle. Figure 2-2c illustrates a detached bow shock ahead of a blunt obstacle. The distance from the nose of the obstacle at which the detached bow shock forms is called the shock stand-off distance.

The bow shock represents an oblique shock with varying shock and deflection angles. At the nose of the obstacle (Point A), the shock angle $\sigma = \pi/2$, i.e. the shock front is perpendicular to the upstream velocity. This constitutes a normal shock with deflection angle $\phi = 0$, and the normal shock relations 2.16 - 2.18 apply. Moving away from the nose, the shock angle σ decreases, and the deflection angle ϕ increases (Point B). This constitutes a strong oblique shock. In this regime, the post-shock plasma is subsonic. At some point C, the deflection angle ϕ increases to its maximum permissible value ϕ_{max} for the given upstream Mach number M_1. Beyond this point, both the shock angle σ and the deflection angle ϕ decrease; this constitutes a weak oblique shock (Point D). In this regime, the post-shock plasma is supersonic. Finally, far away from the obstacle (Point E), the shock angle reaches the Mach angle $\sigma \to \mu = \sin^{-1}(1/M_1)$. Here, the deflection angle is zero, i.e. $\phi(\sigma = \mu) = 0$.

The stand-off distance and the shape of the shock front depend on the upstream Mach number M_1, as well as the shape and size of the obstacle. Analytical solutions are typically inadequate, and the shock structure must be calculated numerically (Van Dyke [1958]; Anderson [2001]). In general, increasing the upstream Mach number M_1 will decrease the stand-off distance (Van Dyke [1958]; Anderson [2001]).

2.5 MHD Shocks

Equations 2.9 - 2.13 describe the equilibrium states upstream and downstream of a fully MHD shock. Unlike in a hydrodynamic shock, the tangential velocity $\mathbf{u_t}$ can now be discontinuous, and depends on the jump in the tangential magnetic field $\mathbf{B_t}$:

$$\rho u_n [\![\mathbf{u_t}]\!] = B_n [\![\mathbf{B_t}]\!] \tag{2.23}$$

Therefore, the angle $\vartheta = \tan^{-1}(B_t/|B_n|)$ between the shock normal and the magnetic field can modify shock properties. Figure 2-3 shows the different types of permissible MHD shocks. We first examine the simple parallel ($\vartheta = 0$) and perpendicular ($\vartheta = \pi/2$) shock limits.

2.5.1 Parallel Shocks

When $\vartheta_{1,2} = 0$, the upstream and downstream magnetic field only have components normal to the shock i.e. $\mathbf{B_{t,1,2}} = \mathbf{0}$, $B_n \neq 0$. This situation in depicted in Figure 2-3a. The jump conditions 2.9 - 2.13 reduce to the hydrodynamic jump conditions 2.15. Therefore, parallel shocks are hydrodynamic in nature and the magnetic field does not participate

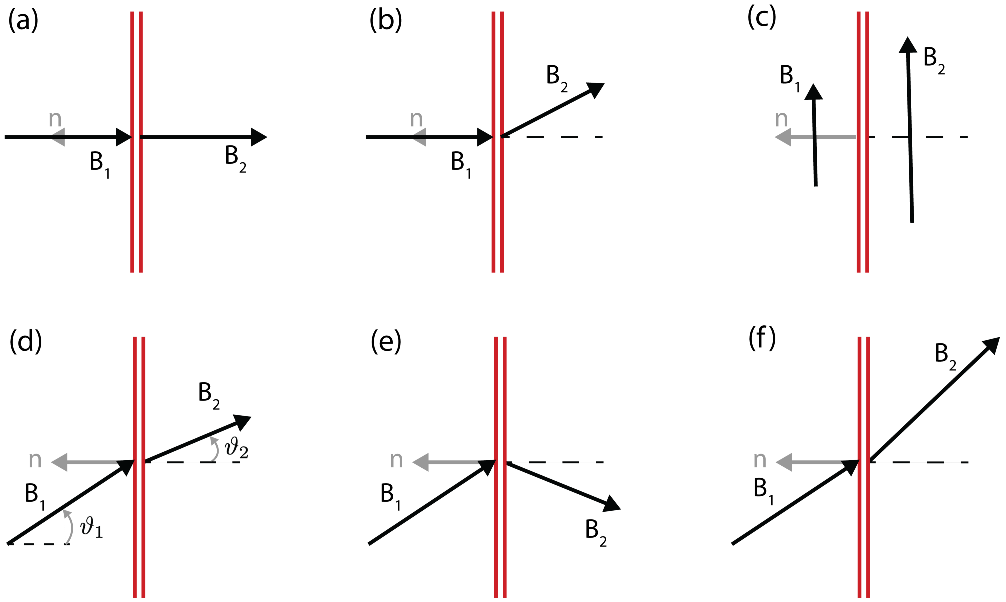

Figure 2-3: Types of MHD shocks (a) Parallel shock. The upstream magnetic field is parallel to the shock normal. The magnetic field remains continuous, and the shock is hydrodynamic. (b) Switch on shock. There is no tangential upstream magnetic field, but the downstream magnetic field has a non-zero tangential component. (c) Perpendicular shock. The upstream magnetic field is perpendicular to the shock normal. The downstream magnetic field is compressed. Perpendicular shocks represent super-fast to sub-fast transitions. (d) Slow shock. Slow shocks represent super-slow to sub-slow transitions in which the post-shock magnetic field is deflected towards the shock normal. (e) Intermediate shock. These represent super-Alfvénic to sub-Alfvénic or sub-slow transitions. The magnetic field changes direction across the shock. (f) Fast shock. These represent super-fast to sub-fast transitions. The magnetic field is compressed and deflected away from the shock normal.

in the shock dynamics.

In some cases, when $\vartheta_1 = 0$ but $\vartheta_2 \neq 0$, i.e. there is a non-zero downstream tangential magnetic field $\mathbf{B_{t,2}} \neq \mathbf{0}$. This is depicted in Figure 2-3b, and the shock is called a switch-on shock. A switch-on shock is an fast/intermediate MHD shock for which the downstream Alfvén Mach number is 1. (Goedbloed et al. [2010]).

2.5.2 Perpendicular Shocks

Consider a flow $\mathbf{u_1} = u_1\,\hat{\mathbf{n}} = u_1\,\hat{\mathbf{e}}_\mathbf{x}$ with a magnetic field $\mathbf{B_1} = B_1\,\hat{\mathbf{e}}_\mathbf{y}$, such that the upstream magnetic field is perpendicular to the shock normal $B_n = 0$, $\vartheta = \pi/2$. This is illustrated in 2-3c. The downstream velocity is also parallel to the shock normal, since $[\![\mathbf{u_t}]\!] = 0$ when

$B_n = 0$. The jump conditions 2.9 - 2.13 become (Boyd and Sanderson [2003]):

$$\begin{aligned}
\rho_1 u_1^2 + p_1 + \frac{B_1^2}{2\mu_0} &= \rho_2 u_2^2 + p_2 + \frac{B_2^2}{2\mu_0} \\
u_1^2 + \frac{\gamma p_1}{\rho_1(\gamma-1)} + \frac{B_1^2}{\rho_1\mu_0} &= u_2^2 + \frac{\gamma p_2}{\rho_2(\gamma-1)} + \frac{B_2^2}{\rho_2\mu_0} \\
\frac{B_2}{B_1} = \frac{\rho_2}{\rho_1} &= \frac{u_1}{u_2}
\end{aligned} \tag{2.24}$$

Introducing $\beta_1 = 2\mu_0 p_1/B_1^2$ and the sound Mach number $M_1 = \rho u_1^2/(\gamma p_1)$, we combine the jump conditions to get:

$$\begin{aligned}
(r-1)\left\{2(2-\gamma)r^2 + \left[2\gamma(\beta+1) + \beta\gamma(\gamma-1)M_1^2\right] r - \beta\gamma(\gamma+1)M_1^2\right\} = 0 \\
\text{Or} \qquad (r-1)\left[ar^2 + b(M_1^2,\beta_1)r + c(M_1^2,\beta_1)\right] = 0
\end{aligned} \tag{2.25}$$

Where $r \equiv \rho_2/\rho_1$ is the density compression ratio and $R \equiv p_2/p_1$ is the pressure ratio. Note that in a perpendicular shock, both the density and the magnetic field are compressed by the same ratio.

The solutions of Equation 2.25 are $r = 1$ (no compression), and $r = (1/2a)\left(-b \pm \sqrt{b^2-4ac}\right)$. Entropically permitted shocks are compressive ($r \geq 1$), so the entropically permitted shock satisfies:

$$\begin{aligned}
\sqrt{b^2-4ac} &> 2a+b \\
\beta\gamma(\gamma+1)M_1^2 &> 2(2-\gamma) + 2\gamma(\beta+1) + \beta\gamma(\gamma-1)M_1^2 \\
M_1^2 > 1 + \frac{2}{\gamma\beta_1} &\Rightarrow u_1^2 > C_S^2 + V_A^2 \equiv V_f^2
\end{aligned} \tag{2.26}$$

Therefore, entropically permitted perpendicular shocks represent super-fast ($M_f > 1$) to sub-fast transitions ($M_f < 1$).

We can determine the downstream sound Mach number M_2 and plasma beta β_2 from:

$$\begin{aligned}
M_2^2 &= M_1^2 \frac{1}{rR} \\
\beta_2 &= \beta_1 \frac{R}{r^2}
\end{aligned} \tag{2.27}$$

Where R is the pressure ratio:

$$R \equiv \frac{p_2}{p_1} = 1 + \frac{1-r^2}{\beta_1} + \frac{\gamma M_1^2(r-1)}{r} \tag{2.28}$$

We plot the solution of the Equation 2.25 as a function of the upstream fast Mach number $M_{f,1}$ in Figure 2-4a. The solution lies in the entropically permissible region only for super-fast $M_{f,1} \geq 1$ to sub-fast transitions $M_{f,1} \leq 1$. The compression ratio increases with increasing upstream fast Mach number. In the strong shock limit, the compression ratio approches $r \rightarrow 4$ for $\gamma = 5/3$. The solution is a weak function of the upstream β_1.

2.5.3 Oblique MHD Shocks

We express the jump conditions 2.9 - 2.14 in non-dimensional (Goedbloed et al. [2010]):

$$[\![\bar{\mathbf{u}}_\mathbf{t}]\!] = [\![\bar{\mathbf{B}}_\mathbf{t}]\!] \tag{2.29}$$

$$[\![\left(M^2-1\right)\bar{\mathbf{B}}_\mathrm{t}]\!] = 0 \tag{2.30}$$

$$[\![M^2 + \bar{p} + \frac{1}{2}\bar{B}_\mathrm{t}^2]\!] = 0 \tag{2.31}$$

$$[\![\frac{\gamma}{\gamma-1}\bar{p}M^2 + \frac{1}{2}\left(1+\bar{B}_\mathrm{t}^2\right)M^4]\!] = 0 \tag{2.32}$$

$$[\![\bar{p}M^{2\gamma}]\!] \leq 0 \tag{2.33}$$

Where $\bar{u}_n \equiv \mu_0\rho|u_n|/B_n^2 u_n = -M^2$, $\bar{\mathbf{u}}_\mathbf{t} \equiv \mu_0\rho|u_n|/B_n^2\mathbf{u}_\mathbf{t}$, $\bar{B}_n \equiv B_n/|B_n| = -1$, $\bar{B}_t = B_t/|B_n| \equiv \tan\vartheta$, and $\bar{p} \equiv \mu_0 p/B_n^2 = \beta/2$. Note that $M^2 \equiv \mu_0\rho u_n^2/B_n^2$ is the square of the normal Alfvén Mach number and is only defined for $B_n \neq 0$.

Combining the jump conditions, we can determine the downstream normal Alfvén Mach number M_2 as a function of M_1, ϑ_1 and β_1. This is called the distilled MHD energy jump condition:

$$\begin{aligned}&\frac{1}{2}\left(M_2^2-1\right)^2\left\{(\gamma+1)M_2^2-(\gamma-1)M_1^2-\gamma\beta_1\right\}\\&+\frac{1}{2}\tan^2\vartheta_1\left\{(\gamma-1)\left(M_2^2-1\right)\left(M_1^2-M_2^2\right)-M_2^2\left(M_1^2+M_2^2-2\right)\right\}=0\end{aligned} \tag{2.34}$$

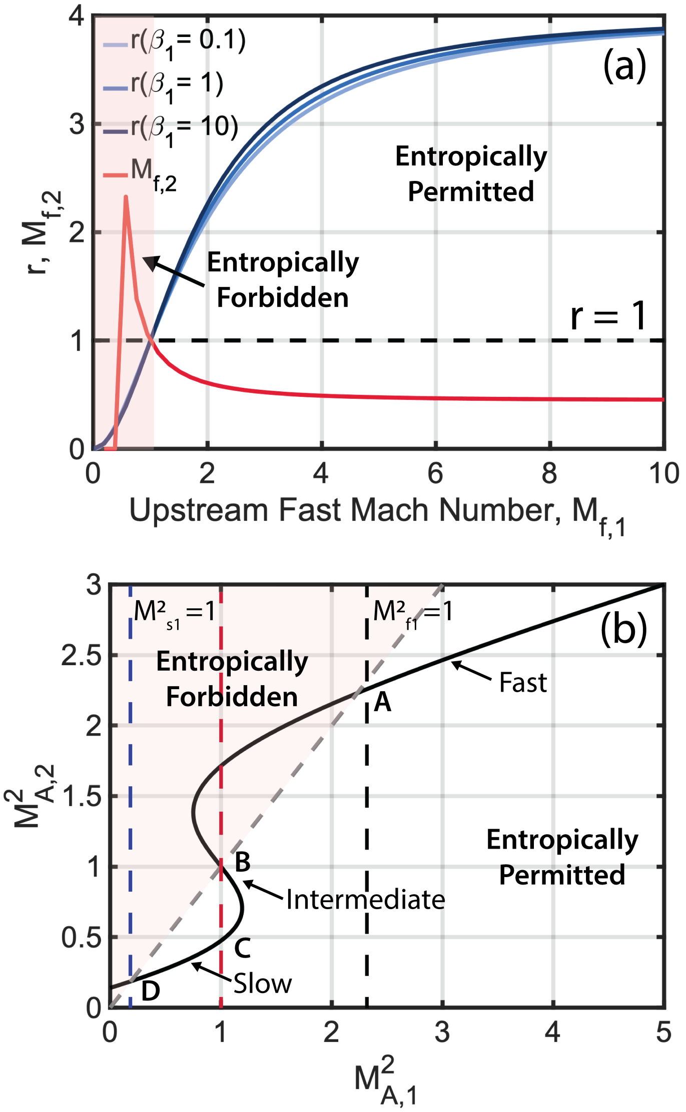

Figure 2-4: (a) Perpendicular shock solution for the compression ratio r and downstream fast Mach number $M_{f,2}$ as a function of the upstream fast Mach number. Entropically permitted shocks are compressive ($r \geq 1$) shocks, which represent super-fast to sub-fast transitions. The compression ratio represents the ratio of the post-shock density and magnetic field to the upstream density and magnetic field. In the strong shock limit ($M_{f,1} \to \infty$), the compression ratio approaches 4 for $\gamma = 5/3$. The solution is a weak function of the plasma β. (b) Solution of the distilled MHD energy jump condition for $\beta = 0.5$ and $\vartheta_1 = \pi/4$. The $M_{A,1} = M_{A,2}$ line separates entropically permitted solution from the entropically forbidden solutions (red). There are three types of permissible MHD shocks. For Mach numbers larger than point A, we get fast shocks, where the upstream velocity is super-fast and the downstream velocity is sub-fast. Between B and C, we get intermediate shocks, where the upstream velocity is super-Alfvénic and the downstream velocity is sub-Aflvéic or sub-slow. Between C and D, we get slow shocks, where the upstream velocity is super-slow and the downstream velocity is sub-slow.

The downstream parameters can be determined from:

$$\frac{u_{\mathrm{n}2}}{u_{\mathrm{n}1}} = \frac{\rho_1}{\rho_2} = \frac{M_2^2}{M_1^2} \tag{2.35}$$

$$\bar{\mathbf{B}}_{\mathbf{t},\mathbf{2}} = \frac{M_1^2 - 1}{M_2^2 - 1}\bar{\mathbf{B}}_{\mathbf{t},\mathbf{1}} \Rightarrow \vartheta_2 = \tan^{-1}\left(\frac{M_1^2 - 1}{M_2^2 - 1}\tan\vartheta_1\right) \tag{2.36}$$

$$\bar{p}_2 = \frac{\beta_2}{2} = \frac{\beta_1}{2} + (M_1^2 - M_2^2)\left[1 - \left(\frac{\bar{B}_{t,1}^2}{2}\right)\frac{M_1^2 + M_2^2 - 2}{(M_2^2 - 1)^2}\right] \tag{2.37}$$

Finally, from the entropy jump condition, it can be shown that entropically permitted jumps satisfy $M_2^2/M_1^2 \leq 1$.

Figure 2-4b shows the solution to Equation 2.34. The $M_{A,1}^2 = M_{A,2}^2$ line separates entropically permitted solutions from the entropically forbidden solutions. The three types of permissible MHD shocks are:

- **Slow shocks** $(1 \geq M_1^2 \geq M_2^2)$. These are super-slow to sub-slow transitions. In Figure 2-4, slow shocks are represented by the part of the solution that lies between points C and D, where the upstream velocity is super-slow. From Equation 2.36, $|\bar{\mathbf{B}}_{\mathbf{t},\mathbf{2}}| \leq |\bar{\mathbf{B}}_{\mathbf{t},\mathbf{1}}|$, so the magnetic field vector is deflected towards the shock normal. This shock is illustrated in Figure 2-3d.

- **Intermediate shocks** $(M_1^2 \geq 1 \geq M_2^2)$. These are super-Alfvénic to sub-Alfvénic or sub-slow transitions. In Figure 2-4, intermediate shocks are represented by the part of the solution that lies between points B and C, where the upstream velocity is super-Alfvénic, and the solution is multi-valued. $\bar{B}_{t,2}/\bar{B}_{t,2} < 0$, so the post-shock and the pre-shock magnetic fields have opposite directions. This is depicted in Figure 2-3e.

- **Fast shocks** $(M_1^2 \geq M_2^2 \geq 1)$. These are super-fast to sub-fast transitions. In Figure 2-4, fast shocks are represented by the part of the solution that lies to the right of point A, where the upstream velocity is super-fast. From Equation 2.36, $|\bar{\mathbf{B}}_{\mathbf{t},\mathbf{2}}| \geq |\bar{\mathbf{B}}_{\mathbf{t},\mathbf{1}}|$, so the magnetic field vector is deflected away from the shock normal. This shock is depicted in Figure 2-3f.

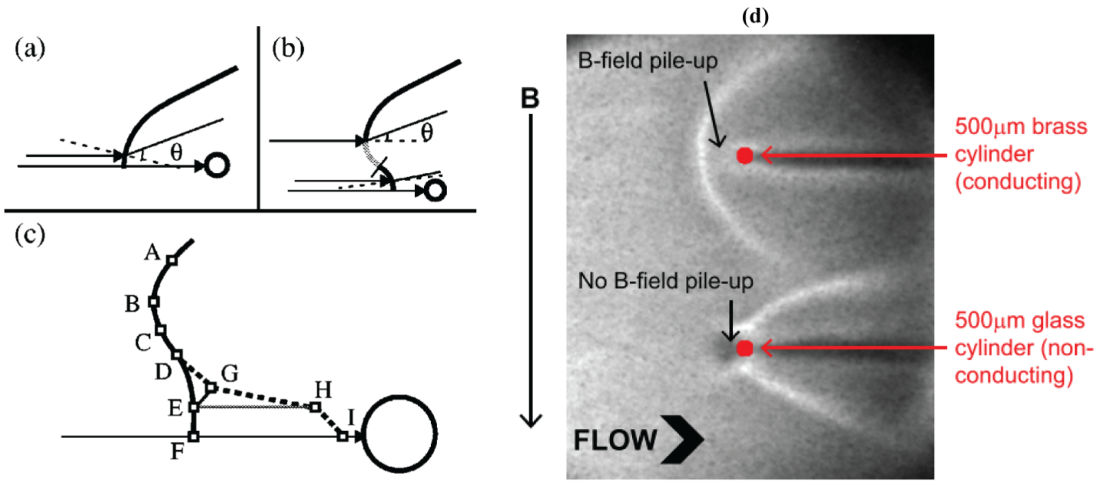

Figure 2-5: (a) Fast bow shock ahead of a cylindrical obstacle (De Sterck et al. [1998]). The upstream magnetic field is aligned with the flow and points from the left to the right. The shock front is concave to the cylinder everywhere ahead of the obstacle. (b) Shock front with a dimpled shape. At the nose, the shock is a switch-on shock, which is followed by an intermediate shock. The upper part of the shock represents a fast shock. (c) Bow shock with 2 interacting shock fronts. The leading shock front exhibits fast, intermediate and hydrodynamic parts, while the secondary shock front exhibits intermediate shock transitions. Reprinted from De Sterck et al. [1998] - "Complex magnetohydrodynamic bow shock topology in field-aligned low- flow around a perfectly conducting cylinder. Physics of Plasmas, 5(11), 4015–4027," with permission of AIP Publishing. (d) Optical self-emission images of bow shocks ahead of a conducting cylindrical obstacle (top), and a non-conducting cylindrical obstacle (bottom) (Burdiak et al. [2017]). Flux pile-up ahead of the conducting obstacle creates a bow shock with a larger opening angle and stand-off distance compared to the non-conducting case. Reprinted from Burdiak et al. [2017] - "The structure of bow shocks formed by the interaction of pulsed-power driven magnetised plasma flows with conducting obstacles. Physics of Plasmas, 24(7)," with permission of AIP Publishing

2.5.4 MHD Bow Shocks

In an MHD bow shock, the shock morphology depends not only on the upstream Mach number, but also on the plasma β and the angle ϑ between the shock front and the magnetic field. Simulations of bow shocks in the switch-on regime show complex shock structures with multiple interacting fronts, where a leading shock front is followed by a secondary shock front (De Sterck et al. [1998];De Sterck and Poedts [2000]). The leading shock front is a super-fast to sub-fast transition; it then splits into two shock fronts — one super-fast to sub-fast transition while the other is an intermediate super-fast to sub-Alfvénic transition, which then evolves into a slow shock. Similarly, 2D simulations, around perfectly conducting cylinders with field-aligned flow in the switch-on regime, exhibit complex shock structures with 2 interacting shock fronts (De Sterck et al. [1998]). The leading shock front exhibits fast, intermediate, and hydrodynamic parts, while the secondary shock front exhibits intermediate shock transitions, as illustrated in Figure 2-5a.

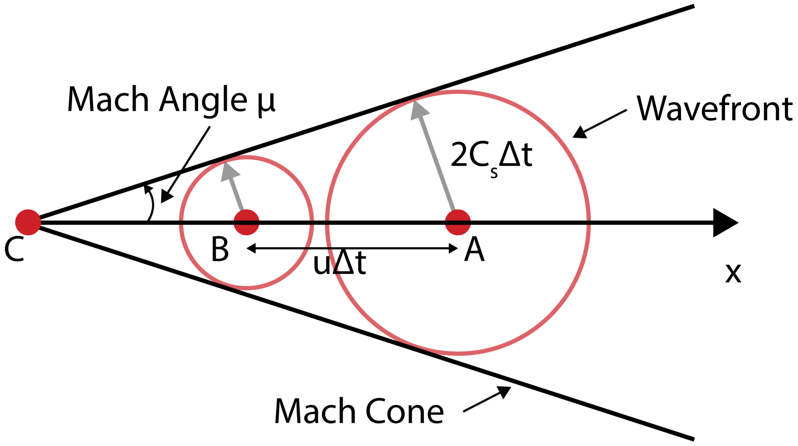

Figure 2-6: Mach cone in a hydrodynamic fluid. The disturbance, initially at position A, moves with a supersonic velocity u form the left to the right. The disturbance emits spherical sound waves which travel outwards at the sound speed C_S. At some time $t = 2\Delta t$, the disturbance is at position C and has traveled a distance $2u\Delta t$ from its initial position. The tangential surface which connects the spherical wavefronts forms the surface of the Mach cone.

Furthermore, in magnetized shocks, the accumulation of magnetic flux at the obstacle and field line bending can further modify the bow shock structure, such that the bow shock shape is determined by a competition between the magnetic tension of the bent field lines and the incoming ram pressure. In such shocks, where flux accumulation modifies shock morphology and two-fluid effects facilitate the shock transition, have been experimentally observed in magnetized bow shocks formed from super-fast flows around conducting cylindrical obstacles (Suttle et al. [2019]; Burdiak et al. [2017]).

2.6 Mach Wave

Consider a point source traveling with some velocity u in the negative x-direction in a stationary hydrodynamic fluid, as shown in Figure 2-6 (or equivalently, a stationary obstacle in a fluid moving in the positive x-direction with velocity u). The source emits spherical sound waves which propagate radially outwards isotropically at the local sound speed C_S. If $u = 0$, the wavefronts form concentric spherical surfaces which radiate outwards in time. If the source is non-stationary and travels with a velocity $u < C_S$, the center of each successive wavefront will be shifted to the left by a distance $u\Delta t$; however, trailing wavefronts cannot catch up with the leading wavefront, and information

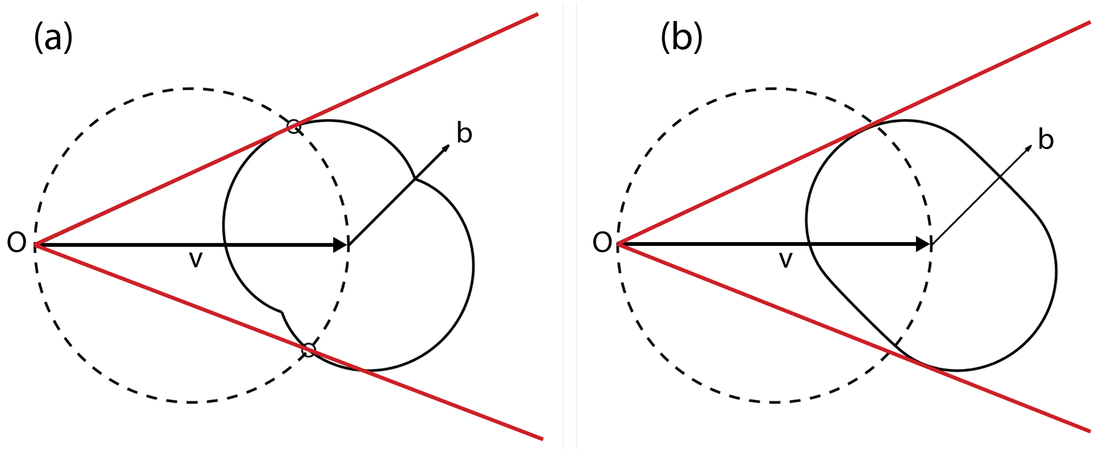

Figure 2-7: (a) Determination of the Fast Mach angle using Friedrichs I diagram. The velocity circle (dashed line) is centered at $(0, v/2)$. The magnetic field vector makes an angle of $\pi/4$ with the velocity vector. The fast magnetosonic phase-speed (solid black line) has a minimum value along the magnetic field and a maximum value perpendicular to the field. The Mach lines (sold grey lines) are determined by connecting the origin to the points of intersection of the velocity circle and the Friedrichs I diagram. Here, the sound Mach number and the Alfvén Mach number are equal to 3.3. (b) Determination of the Fast Mach angle using Friedrichs II diagram.

propagates both upstream and downstream of the disturbance.

If $u > C_S$, trailing wavefronts now catch up with and overtake the leading wavefront, such that information cannot travel downstream before the disturbance arrives. In Figure 2-6, the disturbance, initially at point A, travels to point C after some time $t = 2\Delta t$. Points A and C are separated by a distance $2u\Delta t$, and the original wavefront generated at $t = 0$ has now traveled a distance $2C_s\Delta t$. The tangential surface which connects the spherical wavefronts forms the surface of the Mach cone, and represents a discontinuity between upstream and downstream states. The half-angle of the Mach cone is called the Mach angle μ. We can determine the Mach angle μ from the ratio of the radial extent of each wavefront to the distance traveled by the point source, and show that it is related to the Mach number (Kundu et al. [2012]):

$$\mu = \sin^{-1}\left(\frac{C_S\Delta t}{u\Delta t}\right) = \sin^{-1}(1/M_S) \tag{2.38}$$

The Mach wave represents an oblique shock of infinitesimal strength. The shock angle σ here is equal to the Mach angle μ, for which the deflection of the velocity vector is zero. For an MHD shock, we can have three possible Mach cones associated with each of the three linear MHD waves. Of these, the fast Mach cone is typically the most relevant, since the fast velocity represents the maximum velocity with which a linear MHD perturbation can propagate in a plasma. However, unlike a sound wave whose phase speed is independent of direction, the slow, fast, and Alfvén phase speeds are anisotropic and depend on the angle θ_{bk} between the wave vector **k** and the magnetic field **B**. The fast wave phase speed varies from a maximum of $M_{ms} = \sqrt{v_A^2 + C_S^2}$ perpendicular to the magnetic field ($\theta_{bk} = \pi/2$) to a minimum of $\max(v_A, C_S)$ parallel to the magnetic field ($\theta_{bk} = 0$). Therefore, the Mach angle can also vary between $1/M_{ms} \leq \sin\mu \leq 1/M_{A,s}$ depending on the value of θ_{bk}. In the limiting case $\beta << 1$, $C_S^2 << v_A^2$, so the fast magnetosonic speed becomes $V_{ms}(\beta << 1) \approx V_A$. Similarly, when $\beta >> 1$, $C_S^2 >> v_A^2$, so the fast magnetosonic wave becomes a sound wave $V_{ms} \approx C_S$. In both limiting cases, the fast wave phase speed can be approximated to be isotropic.

For other cases, we can determine the Mach angle from the phase speed representation in velocity space (Friedrichs I diagram) (Spreiter and Stahara [1985]; Spreiter and Alksne [1969]; Petrinec and Russell [1997]). This method is illustrated in Figure 2-7a. We assume a coordinate system where the upstream velocity **V** is along the x-axis. In the plane that contains **B** and **V**, we draw a sphere of diameter V centered at $(V/2, 0)$. Next, we draw the phase velocity curve of the fast wave phase speed for the given direction of the magnetic field **B**. We can now determine the point(s) of intersection of the velocity sphere with the phase diagram, and connect the origin to the points of intersection to get the Mach lines which delineate the surface of the Mach cone. This method, however, is only applicable for certain symmetric cases, and does not account for the difference in direction between the central wave vector and the velocity vector of a propagating point disturbance (Verigin et al. [2003]). For the symmetric cases $\theta_{bk} = 0$ and $\theta_{bk} = \pi/2$, the analytical solutions for the Mach angle are (Spreiter and Stahara [1985]):

$$
\begin{aligned}
\sin\mu &= \frac{\sqrt{M_S^2 + M_A^2 - 1}}{M_A M_S} \qquad (\theta_{bv} = 0) \\
\sin\mu &= \sqrt{\frac{M_S^2 + M_A^2 + 1 + \sqrt{\left(M_S^2 + M_A^2 + 1\right)^2 - 4M_S^2 M_A^2}}{2M_S^2 M_A^2}} \qquad (\theta_{bv} = \pi/2)
\end{aligned}
\tag{2.39}
$$

The velocity of propagation of a point disturbance is the group velocity. We can determine the group velocity from the envelope of all plane waves at unit time emitted from the origin at $t = 0$. We can also use a group velocity representation to determine the Mach angle (Friedrichs II diagram) (Spreiter and Alksne [1969]). This method is illustrated in Figure 2-7b. We draw the group velocity diagram centered at $(0, V)$, and determine the tangent to the curve that crosses through the origin. This is equivalent to the velocity-space representation of the MHD version of the Mach cone depicted in the hydrodynamic case.

Verigin et al. [2003] describe a third method of determining the Mach angle directly from the MHD Rankene-Hughniot relations. We assume that far from the obstacle, the shock surface assumes a simple conic shape given by $x + a(\varphi)\rho = 0$. Here, φ is the azimuthal angle, ρ is the radial length and x is the axial length of the cylindrical coordinate system whose axis is aligned with the shock axis. The Mach angle can then be determined from the gradient of the curve at a given φ at $x \to \infty$, i.e. $\tan\mu(\phi) = -\partial_x \rho = 1/a(\phi)$. By setting the density ratio to unity $r \to 1$ in the Rankene-Hughniot conditions, the 3D asymptotic shape of the MHD shock can be determined from the solution of a non-linear ordinary differential equation (Verigin et al. [2003]):

$$\left[(a' \sin\varphi - a\cos\varphi)\sin\theta_{bv} + \cos\theta_{bv}\right]^2 = M_A^2 + M_S^2 - \frac{M_A^2 M_S^2}{1 + a^2 + a'^2} \tag{2.40}$$

Here, θ_{bv} is the angle between the upstream magnetic field and velocity vectors, and $a' = da/d\varphi$.

2.7 Adiabatic index of a plasma

It is clear from the analysis above that the adiabatic index of the plasma γ plays an important role in shock physics. The adiabatic index γ, which is defined as the ratio of specific heats, is closely related to the polytropic index ζ, which relates the pressure to the density in a polytropic process (Moran et al. [2010]):

$$\frac{p}{\rho^\zeta} = \text{const.} \tag{2.41}$$

By combining the first law of Thermodynamics $dq = d\epsilon + pd(1/\rho)$, and ideal gas law $p = nk_B T$, we can show that for a polytropic ideal gas, the polytropic index ζ is a function of the specific heats:

$$\zeta = \frac{c_P - c}{c_V - c} \tag{2.42}$$

Here, $c_p = dh/dT$ represents the change in specific enthalpy h per unit temperature, $c_V = (d\epsilon/dT)_V$ represents the change in specific internal energy ϵ per unit change in temperature at constant volume, and c represents the heat transferred per unit mass per unit temperature, i.e. $c = dq/dT$. For an isentropic process, no heat is transferred, so $c = 0$. The polytropic index reduces to the ratio of specific heats, which is defined as

$\gamma = c_p/c_v$.

We can also show that for an isentropic process, the internal energy and the pressure can be related as:

$$\rho\epsilon = \frac{p}{\gamma - 1} \tag{2.43}$$

We can use Equation 2.43 to define an effective adiabatic index:

$$\gamma = 1 + \frac{p}{\rho\epsilon} \tag{2.44}$$

The pressure and internal energy density in an ideal plasma with $T_e = T_i$ are:

$$\begin{aligned} p &= (Z+1) n_i k_B T \\ \rho\epsilon &= \frac{3(Z+1) n_i k_B T}{2} \end{aligned} \tag{2.45}$$

These equations represent the standard statistical thermodynamics result for an ideal gas. We can derive them by calculating the Helmholtz free energy F and canonical partition function $\mathcal{Z}_N$ of a dilute gas with N indistinguishable non-interacting particles, which are defined as (Chen [2005]):

$$\begin{aligned} F &= -k_B T \ln \mathcal{Z}_N \\ \mathcal{Z}_N &= \sum_j^N \sum_i^\infty \exp\left[-\frac{E_{i,j}}{k_B T}\right] \\ p &= -\left(\frac{\partial F}{\partial V}\right)_{T,N} \\ \int \rho\epsilon dV &= \sum E_i \frac{\exp(-E_i/k_B T)}{\mathcal{Z}_N} \end{aligned} \tag{2.46}$$

Here, E_i, j represents the i-th energy level of particle j, typically represented using the particle-in-box quantum mechanical solution, and we are summing over N particles to find the total canonical partition coefficient of the N-particle ensemble. The pressure is defined as the volume derivative of the Helmholtz free energy at constant temperature and constant N, and the total internal energy is the summation of the expected energy level of all particles.

The first equation in 2.45 is the familiar ideal gas relation, and the second equation is the statement that the total internal energy is equal to the summation of the kinetic energy of all particles in the gas. Alternatively, we could have also derived the ideal gas internal energy relationship by integrating the kinetic energy of each particle over a Maxwellian distribution function. From Equation(s) 2.45 and 2.44, we can conclude that $\gamma = 5/3$ for an ideal gas.

Most plasmas can be treated as ideal gases with a $\gamma = 5/3$. However, for HED plasmas, the contribution of Coulomb interactions (potential energy of the electrons in the electric field of the ions), ionization energy, and excitation energy may become significant (Drake [2013]). Consequently, the total internal energy of the ionized plasma is larger than that of the ideal gas, and from Equation 2.44, we can expect the effective adiabatic index to be smaller than the ideal value of 5/3. In particular, for an ionized high-Z plasma, the pressure and internal energy density can be estimated using (Drake [2013]):

$$\begin{aligned} p &= 1.6 \times 10^{-12} n_i T_e \left(1 + 0.63\sqrt{T_e} - 2.76 \times 10^{-8} n_i^t\right) \\ \rho\epsilon &= 1.6 \times 10^{-12} n_i \Big[1.43\sqrt{T}_e + 4.2 T_e \\ &\quad + T_e^{3/2}\left(1.3 - 0.315 \ln\left(\frac{n_i}{10^{23} T_e}\right)\right)\Big] \end{aligned} \tag{2.47}$$

Where all quantities are in CGS units, and temperature is in eV. For our plasmas of interest with $n_i \sim 10^{18}$ cm^{-3} and $T_e \sim 10$ eV, the value of the adiabatic index is $\gamma \approx 1.13$.

Similarly, strong radiative losses from a plasma can also modify the balance of pressure and internal energy. In radiation-dominated plasmas, the value of the adiabatic index is $\gamma = 4/3$ (Drake [2013]).

2.8 Summary of MHD Shocks

The theoretical discussion presented in this chapter will form the basis of our analysis in subsequent chapters. The MHD equations describe the macroscopic behavior of a collisionally-dominated ($\sqrt{m_i/m_e}\lambda_{ii}/a << 1$) plasma with small ion Larmor radius ($r_{Li}/a << 1$). We can use the conservation of mass, momentum, and energy to relate the upstream and downstream states of a shock; these jump conditions are called the Rankene-Hughniot jump conditions. Taking the hydrodynamic limit $\mathbf{B} \to 0$, we can determine the relationships between upstream and downstream states for normal and oblique hydrodynamic shocks. A detached bow shock always forms ahead of a blunt obstacle in a supersonic flow, and represents an oblique shock with varying deflection and shock angles. At the nose of the obstacle, the shock is strongest and constitutes a normal shock. Far away from the obstacle, the shock is infinitesimally weak and constitutes a Mach shock. In the ideal MHD limit, we can derive three types of MHD shocks — fast shocks, which are super-fast to sub-fast transitions, slow shocks which are super-slow to sub-slow transitions, and intermediate shocks which are super-Alfvénic to sub-Alfvénic or sub-slow shocks. MHD shock solutions not only depend on the upstream Mach number, but also the plasma β and the orientation of the magnetic field.

Chapter 3

Pulsed Power and Z-pinch Wire Arrays

3.1 Pulsed Power Generators

Pulsed-power machines are HEDP facilities used to apply a fast-rising high-amplitude current pulse to an inductive load. Pulsed-power machines achieve this by discharging large capacitors and compressing the generated current pulse over a short period of time. The largest existing pulsed-power machine is the Z HEDP facility at Sandia National Labs. It is a high-impedance system capable of generating a peak current of 20MA with a rise time of 300 ns (Sinars et al. [2020]). Other examples of pulsed-power generators include MAGPIE (~ 1MA, 240ns; Imperial College London) (Mitchell et al. [1996]), COBRA (~1MA, 100ns; Cornell University) (Smith et al. [1995]), MAIZE (~1MA, 100ns; University of Michigan) (McBride et al. [2018]), and ZEBRA (~1MA, 100ns; University of Nevada Reno) (Bauer et al. [1999]).

There are two commonly used pulsed-power technologies — Marx Generator / Pulse Forming Lines, and Linear Transformer Drivers (LTDs). Compared to the former, LTDs are modular and self-contained devices capable of achieving low inductance and high capacitance (McBride et al. [2018]). An example of a LTD-based pulsed-power system is the MAIZE generator at the University of Michigan. Another LTD-based pulsed-power machine called PUFFIN is under development at MIT (Hare et al. [2020]). An exhaustive review of LTDs can be found in McBride et al. [2018].

Marx generators and Pulse Forming Lines (PFLs) are used in the majority of existing pulsed-power machines, including the Z, MAGPIE and COBRA generators (Sinars et al. [2020]; Mitchell et al. [1996]; Smith et al. [1995]). The MAGPIE generator at Imperial College London, which was used to generate the plasma in the experiments presents here,

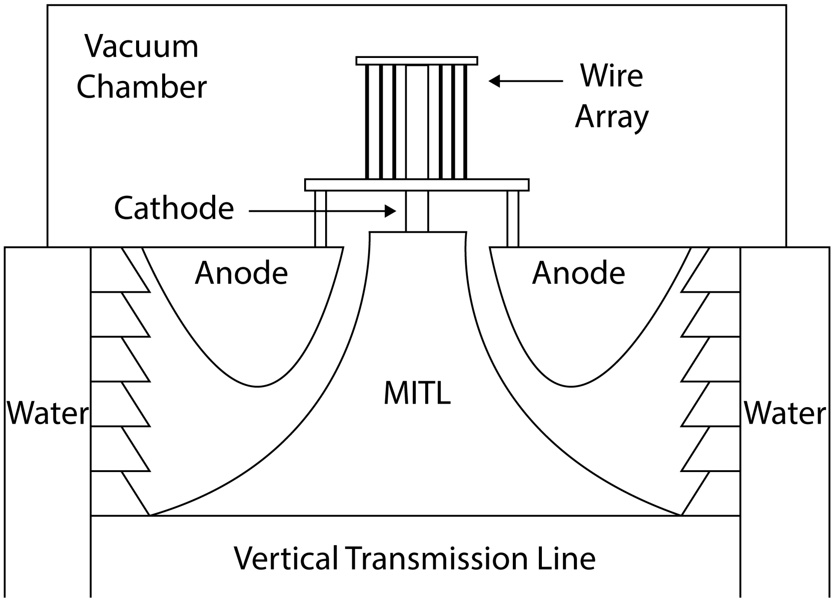

Figure 3-1: Schematic of a pulsed-power machine Magnetically Insulated Transmission Line (MITL) and load setup. The MITL is a coaxial line with a tapering cross-section which delivers the signal from the large-diameter OTL to the load, that sits in a vacuum chamber on top of the MITL.

comprises 4 Marx banks (with 24 1.3 μF capacitors) with 4 PFLs (Mitchell et al. [1996]). A Marx generator is a collection of capacitors and spark-gap switches. We charge the capacitors in parallel and discharge them in series, so that the output voltage is amplified by a factor equal to the number of capacitors.

Marx banks generate a low-amplitude slow-rising signal. PFLs, which consist of intermediate capacitances with successively smaller discharge times, are needed to compress this signal to create a fast-rising high-amplitude pulse. The signal then travels via the Output Transmission Line (OTL) (on MAGPIE, this is called the Vertical Transmission Line) to the Magnetically Insulated Transmission Line (MITL). The OTL is typically a large-diameter coaxial cable insulated with deionized water (Mitchell et al. [1996]; McBride et al. [2018]).

The MITL is a coaxial line with a tapering cross-section, as illustrated in Figure 3-1a. It delivers the signal from the large-diameter OTL to the load, which sits in a vacuum chamber on top of the MITL. The MITL is said to be magnetically insulated; this is be-

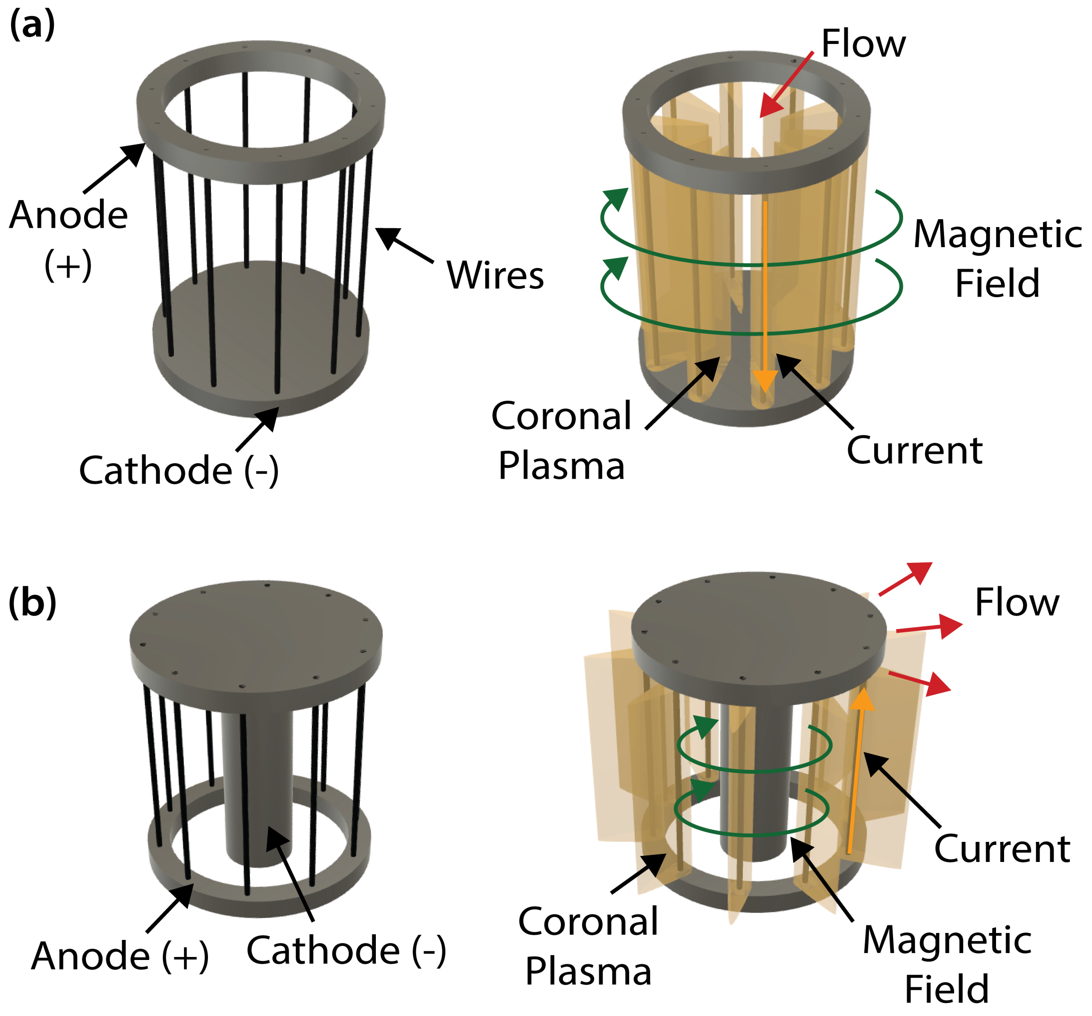

Figure 3-2: (a) 3D representation of of an imploding wire array. The global magnetic pressure acts on the outside edge of the wires and causes radially converging flows of plasma. (b) 3D representation of of an exploding wire array. The wires are arranged around a central conductor. The global magnetic pressure acts on the inside edge of the wires and causes radially diverging outflows of plasma.

cause the large current in the MITL generates strong azimuthal magnetic fields. Any charge carrier which leaves the MITL experiences a strong radial $\mathbf{v} \times \mathbf{B}$ force which returns it to the MITL (Mendel et al. [1983]). Magnetic insulation typically deteriorates later in time (typically after peak current). When the magnetic field becomes small enough, charge carriers can escape the MITL and breakdown occurs.

3.2 Wire Array Z-Pinches

A z-pinch refers to any cylindrical column of plasma, through which current propagates in the axial (or the 'z') direction. Wire array z-pinches refer to cylindrical, conical or planar arrays of wires, which have been historically used as loads in pulsed-power machines to generate intense bursts of x-ray and XUV radiation (Deeney et al. [1997]; Haines et al. [2005]; Giuliani and Commisso [2015]). It was later discovered that wire arrays could also be used as sources of highly collisional magnetized plasmas for laboratory astrophysics applications (Lebedev et al. [2019]; Lebedev et al. [2002]; Haines et al. [2002]). A commonly used configuration is a cylindrical array, which can be of two types — imploding arrays (Lebedev et al. [1999]; Lebedev et al. [2001]; Lebedev et al. [2005] Ampleford et al. [2010];), and exploding arrays (also called inverse z-pinch arrays) (Harvey-Thompson et al. [2009]; Hare et al. [2018]). An imploding wire array is a cylindrical cage of wires, as shown in Figure 3-2a. The magnetic pressure acts on the outside edge of the wires and pushes the plasma radially inwards towards the array center. Imploding wire arrays have been traditionally used to generate and study highly energetic XUV and X-ray radiation (Ryutov [2000]; Lebedev et al. [2005]; Giuliani and Commisso [2015]). In an exploding array, as illustrated in Figure 3-2b, the wires are arranged around a central conductor. The global magnetic pressure acts on the inside edge of the wires and causes radially diverging outflows of plasma.

We use exploding wire arrays in the experiments presented in this thesis. Exploding wire arrays offer several advantages over other geometric configurations that make them ideal for these experiments. Exploding wire arrays generate azimuthally symmetric flows; which means that we can expect the properties of the flow to vary predominately in the radial direction. Note that exploding wire arrays exhibit modulations in the axial and azimuthal directions, but these modulations are generally periodic (Chittenden and Jennings [2008]; Harvey-Thompson et al. [2009]; Swadling et al. [2013]). Moreover, the radially diverging nature of the flows means that the plasma can flow uninterrupted into the relatively large vacuum region, which allows for better diagnostic access to the plasma.

When a strong current pulse is applied to the wire array, the material in the wires heats Ohmically, and vaporizes and ionizes to form a ring of hot low-density coronal plasma around the relatively dense cold wire cores (Lebedev et al. [2001]). The initial explosion of the wires is not well understood and typically results in an inhomogeneous column of vapor and liquid states, which comprises the stationary wire cores. The total magnetic field in the array is the superposition of the local magnetic fields around each wire. In an exploding array, the magnetic field B_θ points in the azimuthal direction, and decays

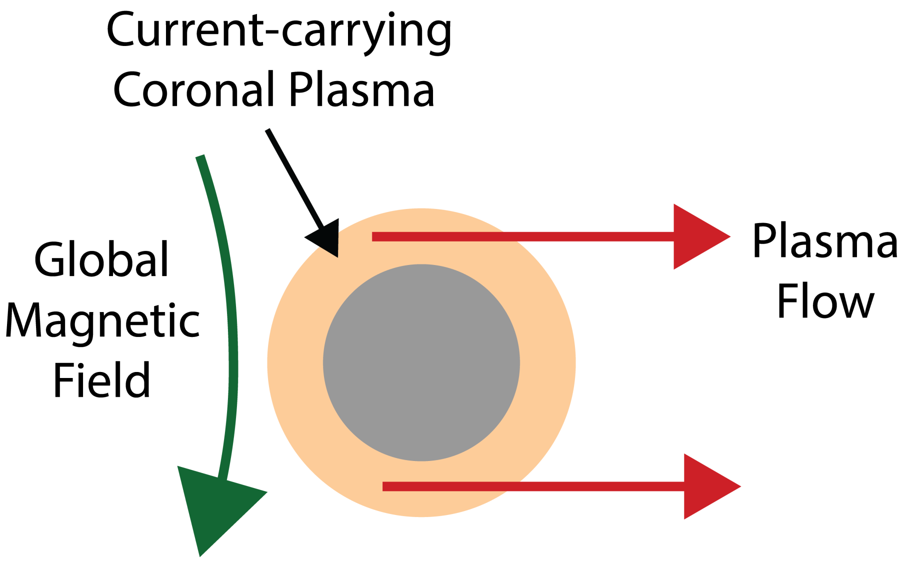

Figure 3-3: Current-carrying coronal plasma around the central wire core.

as $B_\theta \sim I/r$ inside the array(Harvey-Thompson et al. [2009]). Here, I is the current and r is the radial distance from the array center. The total current enclosed by an Amperian loop is zero outside the array for an exploding array, so that the azimuthal magnetic field $\oint \mathbf{B} \cdot \mathbf{ds} = 0$ goes to zero here. This is illustrated in Figure 3-4b. Because of the large magnetic pressure inside the array compared to the outside, the coronal plasma experiences a net outwards magnetic force.

Most of the current density is concentrated within a thin skin region at the surface of the wire cores (Lebedev et al. [2005]; Lebedev et al. [2001]). The current flows preferentially through the conducting coronal plasma in the skin region, and the wire cores, which experience little magnetic pressure, expand at the sound speed, while the coronal plasma accelerates radially outwards under the action of the global $\mathbf{j} \times \mathbf{B}$ force (Lebedev et al. [2001]). The plasma ablates into a force-free region initially devoid of a magnetic field. The ablating plasma advects some magnetic field and current with it, such that the magnetic field is redistributed into the initially force-free flow region (Burdiak et al. [2017]). The initial phase of the wire array is marked by the continuous ablation of plasma from the wire cores — this is called the ablation phase. Characteristic parameters for a pulsed-power driven Aluminum plasma on a ~ 1 MA facility during the ablation phase are shown in Table 3.1.

Table 3.1: Characteristic parameters for a pulsed-power driven Aluminum plasma on a ~ 1 MA facility during the ablation phase

Measurable Quantities	Electron density n_e (cm^{-3})	10^{18}
	Magnetic Field B (T)	10
	Velocity v (cm s^{-1})	10^7
	Ion temperature T_i (eV)	10
	Electron temperature T_e (eV)	10
	Effective Ionization, $n_e/n_i = Z$	3.5
Derived Quantities	Alfvén Speed V_A (cm s^{-1})	8 10^6
	Ion Sound Speed C_s(cm s^{-1})	2×10^6
	Fast Magnetosonic Speed V_f(cm s^{-1})	8×10^6
	Ion Larmor Radius r_{Li} (cm)	7×10^{-3}
	Electron Larmor Radius r_{Le} (cm)	1×10^{-4}
	Ion Inertial Length δ_i (cm)	6×10^{-2}
	Ion-Ion Mean Free Path λ_{ii} (cm)	1×10^{-5}
	Electron Plasma Frequency $\omega_{p,e}$ (rad s^{-1})	6×10^{13}
Non-dimensional Quantities	Sonic Mach Number $M_s = v/C_S$	7
	Alfvèn Mach Number $M_A = v/V_A$	2
	Fast Mach Number $M_A = v/V_f$	2
	Reynolds' Number $Re = va/\nu$	10^6
	Magnetic Reynolds' Number $Re_m = \mu_0 va/\eta$	10
	Plasma Beta β	0.1
	Adiabatic Index γ	1.13
	Ion Magnetization r_{Li}/a	10^{-2}
	Electron Magnetization r_{Le}/a	10^{-4}
	Collisionality $(m_i/m_e)^{1/2}(\lambda_{ii}/a)$	10^{-3}

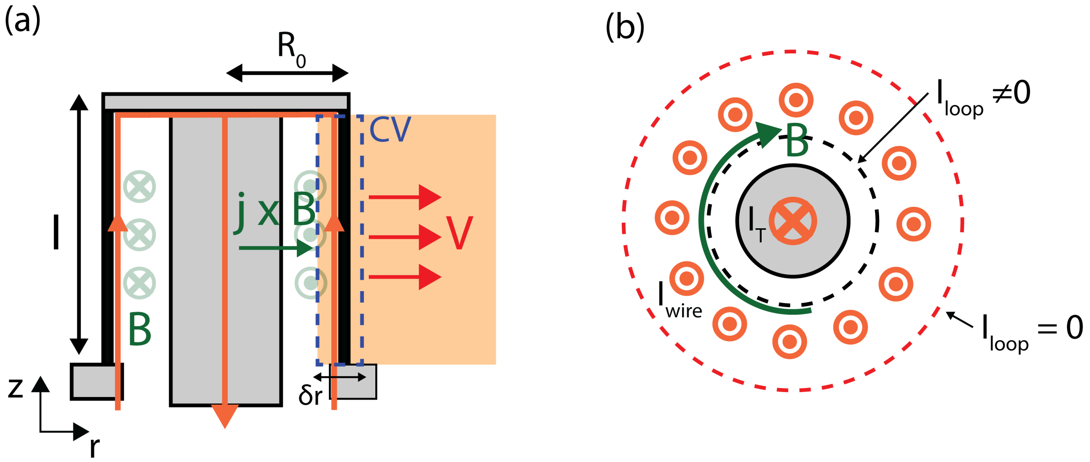

Figure 3-4: (a) Side-on (r-z plane) view of an exploding wire array. In the derivation of the rocket model, we assume that the wire cores remain stationary and the magnetic pressure accelerates the coronal plasma to a constant velocity V in a thin skin region of width δr. (b) Top (r-θ) view of an exploding wire array. At t= 0s, the total current enclosed within the Amperian loop outside the array is zero, while the current enclosed within the Amperian loop inside the array is non-zero. The net magnetic pressure thus pushes the plasma radially outwards.

Experiments and simulations of wire arrays have shown an axial non-uniformity in the ablation rate. The axial non-uniformity corresponds a $m = 0$-like instability, and exhibits a quasi-periodic structure with a time-independent wavelength comparable to the wire core size (Lebedev et al. [1999]; Harvey-Thompson et al. [2009]; Chittenden and Jennings [2008]). The wavelength of the modulation typically grows with the growth of the radius of the coronal plasma, and then becomes constant later in time, when the coronal plasma stops expanding. This point typically corresponds to the time at which the global magnetic field becomes large enough to switch the topology of the magnetic field around the wire core. The non-uniform ablation rate eventually leads to breaks in the wires, which signifies the end of the ablation phase, and the beginning of the explosion/implosion phase Lebedev et al. [2005]; Lebedev et al. [2001]. The current path through the wires is disrupted, and the current switches to the plasma, which experiences an abrupt and rapid acceleration (Lebedev et al. [2005]); Lebedev et al. [2001]). The trailing mass is left behind and does not participate in the explosion. In our experiments, we ‘over-mass’ the wires, such that the wires ablate continuously and do not experience the explosion phase.

3.2.1 Rocket Model of Mass Ablation

We can approximate the rate of mass ablation and radial density distribution from a wire array using the a simplified phenomenological model called the rocket model (Lebedev et al. [2005]). We use the following simplifying assumptions in the model:

(1) We neglect the discrete wires and model the wire array as a thin cylindrical plasma shell of radius R_0, height l, and thickness δr, with $R_0 \gg \delta r$.

(2) The wire cores remain stationary $dR_0/dt = 0$; all current density is concentrated in an infinitesimally thin skin layer at the surface. No current flows through ablated plasma, and the wire cores.

(3) The $\mathbf{j} \times \mathbf{B}$ force only acts on coronal plasma in the skin region.

(3) Plasma ablates outwards continuously from the surface of the shell with characteristic radial velocity V that is constant in time

The global magnetic field $\mathbf{B}$ in the exploding wire array is given by Ampere's law — the integral of the magnetic field along a closed contour $\mathbf{s}$ is proportional to the enclosed current I. For an Amperian loop inside the exploding array:

$$\begin{gathered}\oint \mathbf{B} \cdot \mathbf{ds} = \int_A \mu_0 \mathbf{j} \cdot \mathbf{dA} \\ \int_0^{2\pi} B_\theta r \, d\theta = \mu_0 I \Rightarrow B_\theta = \frac{\mu_0 I}{2\pi r}\end{gathered} \tag{3.1}$$

The magnetic field thus decays with radial distance from the array center. Outside the array, the total current in the Amperian loop is zero, so there is no magnetic field outside the wire array. Current flows in the coronal plasma on the inside of the wires, so the current density in the cylindrical shell is $I/4\pi R_0 \delta r$, and the $\mathbf{j} \times \mathbf{B}$ force density at the array radius $r = R_0$ is:

$$\mathbf{j} \times \mathbf{B} = \frac{\mu_0 I^2}{8\pi^2 R_0^2 \delta r} \hat{\mathbf{e}}_r \tag{3.2}$$

A mass balance on the control volume (CV) containing the coronal plasma (see Figure 3-4) shows us that the time rate of change of mass of the shell is equal to the area integral of the mass flux at the surface:

$$\dot{m} = -\rho_s A_s V \tag{3.3}$$

A momentum balance on the CV gives us:

$$\begin{aligned}\int \mathbf{j}\times\mathbf{B}\,dV &= \partial_t \int_V \rho\mathbf{v}dV + \int_A \rho\mathbf{v}\mathbf{v}\cdot\mathbf{dA} \\ \rho_s V^2 A_s &= \frac{\mu_0 I^2}{8\pi^2 R_0^2 \delta r} 2\pi R_0 \delta R l\end{aligned} \tag{3.4}$$

Substituting $\dot{m} = -\rho_s A_s V$, we can get an expression for the mass ablation rate from the wire array:

$$\dot{m} = -\frac{l\mu_0}{4\pi R_0 V} I^2(t) \tag{3.5}$$

The mass ablation rate is thus proportional to the square of the current $I(t)$ through the wires. We integrate Equation 3.5 to determine the total mass ablated at time t:

$$\Delta m = m(0) - m(t) = \frac{l\mu_0}{4\pi R_0 V} \int_0^t I^2(t')dt' \tag{3.6}$$

If we require the remaining mass $m(\tau) = \alpha m_0$ to be some fraction α of the initial mass m_0 after a current pulse of duration τ, we can determine the required initial mass per unit length as:

$$m_0/l = \frac{\mu_0}{4\pi R_0 V(1-\alpha)} \int_0^\tau I^2(t')dt' \tag{3.7}$$

Mass injected at $r = R_0$ at time t is spread over a larger area at $r = r$ at some later time $t' = t + (r - R_0)/V$:

$$\rho_0 V(2\pi l) R_0|_t = \rho(r) V(2\pi l) r|_{t'} = -\dot{m} \tag{3.8}$$

Substituting for the ablation rate $\dot{m}$, we can determine the radial mass density distribution at time t' as:

$$\rho(r,t') = \frac{\mu_0}{8\pi^2 R_0 r V^2}\left[I(t' - \frac{r-R_0}{V})\right]^2 \tag{3.9}$$

3.3 Resitive MHD Simulations of Wire Arrays

We use GORGON to simulate the dynamics of the plasma generated in a wire array. GORGON is a 3D resistive MHD two-temperature code developed by Chittenden et al. [2004]. GORGON solves the resistive magnetohydrodynamic equations explicitly using a forward Eulerian method in time. It uses a two-temperature model, which means that the ion and electrons have separate temperatures which equilibriate over some collisional time scale τ_{eq}. The electrons are heated resistively and undergo radiative cooling, while the ions are heated by compression and viscous heating. The electrons and ions exchange energy via collisons. GORGON has been used to successfully reproduce and study the dynamics of MHD shocks and wire array ablation (Chittenden et al. [2004]; Chittenden et al. [2004]; Harvey-Thompson et al. [2009]; Lebedev et al. [2014]; Burdiak et al. [2017]).

An important feature of plasma shocks is the intense emission of radiation associated with the post-shock plasma. The transition in energy states of electrons is accompanied by the emission or absorption of radiation. A plasma can emit radiation due to free-free electron transitions (Bremsstrahlung radiation), free-bound transitions (recombination radiation), and bound-bound transitions (line radiation). A magnetized plasma may also emit cyclotron emission associated with the gyro-motion of electrons around magnetic field lines. To accurately account for the change in internal energy due to radiative losses, we must solve the radiative transport equation and account for the spatially and temporally varying emissivities and absorbtivities of the plasma. However, solving the full radiative transport can be computationally restrictive, so GORGON uses a simple volumetric radiation loss model, which estimates the volumetric radiative power from each cell to be equal to the sum of the Bremsstrahlung and recombination loss from the plasma (Huba [2013]):

$$\dot{q}_{\mathrm{rad}} = KZ^2 n_e n_i T_e^{1/2} \left(1 + \frac{\Delta E^{Z-1}}{T_e}\right) \tag{3.10}$$

Here, n_e and n_i are the ion and electron densities respectively, T_e is the electron temperature, ΔE is the ionization energy, and K is a constant of proportionality. In GORGON, we use a value of $K = 3 \times 1.69 \times 10^{-38}$.

We also require a model for the equation-of-state (EOS) to relate the ionization state Z to the temperature and density of the plasma. In a plasma, collisions between electrons and ions can excite bound electrons to higher energy states, or even excite a bound electron into the continuum, making it a free electron. Similarly, ions and electrons can collide and recombine into an ion with a reduced charge — a process called collisional recombination. When the rates of collisional ionization and recombination are in detailed balance, the system is said to be in LTE (Drake [2013]). GORGON uses a numerical approximation to the LTE Thomas-Fermi model to predict the ionization state of the plasma. The Thomas-Fermi model solves for the potential field in each ion sphere (the region in space around the ion where the electrostatic influence of the ion is non-negligible) using the Poisson equation, which relates the Laplacian of the electric potential to the spatially-varying charge density in the ion sphere (Drake [2013]). Thomas-

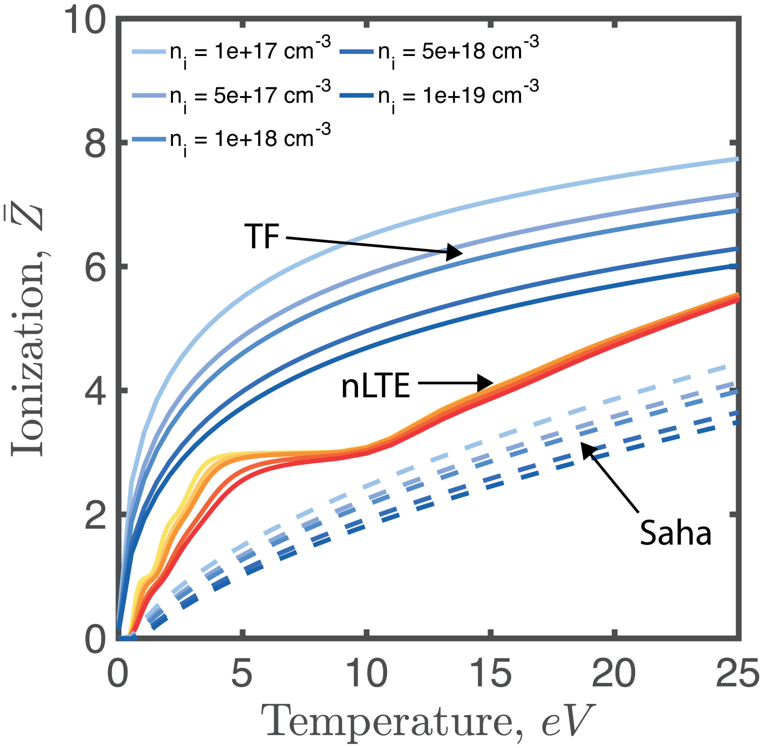

Figure 3-5: Comparison of LTE Thomas-Fermi (TF) and Saha ionziation models with a non-LTE tabulated ionization model for an Aluminum plasma. Darker colors represent increasing ion density. Thomas-Fermi tends to overpredict the ionization state, while the Saha model tends to underpredict the ionization state compared to the nLTE model

Fermi self-consistently solves for the spatially-varying electron density in the ion sphere.

Another commonly used LTE model is the Saha model. The Saha equation describes the equilibrium densities of ions in adjacent ionization states. We can estimate the degree of ionization of the plasma from the ionization state at which the rates of recombination and ionization are balanced. The Saha model predicts an average ionization level of (Drake [2013]):

$$Z \approx \sqrt{\frac{T_e}{E_H}}\sqrt{\ln\left[\frac{1}{n_e}\frac{g_j}{4g_k a_o^3}\left(\frac{T_e}{\pi E_H}\right)^{3/2}\right]} - \frac{1}{2} \tag{3.11}$$

Here, T_e is the electron temperature, n_e is the electron density, $g_{i,j}$ represent the degeneracies of adjacent states, and $E_H = 13.6$ keV is the energy require to ionize an electron from a hydrogen atom. The Saha model is typically limited because it does not include the effect of multiple ions (which can lower the ionization energy — a phenomenon called continuum lowering)(Drake [2013]).

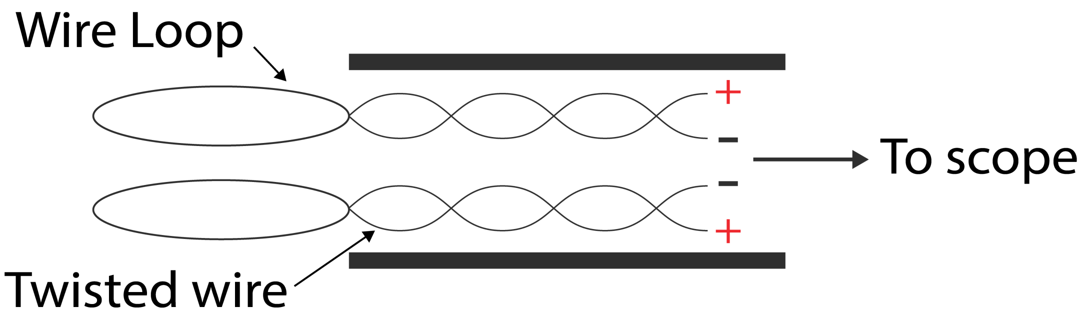

Figure 3-6: Schematic of a simple inductive probe with two oppositely-wound loops of conducting wire. A time-varying magnetic field induces a voltage in a wire loop equal to the time rate of change of the magnetic flux through the loop, which is read by the oscilloscope.

Both Saha and the Thomas-Fermi models compute the ionization state at LTE. However, plasmas can deviate from LTE. In non-LTE plasmas, using a LTE equation-of-state will add an additional uncertainty in the ionization state. In Figure 3-5, we compare the Thomas-Fermi and Saha models with a tabulated non-LTE ionization model (Chittenden et al. [2016]). For our temperatures of interest, Thomas-Fermi tends to overpredict the ionization state, while the Saha model tends to underpredict the ionization state compared to the nLTE model.

3.4 Diagnostics

We present three diagnostic techniques — (1) Inductive probes, (2) Laser Interferometry, and (3) Optical Thompson Scattering. We use inductive probes and laser interferometry to measure the magnetic field and plasma density respectively. We do not use Optical Thompson Scattering in the experiments presented in this thesis, but we introduce it here, because we hope to implement it in future experiments to determine the ion and electron temperatures, ionization, and velocity of the plasma.

3.4.1 Inductive Probes

An inductive probe is simply a loop of conducting wire, as illustrated in Figure 3-6. Inductive probes function due to Faraday's law of electromagnetic induction — a time-varying magnetic field induces a voltage in a wire loop equal to the time rate of change of the magnetic flux through the loop. The voltage response of the probe can have two contributions — one due to the time-varying magnetic flux through the loop, and another electrostatic component due to the coupling of stray voltages or the voltage from the pulsed-power generator. One method to isolate the magnetic component is to have two oppositely-wound loops in the inductive probe, which allows us to combine the signals from each loop and eliminate the contribution of the electrostatic component:

$$\begin{aligned} V_1 &= \dot{\Phi}_1 + \oint \mathbf{E}\cdot\mathbf{dl} \\ V_2 &= -\dot{\Phi}_2 + \oint \mathbf{E}\cdot\mathbf{dl} \\ V &= \frac{V_1 - V_2}{2} = N\dot{B}A_p \end{aligned} \tag{3.12}$$

Here, Φ is the magnetic flux, $\mathbf{E}$ is the electric field, N is the number of turns in the wire, B is the magnetic field , and $A_p = \mathbf{b}\cdot\mathbf{n}\,A_{\text{loop}}$ is the projection of the cross-sectional area of the loop along the magnetic field. The oppositely wound loops are placed next to one another, so that they experience approximately the same magnetic and electrostatic components.

The area of the probe A_p can differ from the geometric area of the loop because of skin effects. One way to determine the effective area is to calibrate the probe by placing it in a known magnetic field. We get localized measurements of the magnetic field from inductive probes. For effective measurements, the length scale of variation of the magnetic field must be small compared to the size of the probe.

3.4.2 Laser Interferometry

Laser interferometry is an imaging technique used to measure the line-integrated electron density. It has been used in pulsed-power plasmas to visualize the plasma flow (Swadling et al. [2013];Lebedev et al. [2014]; Burdiak et al. [2017]). Laser interferometry is based on the principle of interference of two electromagnetic waves with different phases. In a typical interferometry setup like the Mach-Zehnder interferometer shown in Figure 3-7, a monochromatic beam is split into a reference and a probe beam using a beamsplitter. The probe beam then propagates through the plasma, while the reference beam propagates via air or vacuum. Since the refractive index of the plasma is different from that of vacuum, the probing beam accumulates a different phase compared to the reference beam as it propagates through the plasma. The reference and probe beams, which now have a relative phase difference between them, interfere at the target. The phase difference between the two beams can be determined from the intensity at the

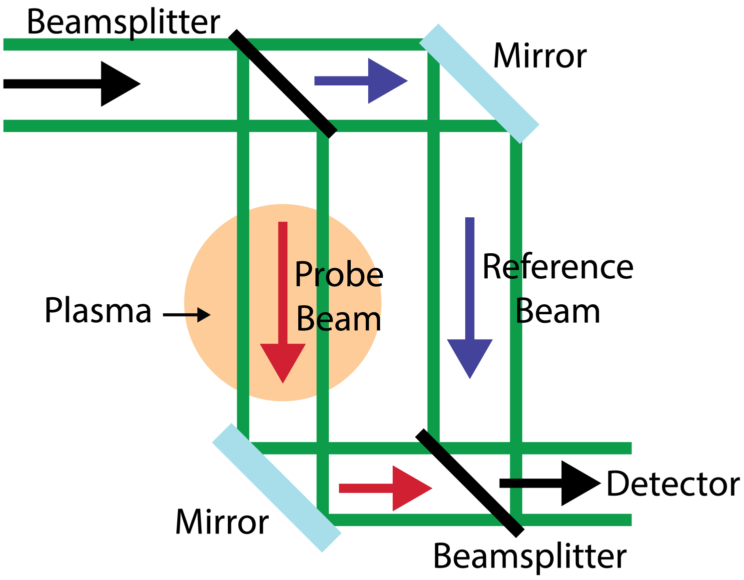

Figure 3-7: Schematic of a simple Mach-Zehnder interferometer.

detector, and the phase difference can then be related to the electron density.

Consider two monochromatic plane electromagnetic waves:

$$\begin{aligned}\mathbf{E}_r &= \mathbf{E}_{r,0}e^{-i\omega t}e^{i\mathbf{k_r}\cdot\mathbf{x}}\\ \mathbf{E}_p &= \mathbf{E}_{p,0}e^{-i\omega t}e^{i\mathbf{k_p}\cdot\mathbf{x}}\end{aligned} \tag{3.13}$$

The reference wave $\mathbf{E_r}$ and probe wave $\mathbf{E_r}$ interfere at the detector. The total field becomes:

$$\mathbf{E}_t = \mathbf{E}_r + \mathbf{E}_p = \left(\mathbf{E}_{r,0}e^{i\mathbf{k_r}\cdot\mathbf{x}} + \mathbf{E}_{p,0}e^{i\mathbf{k_p}\cdot\mathbf{x}}\right)e^{-i\omega t} \tag{3.14}$$

The total intensity is:

$$\begin{aligned}I_t &= \mathbf{E}_t\cdot\mathbf{E}_t^*\\ I_t &= |\mathbf{E_{r,0}}|^2 + |\mathbf{E_{p,0}}|^2 + \mathbf{E_{r,0}}\cdot\mathbf{E_{p,0}}\left[e^{i(\mathbf{k_1}-\mathbf{k_2})\cdot\mathbf{x}} + e^{-i(\mathbf{k_1}-\mathbf{k_2})\cdot\mathbf{x}}\right]\end{aligned} \tag{3.15}$$

Using the Euler expression $e^{i\theta} + e^{-i\theta} = 2\cos\theta$, we get:

$$I_t = |\mathbf{E_{r,0}}|^2 + |\mathbf{E_{p,0}}|^2 + 2\mathbf{E_{r,0}}\cdot\mathbf{E_{p,0}}\cos\left[(\mathbf{k_1}-\mathbf{k_2})\cdot\mathbf{x}\right] \tag{3.16}$$

Or:

$$I_t = (|\mathbf{E_{r,0}}|^2 + |\mathbf{E_{p,0}}|^2)\left(1 + \frac{2\mathbf{E_{r,0}} \cdot \mathbf{E_{p,0}}}{|\mathbf{E_{r,0}}|^2 + |\mathbf{E_{p,0}}|^2} \cos\Delta\phi\right) \tag{3.17}$$

Where $\Delta\phi = (\mathbf{k_1} - \mathbf{k_2}) \cdot \mathbf{x}$ is the phase difference between the reference and probe beams.

In general, the phase accumulated by an electromagnetic wave for a slowly-varying medium is (Hutchinson [2002]):

$$\phi = \int \mathbf{N} \cdot \mathbf{dl} \tag{3.18}$$

Here, $\mathbf{N} = \mathbf{k}^2 c^2/\omega$ is the refractive index.

In the absence of the plasma, the probe and reference beams have the same refractive index $N \approx 1$, and accumulate the same phase, so that the phase difference is zero, i.e. $\Delta\phi = (\mathbf{k_1} - \mathbf{k_2}) \cdot \mathbf{x} = 0$. In this case, the detector reads a constant intensity. In the presence of the plasma, $\mathbf{k_1} \neq \mathbf{k_2}$, so a phase difference is introduced between the probe and reference beams, and the detector reads a modulated intensity $I_t/I_0 \sim (1 + \cos\Delta\phi)$ depending on whether the probe and reference beams interfere constructively or destructively.

The variation in the detected intensity varies as $\cos\Delta\phi$. Therefore, phases that are separated by 2π have the same intensity, which makes it difficult to uniquely determine the density and direction of change of the phase. To overcome this issue, we introduce a deliberate misalignment between the probe and reference beams (Hutchinson [2002]; Swadling et al. [2013]). The misalignment introduces a spatially varying phase difference between the probe and reference beams (even when there is no plasma), such that an interference pattern of bright and dark fringes forms at the detector, as shown in Figure 3-8c. Consider an interferometer where the wavevectors of the probe and reference beams are misaligned with an angle 2α between them. The intensity at the detector is given by 3.16. If we assume that $E_{p,0} \approx E_{r,0} \equiv E_0$, then we can write the intensity at the detector as:

$$\frac{I_t}{2E_0^2} = 1 + \cos\left[(\mathbf{k_1} - \mathbf{k_2}) \cdot \mathbf{x}\right] \tag{3.19}$$

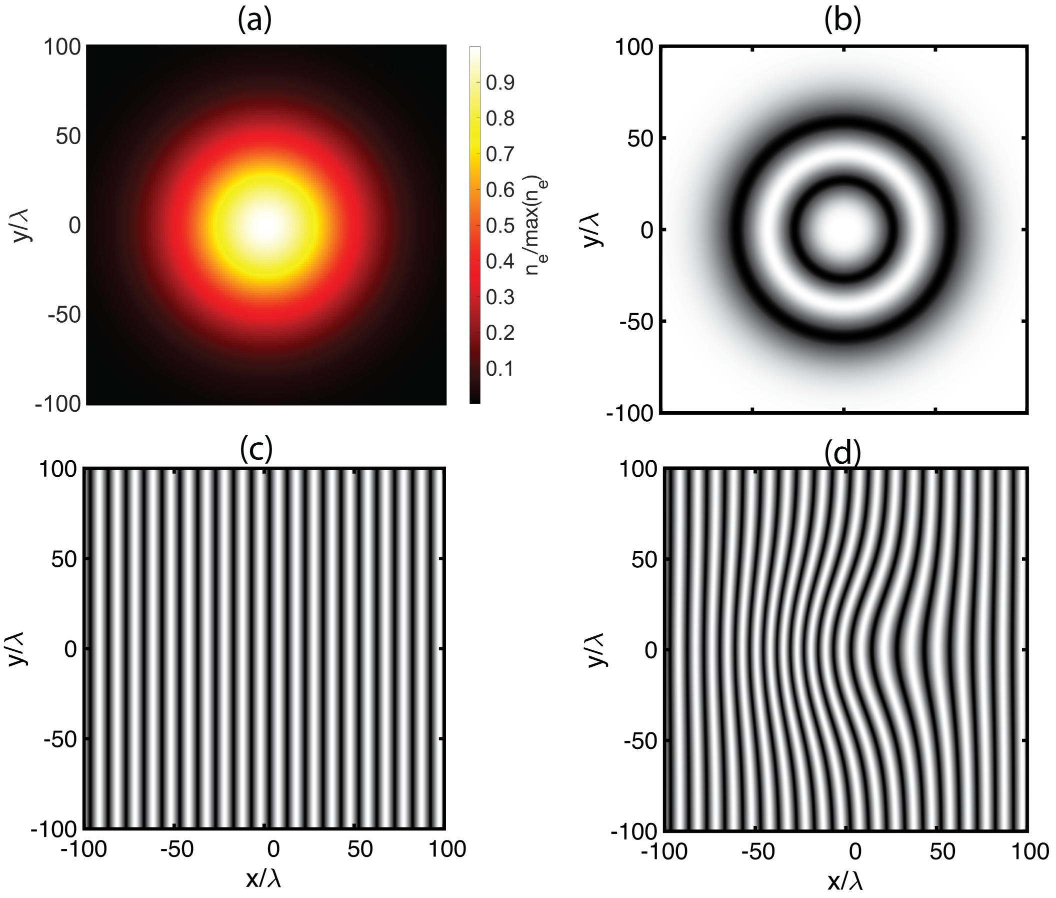

Figure 3-8: (a) Synthetic electron density map. The plasma electron density is modeled as a radially varying Gaussian function with a standard deviation of 50 λ. We have normalized the spatial axis with the probing laser wavelength. (b) Synthetic interferogram in a spatially homodyned system, where there is no misalignment between the probing and reference beams. (c) Background interferogram in the absence of plasma in a spatially heterodyned system. A slight misalignment between the probe and laser beams produces an interference pattern of dark and bright fringes. (d) Synthetic interferogram in the presence of the plasma. The phase introduced by the plasma distorts the pattern of bright and dark fringes. We have ignored any shadowgraphy effects due to density gradients, and any emission and absorption of radiation by the plasma in generating the synthetic interferograms.

For the configuration shown in Figure, we can write the phase difference as:

$$(\mathbf{k_1}-\mathbf{k_2})\cdot\mathbf{x} = \begin{pmatrix} k\cos\alpha \\ k\sin\alpha \end{pmatrix} - \begin{pmatrix} k\cos\alpha \\ -k\sin\alpha \end{pmatrix} = 2k\sin\alpha y \tag{3.20}$$

Combining this result with Equation 3.19, we observe that in the absence of any plasma, the intensity at the detector is modulated in the y-direction with a wavenumber $k_{\mathrm{mod}} = 2k\sin\alpha$. For small $\alpha \ll 1$, we can approximate the intensity as:

$$\frac{I_t}{2E_0^2} \approx 1+\cos\left(2k\alpha y\right) \tag{3.21}$$

Here, k is the wavenumber of the probe and reference beams, and α is half the angle between them. Therefore, we can see that the interferogram comprises a linear pattern of dark ($2k\alpha y = n\pi, n = \pm 1, 3, 5, ...$) and bright fringes ($2k\alpha y = m\pi, m = \pm 0, 2, 4, ...$), with a fringe separation (between successive bright or dark fringes) of $\Delta\lambda = \pi/k\alpha$. This is shown in Figure 3-7c, where we have generated a synthetic interferogram from the interference of two electromagnetic waves with a slight misalignment between them.

The presence of the plasma adds an additional phase ϕ_p to the probe beam. Using the ansatz $\phi_p \approx \nabla\phi_p \cdot \mathbf{x}$, we can express the intensity as:

$$\frac{I_t}{2E_0^2} = 1 + \cos\left[(\mathbf{k_1} - \mathbf{k_2} + \nabla\phi_\mathbf{p}) \cdot \mathbf{x}\right] \tag{3.22}$$

The phase introduced by the plasma now changes the wavenumber of the modulation, and allows us to determine both the magnitude and the direction of change of phase. In regions where the phase in increasing with distance along the direction of propagation, i.e $\nabla\phi_p > 0$, the fringes are closer. Similarly, where the phase decreases with distance, i.e $\nabla\phi_p < 0$, the fringes are spaced further apart.

The introduction of a phase ϕ_p distorts the spatially uniform fringe pattern in a spatially heterodyned interferometry system, as shown in Figure 3-8d. All that remains is to relate the phase to the electron density n_e of the plasma. In order to do so, we need to determine the refractive index of the plasma, which requires solving for the dispersion relation of electromagnetic waves in a plasma.

We present the full derivation of the EM wave dispersion relation in Appendix A for the interested reader. Here, we shall only consider the case where the gyration frequency of electrons is much smaller than the frequency of the EM wave, i.e. $\Omega_c \equiv \frac{eB}{m} \ll \omega_{pe} \ll \omega$. Here, B is the magnetic field strength, e is the electron charge, and m is the electron mass. For our plasmas with typical values of $B \sim 10$ T, $n_e \sim 10^{18}$ cm^{-3}, the electron gyro frequency is $\Omega_c \sim 2 \times 10^{12}$ rad s^{-1}, which is much smaller than the typical laser frequencies $\omega = c/k \sim 10^{15}$ rad s^{-1} used for laser plasma diagnostics. In this limit, the principal mode of propagation is the ordinary wave (or O-wave), which has the dispersion relation (Hutchinson [2002]):

$$N^2 = \frac{k^2 c^2}{\omega^2} = 1 - \frac{\omega_p^2}{\omega^2} \tag{3.23}$$

Here, $\omega_p = n_e e^2/m\epsilon_0$ is the electron plasma frequency.

When the wave frequency equals the electron plasma frequency $\omega = \omega_p$, the wave is cut-off. When $\omega < \omega_p$, the wave vector k becomes imaginary and oscillatory solutions are not possible. The wave is said to be evanescent and is damped exponentially. The cut-off or critical plasma density n_c is:

$$n_c = \frac{\omega^2 m\epsilon_0}{e^2} \tag{3.24}$$

And the refractive index can be written as:

$$N^2 = 1 - n_e/n_c \tag{3.25}$$

The phase difference $\Delta\phi$ between the reference beam and the probing beam is:

$$\Delta\phi = \int (\boldsymbol{k_1} - \boldsymbol{k_2}) \cdot \boldsymbol{dl} = \frac{\omega}{c}\int 1 - \sqrt{1 - \omega_p^2/\omega^2}\, dl \tag{3.26}$$

In the limit where $\omega_p^2/\omega^2 << 1$, we can write Equation 3.26:

$$\Delta\phi = \frac{1}{2c\omega}\int \omega_p^2 dl = \frac{\omega}{2cn_c}\int n_e dl \tag{3.27}$$

Thus, the phase difference between the reference and probe beams is proportional to the line integrated plasma density.

3.4.3 Optical Thompson Scattering

Optical Thompson Scattering (OTS) is a powerful diagnostic technique that can provide information about the density, temperature, ionization, and velocity of a plasma. It is another commonly used diagnostic technique in pulsed-power driven plasmas (Harvey-Thompson et al. [2012]; Burdiak et al. [2017]; Hare et al. [2018]; Suttle et al. [2021]). In OTS, we illuminate a small volume of the plasma with a monochromatic laser beam. The electrons in the plasma accelerate in response to the electromagnetic field of the incident radiation. The accelerating charges in the scattering volume emit radiation in all directions (except along the electric field) — this is called the scattered radiation which typically exhibits a power spectrum different from the incident light. We collect the scattered radiation at some angle θ to the direction of propagation of the incident beam, and by measuring the scattered spectrum with a spectrometer, we can determine several important properties of the plasma. Scattering from a plasma in the non-relativistic regime

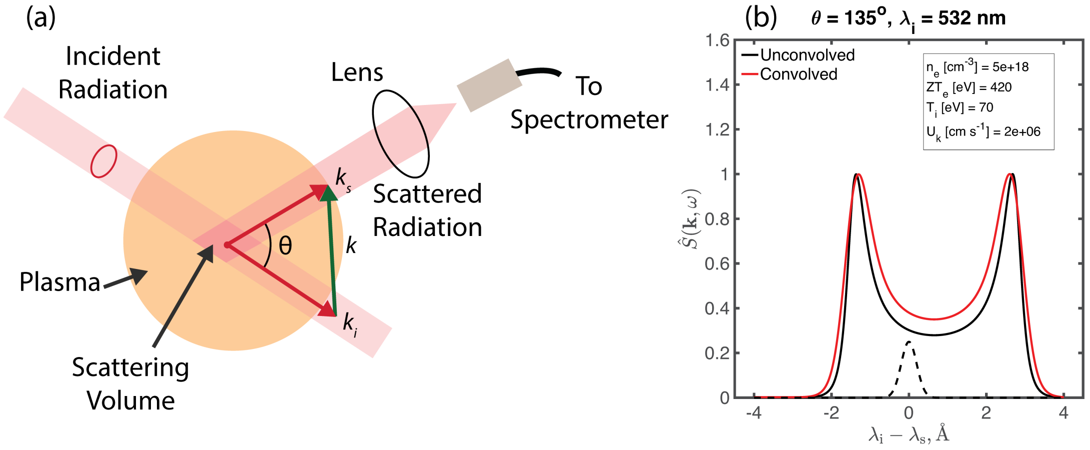

Figure 3-9: (a) Schematic of a simple Optical Thompson Scattering setup. An electromagnetic wave with the wave vector $\mathbf{k_i}$ illuminates the scattering volume. We collect the scattered radiation (which has some wave vector $\mathbf{k_s}$) at an angle θ to the incident wave. The spectrum of the scattered radiation is measured with a spectrometer. (b) A synthetic spectral density function showing well separated ion acoustic peaks. The spectral density function is convolved with the spectrometer response function (a Gaussian function with $\sigma = 2$Å to generate the expected signal. The spectral density function is Doppler shifted due to the velocity of the moving plasma.

is called Thompson scattering. Similarly, scattering from relativistic plasmas is called Compton scattering. The plasmas of interest in this thesis are non-relativistic plasmas, so their scattered radiation can be described well with the theory of Thomson scattering (Sheffield et al. [2010]).

We do not provide the full theory of Thompson scattering here, but only summarize the key results. The full derivation based on the treatment by Sheffield et al. [2010] and Hutchinson [2002] is provided in Appendix B for the interested reader. Consider an electromagnetic wave with the wave vector $\mathbf{k_i}$ and angular frequency ω_i which illuminates a small scattering volume within the plasma, as shown in Figure. We collect the scattered radiation (which has some frequency ω_s and wave vector $\mathbf{k_s}$) at a distance R along the direction $\hat{\mathbf{s}}$. We define the scattering wave vector and the scattering frequency as $\mathbf{k} = \mathbf{k_s} - \mathbf{k_i}$ and $\omega = \omega_s - \omega_i$ respectively. The total scattered electric field will have contributions from all electrons in the scattering volume, so we integrate the power over the electron distribution function and represent the average power as the ensemble-averaged power. We calculate the time-averaged power per unit solid angle per unit frequency interval from the Fourier transform of the total energy flux along the scattering direction $\hat{\mathbf{s}}$. The ensemble-averaged scattered power spectrum for non-relativistic scattering is (Sheffield et al. [2010]):

$$\left\langle \frac{d\bar{P}}{d\Omega_s d\omega_s} \right\rangle = \frac{q_{in} r_e^2}{2\pi} \left[\hat{\mathbf{s}} \times (\hat{\mathbf{s}} \times \hat{\mathbf{E}}_{\mathbf{io}}) \right]^2 e^{ik_s R} N S(\mathbf{k}, \omega) \tag{3.28}$$

Where $q_{in} = cE_{i0}^2/(4\pi)$ is the magnitude of the incident energy flux, $r_e = e^2/m_e c^2$ is the classic electron radius, $\mathbf{E_{i0}}$ is the incident electric field, $\hat{\mathbf{s}}$ is the scattering direction, k_s is the wave number of the scattered radiation, ω_s is the frequency of the scattered radiation, Ω is the solid angle, and N is the total number of electrons in the scattering volume.

$S(\mathbf{k}, \omega)$ is called the spectral density function. It determines the shape of the power spectrum in frequency space, and is a function of the scattering wave vector $\mathbf{k}$ and the scattering frequency ω. The spectral density function is defined as (Sheffield et al. [2010]):

$$S(\mathbf{k}, \omega) \equiv \lim_{T\to\infty, V\to\infty} \frac{1}{TV} \left\langle \frac{|n_{\mathrm{e}}(\mathbf{k}, \omega)|^2}{n_{eo}} \right\rangle \tag{3.29}$$

Here, $n_e(\mathbf{k}, \omega)$ is the Fourier transform of the electron density $n_e(\mathbf{r}, t)$, and n_{e0} is the average electron density of the scattering volume. For a non-relativistic, unmagnetized collissionless plasma, we can show that the spectral density function has the form (Sheffield et al. [2010]):

$$S(\mathbf{k}, \omega) = \frac{2\pi}{k} \left| 1 - \frac{\chi_e}{\epsilon} \right|^2 \hat{f}_{eo}\left(\frac{\omega}{k}\right) + \frac{2\pi Z}{k} \left| \frac{\chi_e}{\epsilon} \right|^2 \hat{f}_{io}\left(\frac{\omega}{k}\right) \tag{3.30}$$

Here, Z is the ionization, $\hat{f}_0$ is the 1D normalized Maxwellian distribution, and χ_i and χ_e are the electric susceptibilities of the ions and electrons respectively, which are related to the plasma dielectric constant:

$$\epsilon = 1 + \chi_e + \chi_i \tag{3.31}$$

We can show that for an unmagnetized collisionless plasma, the electric susceptibilities are (Sheffield et al. [2010]):

$$\chi_s = \frac{1}{(\lambda_D k)^2} \left(\frac{Z_s T_e}{T_i} \right) w \left(\frac{\omega}{k v_{th,s}} \right) \tag{3.32}$$

Here, λ_D is the Debye length, T_e and T_i are electron and ion temperatures, and $v_{\mathrm{th,s}}$ is the thermal velocity of species s. w is the derivative of the plasma dispersion function, which we can write in terms of the Dawson integral:

$$\begin{aligned} w(z_0) &= 1 + i\sqrt{\pi} z_0 e^{-z_0^2} - 2z_0 D_+(z_0) \\ D_+(x) &= e^{-x^2}\int_0^x e^{t^2}\,dt \end{aligned} \tag{3.33}$$

The 1D normalized Maxwellian distribution is:

$$\hat{f}_s = \left(\frac{1}{\pi v_{th,s}^2}\right)^{1/2} \exp(-v^2/v_{th,s}^2) \tag{3.34}$$

$$v_{th,s} = \sqrt{\frac{2k_b T_s}{m_s}} \tag{3.35}$$

The scattering wave vector is:

$$\begin{aligned} \mathbf{k} &= \mathbf{k_s} - \mathbf{k_i} \\ k &= \sqrt{k_i^2 + k_s^2 - 2k_s k_i \cos\theta} \end{aligned} \tag{3.36}$$

The scattering frequency is:

$$\begin{aligned} \omega &= \omega_s - \omega_i \\ \omega_{s,i} &= \sqrt{c^2 k_{i,s}^2 + \omega_{pe}^2} \end{aligned} \tag{3.37}$$

$$\omega_{pe} = \left(\frac{4\pi n_e e^2}{m_e}\right)^{1/2} \tag{3.38}$$

Here, ω_{pe} is the electron plasma frequency.

When the electron fluid is non-stationary and moves with a velocity $\mathbf{V}$, the scattered frequency is Doppler shifted by $\mathbf{V}\cdot\mathbf{k}$. The scattered frequency is then:

$$\omega_s = \sqrt{c^2 k_s^2 + \omega_{pe}^2} + \mathbf{V}\cdot\mathbf{k} \tag{3.39}$$

The spectral density of the scattered radiation (Equation 3.30) has contributions from both the ion and electron fluids. The scattered radiation also exhibits resonances at the electron plasma wave and ion acoustic wave frequencies (Sheffield et al. [2010]). These appear as peaks in the spectral density function, which are typically damped by Landau and collisional damping. The ion acoustic feature, which are low frequency peaks that appear at the ion acoustic frequency, is of particular interest. Figure 3-9b shows a sythentic OTS spectrum with well-defined ion acoustic peaks. The peak separation, peak width, and the Doppler shift allow us to discern information about the ion and electron temperatures, ionisation, and velocity of the plasma (Sheffield et al. [2010]). We provide more discussion on the application of the OTS ion feature to plasmas of interest in Chapter 5.

The spectral density function (Equation 3.30) and the electric susceptibilities (Equation 3.32) are derived for non-relativistic unmagnetized collisionless plasmas. These assumptions require further elaboration. The first, that of a non-relativistic plasma, is satisfied when the characteristic velocity V of the plasma is small compared to the light speed c, i.e. $V/c \ll 1$. The laboratory plasmas presented in this thesis exhibit velocities $\sim 100\,\mathrm{km\,s^{-1}}$, so this criterion is easily satisfied. Next, we assume that the plasma is collisionless and unmagnetized, which at first glance, does not seem to apply to our system. Typically, a plasma is collisionless if the mean free path of collisions λ_{mfp} is comparable to the length scale L of the plasma. Similarly, the plasma is said to be magnetized is the gyro-frequency Ω_c is small compared to the characteristic frequency of the plasma $1/\tau$. From Table 3.1, $\lambda_{\mathrm{mfp}}/L \ll 1$ and $\Omega_e\tau \gg 1$ for our plasmas of interest, so the plasma is highly collisional and magnetized (Suttle et al. [2019]; Burdiak et al. [2017]). Therefore, it seems paradoxical to assume a collisional unmagnetized plasma in our derivation.

This apparent paradox is resolved if we consider that the plasma can still be collisionless and unmagnetized with respect to the oscillating EM fields of the propagating laser beams, i.e. $\nu/\omega_{i,s} \ll 1$ and $\Omega_c/\omega_{i,s} \ll 1$ (Sheffield et al. [2010]). Here, ν is the frequency of collision between the ions and electrons, and Ω_c is the ion or electron gyro-frequency. The EM fields of the propagating laser beams oscillate at a much smaller time scale compared to the time scales at which the electron and ions collide and gyrate, and the plasma appears effectively collisionless and unmagnetized to the incident and scattered waves.

3.5 Summary of Pulsed-Power Machines and Z-Pinch Wire Arrays

We use pulsed-power machines to drive a fast-rising high-amplitude current pulse through an inductive load. Pulsed-power machines, like the MAGPIE generator at Imperial College London, achieve this by discharging the capacitors in the Marx banks, and compressing the resulting current pulse using the Pulse Forming Lines. The Output Transmission Line and the Magnetically Insulated Transmission Line (MITL) deliver the current pulse to the load which sits in a vacuum chamber. We use an exploding wire array as the load in our pulsed-power experiments to generate a highly-collisional radially diverging magnetized plasma. An exploding wire array consists of a cylindrical set of wires arranged around a central conductor. When the current flows through the wires, the mass in the wires vaporizes and ionizes to form a ring of coronal plasma, which is pushed radially outwards by the strong magnetic pressure inside the array. We can estimate the rate of ablation in a wire array using the Rocket model, which estimates the mass ablation rate to be proportional to the square of the total current in the wires. We present three diagnostic techniques — inductive probes, plasma interferometry, and Optical Thompson Scattering (OTS). Inductive probes, which work based on Faraday's law of electromagnetic induction, measure the time rate of change of magnetic flux through the probe. Laser interferometry, which allows us to determine the line-integrated electron density, is a refractive index measurement based on the interference of two electromagnetic waves with a relative phase between them. Finally, OTS is based on the scattering of light by the plasma, and can help us determine the ion and electron temperatures, ionization, and velocity of the plasma.

Chapter 4

Bow Shocks in Supersonic Super-Alfvénic aluminum Plasma

In this chapter, we investigate 3D bow shocks in a highly collisional magnetized aluminum plasma, generated during the ablation phase of an exploding wire array on the MAGPIE facility (1.4 MA, 250 ns) [1]. Ablation of plasma from the wire array generates radially diverging, supersonic ($5 < M_1 < 8$), super-Alfvénic magnetized flows with frozen-in magnetic flux ($Re_m >> 1$). These flows collide with inductive probes placed in the flow, which serve both as the obstacles that generate the magnetized bow shocks, and as diagnostics of the advected magnetic field and flow velocity. Laser interferometry is used to diagnose the line-integrated electron density. A detached bow shock forms ahead of the probe and exhibits a fully 3D structure. The shock opening-angle is larger in the plane parallel to the magnetic field than in the plane perpendicular to the field. We calculate the the shock Mach angle from the shock geometry to determine the Mach number of the upstream flow. The Mach angles are ~11° and ~7° in the parallel and perpendicular planes respectively. Inductive probe measurements show that the peak post-shock magnetic field is ~ 14 T. We determine the velocity of the flow from the time of flight of the plasma to the probe, and by combining this information with the observed shock geometry, we estimate the temperature of the plasma. The velocity and electron temperature are in good agreement with values reported from Thompson scattering measurements in similar flows. Finally, we compare the experimental results with fully 3D simulations performed using the resistive MHD code GORGON.

---

[1] The experimental data reported here were collected by personnel at the MAGPIE facility, Imperial College London, in 2016. The author is responsible for the analysis and interpretation of the collected data.

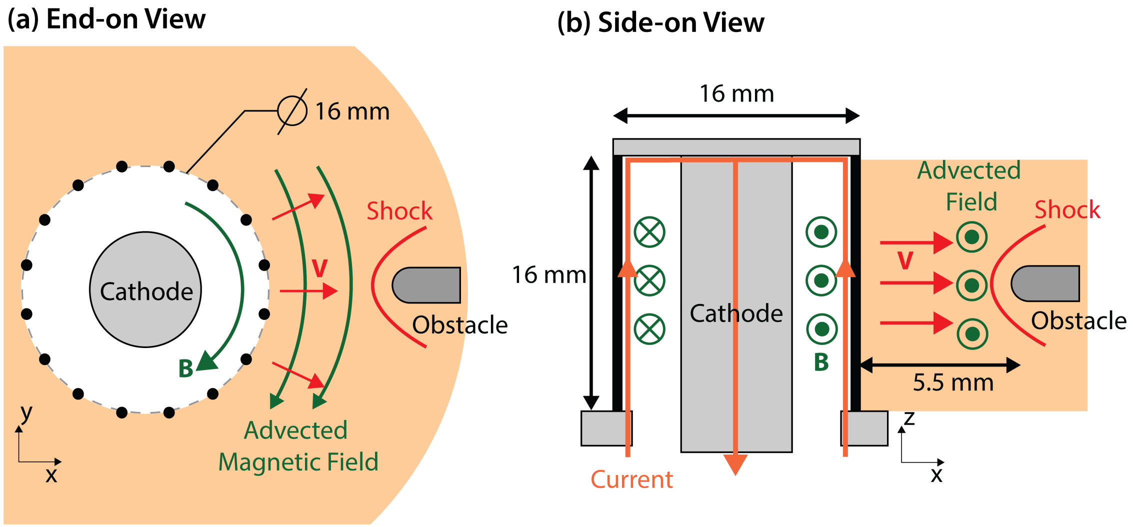

Figure 4-1: Experimental setup showing the exploding wire array and obstacle configuration. (a) End-on (xy-plane) view of the experimental geometry, showing a cylindrical array of 16 equally-spaced 30 µm Al wires around a central cathode. The array diameter is 16 mm and the array height is 16 mm. An inductive probe serves as the obstacle and is placed ~ 5.5 mm from the array surface. The magnetic field lines lie parallel to the end-on plane, and point in the azimuthal direction with respect to the center of the array. (b) Side-on (xz-plane) view of the experimental geometry. In the side-on plane, the magnetic field lines ahead of the obstacle lie perpendicular to the plane, and point out of the page.

4.1 Experimental and Diagnostic Setup

The experimental setup is illustrated in Figure 4-1. The load consists of a cylindrical array of 16 equally-spaced 30 µm diameter aluminum wires around a central stainless steel cathode. The array diameter and the array height are both 16 mm. The load is placed within a vacuum chamber that sits atop the MITL of the pulsed-power generator. The current pulse (1.4 MA peak current, 250 ns rise time) is generated using the MAGPIE generator at Imperial College London.

When current flows through the wires, the wires heat up resistively. The wire material vaporizes and ionizes to create a ring of low-density coronal plasma around the dense wire cores. Current density is mostly concentrated within a thin skin region containing the coronal plasma immediately around the stationary wire cores. The global $\mathbf{j} \times \mathbf{B}$ Lorentz force accelerates the coronal plasma radially outwards, and the ablating plasma streams supersonically into the flow region around the array. The ion-ion mean free path of the ablating plasma is typically small ($\lambda_{ii}/a \ll 1$), and the magnetic Reynolds number is typically large $Re_m \sim 10-100$ (Suttle et al. [2019]). The ablating plasma advects some of the current density and the magnetic field at the array surface radially outwards, resulting in outflows of highly collisional magnetized plasma. The velocity of the ablating plasma in similar setups is typically supersonic $M_S \sim 5$ and super-fast $M_f \sim 2$ (Burdiak et al. [2017]; Suttle et al. [2019]). When these hypersonic outflows collide with the obstacles, they generate detached bow shocks.

In contrast to previous experimental work, an inductive probe serves as the obstacle, and is placed 5.5 mm from the array surface. The probe consists of two strands of enamel-coated wire, threaded through a ~ 1 mm diameter thin steel tube. In addition to generating bow shocks, the probe also measures the post-shock magnetic field. We use a laser interferometry imaging system to visualize the plasma flow and the bow shock. The interferometry system provides line-integrated side-on (x-z plane) and end-on (x-y plane) views of the experimental setup. Note that throughout this chapter, we use a coordinate system positioned at the intersection of the obstacle axis and the wire array surface.

4.1.1 Inductive Probes

In addition to the inductive probe placed in the flow, a second inductive probe is placed in a recess inside the MITL (magnetically insulated transmission line) of the pulsed-power machine, and is used to monitor the current in the load. The signal from the probes is recorded using an oscilloscope with a 1 ns digitization rate.

The probe placed in the flow consists of two oppositely-wound single-turn loops of conducting wire in a thin steel tube, as illustrated in Figure 3-6. Having two oppositely-wound loops in the inductive probe allows us to combine the signals from each loop and isolate the contribution of the time-varying magnetic flux.

$$\begin{aligned} V_1 &= \dot{\Phi}_1 + V_E \\ V_2 &= -\dot{\Phi}_2 + V_E \\ V &= \frac{V_1 - V_2}{2} = N\dot{B}A_p \end{aligned} \tag{4.1}$$

Here, Φ is the magnetic flux, $\mathbf{E}$ is the electric field, N is the number of turns in the wire, B is the magnetic field , and $A_p = \mathbf{b}\cdot\mathbf{n}\,A_{\text{loop}}$ is the projection of the cross-sectional area of the loop along the magnetic field.

We position the inductive probe to measure the azimuthal magnetic field (with respect to the array center); the normals to the surfaces of the loops lie along the magnetic field. The inductive probe was calibrated before use in the experiment to determine the effec-

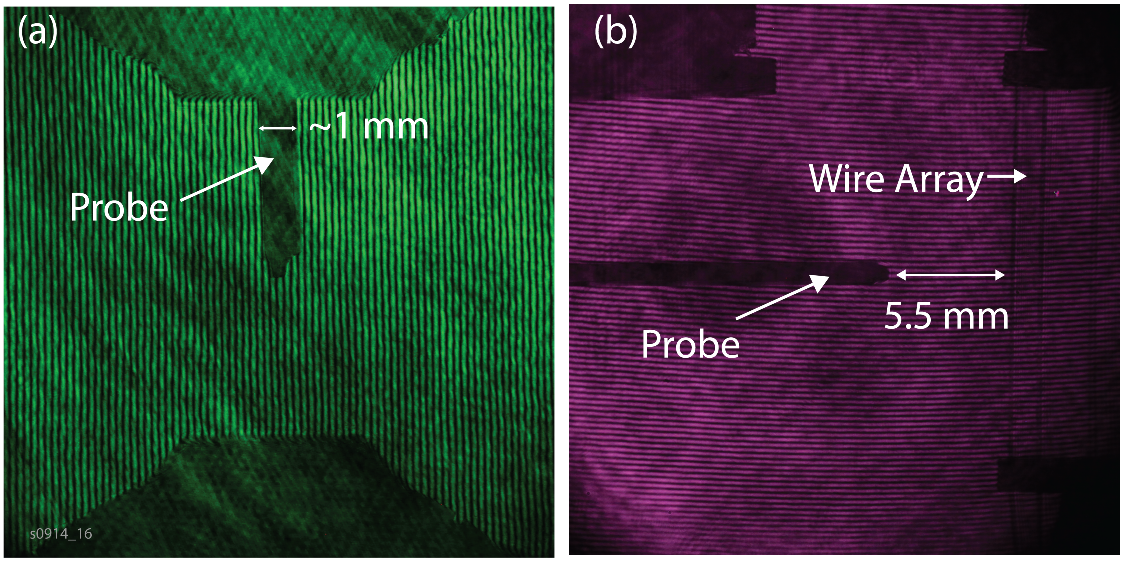

Figure 4-2: (a) Raw end-on interferogram of the experimental set-up the the absence of plasma. This view is illuminated using a 532 nm pulsed Nd-YAG laser. (b) Raw side-on interferogram of the experimental set-up the the absence of plasma. This view is illuminated using a 1053 nm Nd:Glass laser. The probe and reference beams are slightly misaligned to generate a spatially heterodyned system. In the absence of plasma, this creates a linear pattern of bright and dark interference fringes.

tive area A_p of the probe. This was done by placing the probe within the known magnetic field generated by a ~ 1 kA time-varying current. The effective areas of the probe determined from the calibration is $A_{\text{eff}} = 0.295 \pm 0.01$ mm^2.

The voltage signal from the probe is proportional to the time-rate of change of the magnetic field. To determine the magnetic field strength at the probe, we integrate the signal in time with the initial condition $B(t = 0) = 0$.

In pulsed-power systems, inductive probes are a good diagnostic of the magnetic field only until the time of peak current. After peak current, magnetic insulation in the MITL becomes weaker and breakdown can occur. The current can take complicated paths through the system, and the measurement of the current in the MITL using the inductive probe is no longer a good proxy for the behaviour of the current in the load itself.

4.1.2 Laser Interferometry

We use a Mach-Zehnder interferometry system to visualize the plasma flow and to determine the line-integrated electron density. Our interferometry system is set up to provide both end-on and side-on views of the experimental setup. The end-on (x-y plane) view provides an axially integrated view of the experimental setup. This view is shown in Figure 4-2a. This line-of-sight is illuminated using a 532 nm pulsed Nd-YAG laser with a pulse width of 150 ps. The pulse width sets the coherence length and the temporal resolution of the interferometry system. The side-on view provides a line-integrated (along the y-direction) view of the x-z plane. This view is shown in Figure 4-2b. It is illuminated using a 1053 nm Nd:Glass laser.

We combine the probe beam (which passes through the plasma) and the reference beam (which passes through air/vacuum) at the CCD of a DSLR camera. The probe and reference beams are slightly misaligned to generate a spatially heterodyned system. In the absence of plasma, this creates a linear pattern of bright and dark interference fringes. When the probe beam propagates through the laser, the resulting phase accumulated by the beam distorts the fringe pattern and introduces a spatially-varying fringe shift. We use the observed fringe shift to determine the phase difference between the probe and reference beams, and to calculate the line-integrated electron density (Hare et al. [2019]).

4.2 Electron Density Measurements and Shock Morphology

Figure 4-3 shows the end-on and side-on raw interferograms and the processed line-integrated electron density maps captured at 300 ns after current start. The phase accumulated by the probing beam distorts the linear fringe pattern in the raw interferograms. A detached bow shock, characterized by a curved discontinuity in electron density, is visible in both end-on and side-on images. Note that the bow shock is more distinct on the top of the probe in both end-on and side-on images. This is because the shock front is almost parallel to the fringes under the probe, so the fringes remain relatively undisturbed. The shock front appears distinct on the other side of the probe, where the fringes are at an angle to the shock.

The upstream electron density is not constant ahead of the obstacle. In both end-on and side-on images, the electron density is high near the surface of the wire array and decreases with distance from the array. In the end-on plane, the upstream flow exhibits significant modulation in the azimuthal direction. The azimuthal modulation in electron density results from the supersonic collision of adjacent jets emanating from the wire cores, which forms hot dense standing oblique shocks. We discuss oblique shocks in more detail in Chapter 5. Due to the oblique shocks, we expect the Mach number of

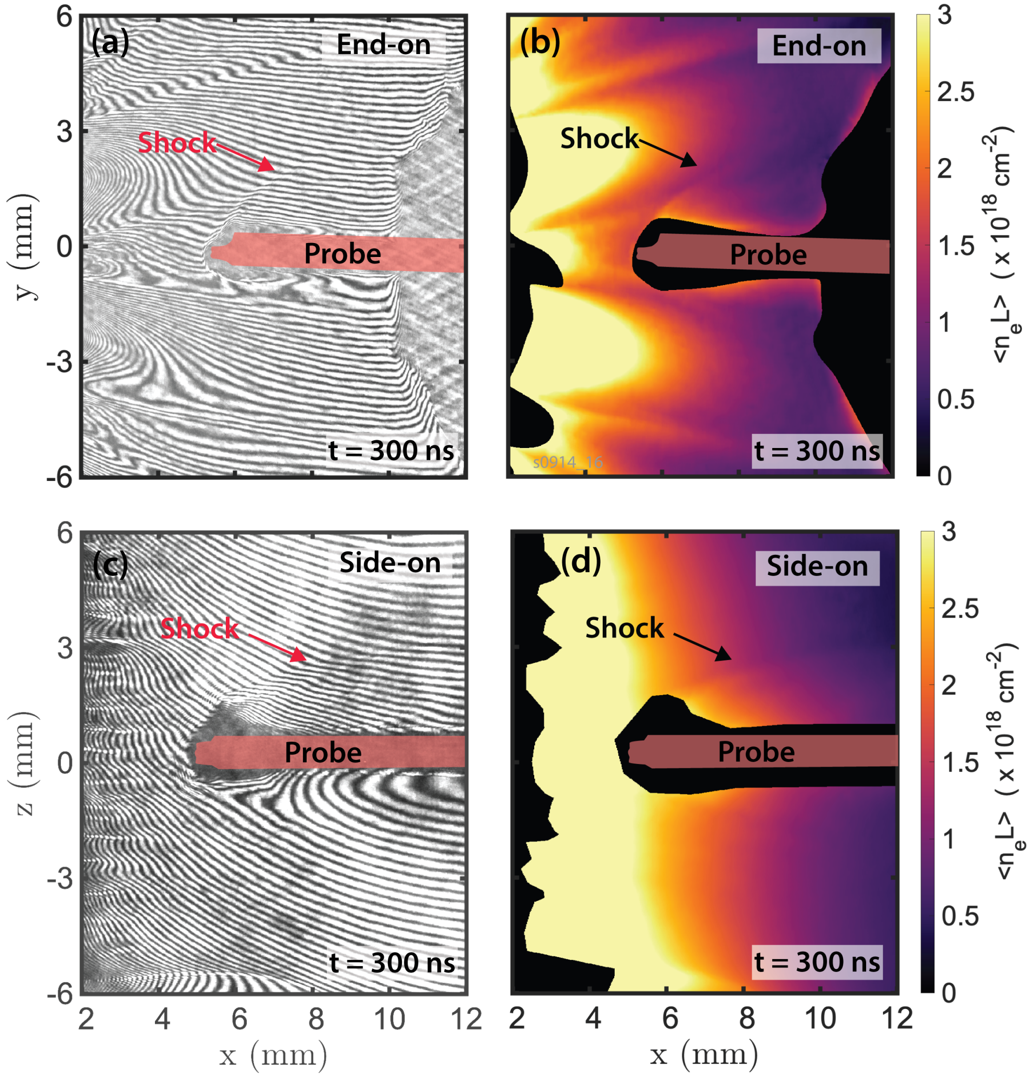

Figure 4-3: (a) End-on spatially heterodyned raw interferogram captured at 300 ns after current start using a Mach-Zehnder interferometry system with a 532 nm laser. The red shaded region is the shadow of the inductive probe, measured by blocking the reference beam and therefore backlighting the inductive probe using the probing laser beam. (b) End-on line-integrated electron density map determined using laser plasma interferometry. (c) Side-on raw interferogram captured at 300 ns after current start using a 1053 nm laser. (d) Side-on line-integrated electron density map determined using laser plasma interferometry. A detached bow shock is visible ahead of the probe in both side-on and end-on views. The shock opening half-angle is larger in the end-on view than in the side-on view. Note that regions in black near the obstacle and the wire array surface represent locations where the probing beam is lost.

the upstream flow in the end-on plane to also be modulated. In comparison, the upstream flow in the side-on plane is relatively more uniform.

We define the shock opening half-angle $\alpha/2$ as the angle between the obstacle axis and the shock front (See Figure 4-4). The opening half-angle decreases continuously with

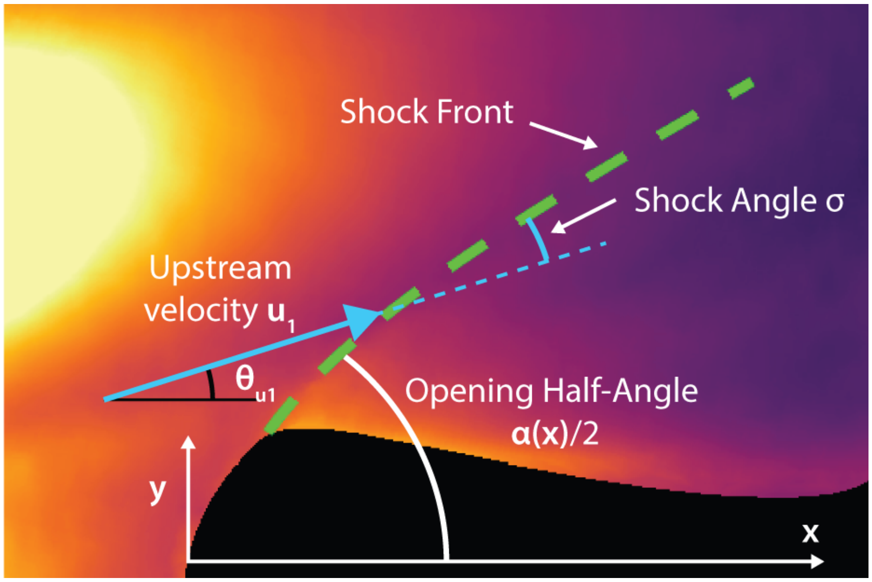

Figure 4-4: Schematic overlay showing bow shock geometry observed ahead of the inductive probe in the end-on view. The shock front is represented by the dashed green line. The opening half-angle is the angle between the obstacle axis and the shock front. The shock angle is the angle between the upstream velocity and the shock front.

distance from the nose of the obstacle. We observe the shock opening angle to be larger in the end-on plane than in the side-on plane.

The upstream velocity $\mathbf{u_1}$ makes an angle θ_{u1} with respect to the horizontal. We define the shock angle σ as the angle between the upstream velocity vector and the shock front (Figure 4-4). We can determine the shock angle from the opening half-angle and the velocity angle as $\sigma = \alpha/2 - \theta_{u1}$. To determine the opening-half angle from the observed bow shock geometry, we trace the shock front and fit a curve $s(x_s, y_s)$ to it. The opening half-angle then becomes $\alpha/2 = \tan^{-1}(dy_s/dx_s)$.

In the side-on view, the upstream velocity only has a component in the x-direction, i.e. $\theta_{u1} = 0$. So the opening half-angle and the shock angle are equal in the side-on view. In the end-on view, the velocity vector makes a non-zero angle with the horizontal. Therefore, we must account for the direction of the upstream velocity when calculating the shock angle. We assume that the upstream velocity propagates radially outwards with respect to the array center. The upstream velocity then makes an angle $\theta_{u1} = \tan^{-1}(y/x)$ to the horizontal.

In a bow shock, the shock angle varies continuously from 90° at the nose of the obstacle to the Mach angle μ asymptotically far away from the obstacle, where the bow shock constitutes an infinitesimally weak Mach wave. From our interferometry images (Figure 4-3), we observe that the shock opening half-angle approaches $\alpha/2 \rightarrow 30°$ and $\alpha/2 \rightarrow 7°$ in the end-on and side-on views respectively. The Mach angles are $\mu \approx 11 \pm 0.5°$ and $\mu \approx 7 \pm 0.5°$ in the end-on and side-on planes respectively. We discuss the discrepancy between the end-on and side-on Mach angles in §4.4.

If we assume that the linear wave phase velocity in the plasma is isotropic, we can use the simple relation $\sin\mu = 1/M_1$ to obtain the upstream Mach number. In the end-on plane, the observed Mach angle corresponds to an upstream Mach number of $M_S = 5.2 \pm 0.3$. In the side-on plane, the upstream Mach number is $M_S = 8.2 \pm 0.6$.

The assumption of an isotropic linear phase velocity requires further elaboration. If the shock is hydrodynamic, then the sound wave, which propagates isotropically at the ion sound speed C_s, sets the Mach angle. In a fast magnetohydrodynamic shock, the fast magnetosonic wave which determines the shock dynamics exhibits an anisotropic phase velocity — the fast wave propagates at the magnetosonic velocity $\sqrt{V_A^2 + C_S^2}$ perpendicular to the magnetic field, and at the higher of the sound speed and Alfvén speed V_A parallel to the magnetic field. Experimental results from pulsed-power aluminum plasmas in exploding wire arrays have shown that the magnetic pressure dominates, so that the Alfvén speed V_A exceeds the sound speed C_S. Secondly, similar experiments with 2D cylindrical obstacles show that the fast and Alfvén Mach numbers are expected to be roughly ~ 2 (while the sound Mach number $M_S > 5$) (Burdiak et al. [2017]; Suttle et al. [2019]). Thus, we can expect the anisotropy in the fast wave speed to be small.

4.3 Magnetic Field Measurements

Figure 4-5a shows the voltage signal from the inductive probes placed near the MITL and in the flow. The signal from the inductive probe near the MITL is proportional to the time rate of change of the current in the load. The current rate $\dot{I}$ in the load is initially positive for $0 < t < 250$ ns, then becomes negative for $t > 250$ ns, before returning back to 0 at $t \approx 400$ ns. The voltage signal at the load exhibits a characteristic ‘double-bumped’ structure with a larger peak at ~ 85 ns and a smaller peak at ~ 180 ns, caused by reflections from impedance mismatches within the transmission lines (Mitchell et al. [1996]). We observe that the rise time of the load current is ~ 250 ns.

The probe placed in the flow measures the time-rate of change of the post-shock magnetic field. The probe in the flow approximately reproduces the shape and characteristic features of signal at the MITL, including the characteristic 'double bump', showing that the magnetic field is frozen into the flow, and that the magnetic field from the inside of the array is advected to the outside by the ablating plasma. The black and blue circles in Figure 4-5a represent these features on the load and probe 1 signals respectively.

Figure 4-5b shows the normalized load current and the advected post-shock magnetic field. The normalized load current is determined by integrating the MITL inductive probe signal. The advected magnetic field is determined by integrating the voltage signals from the probe in the flow. The load current initially rises, reaches a maximum at ~ 250 ns, and then falls. The load current and the advected magnetic field have similar shapes, again confirming that the magnetic flux is frozen into the flow. We observe the post-shock peak magnetic field to be ~ 14 T. Due to a lack of calibration information we only show the shape of the current waveform rather than its magnitude. Other experiments show that MAGPIE consistently delivers a 1.4 MA peak current, which what we used in the later simulations of this experiment.

Figure 4-5c shows the velocity of the plasma at the inductive probe determined from the ratio of the distance from the array to the probe and the time of flight of the plasma to the probe. The time of flight is determined from the time interval between the corresponding features on the load and the probe signals respectively, as shown in Figure 4-5(a). The distance to the probe (L = 5.55 ± 0.25 mm) is determined from the interferometry images. The velocity at the probe is ~ 100 km s^{-1} early in time and decreases to ~ 60 km s^{-1} at $t \approx 350$ ns. We can compare flow velocity with the flow speed determined in similar exploding arrays using Thompson scattering. Burdiak et al. [2017] report a flow velocity of ≈ 75 km s^{-1} at $t \approx 250$ ns from Thompson scattering measurements at a position ~ 6 mm from the array. This is consistent with the calculated flow velocity of 71 ± 12 km s^{-1} from our inductive probe measurements.

At 300 ns, the velocity at the probe is $V = 62 \pm 12$ km s^{-1}. From the interferometry images, we know that the expected upstream Mach numbers are 5.2 ± 0.3 and 8.2 ± 0.6 in the end-on and side-on planes respectively. If we assume that the shock is hydrodynamic, then we can determine the sound speed C_S and the electron temperature ZT_e of the plasma. The sound speed is $C_S = 11.8 \pm 2.4$ km s^{-1} in the end-on plane, and $C_S = 7.6 \pm 1.6$ km s^{-1} in the side-on plane. This corresponds to $ZT_e = 35 \pm 14$ eV and $ZT_e = 14 \pm 6$ eV in the end-on and side-on planes respectively. For comparison, the value of ZT_e determined using Thomson scattering in a similar pulsed-power driven aluminum plasma is ~ 42 eV (Burdiak et al. [2017]). Assuming an average ionization of 3.5 for the aluminum plasma, the expected electron temperature is $T_e \approx 10$ eV (end-on) and $T_e \approx 4$ eV (side-on).

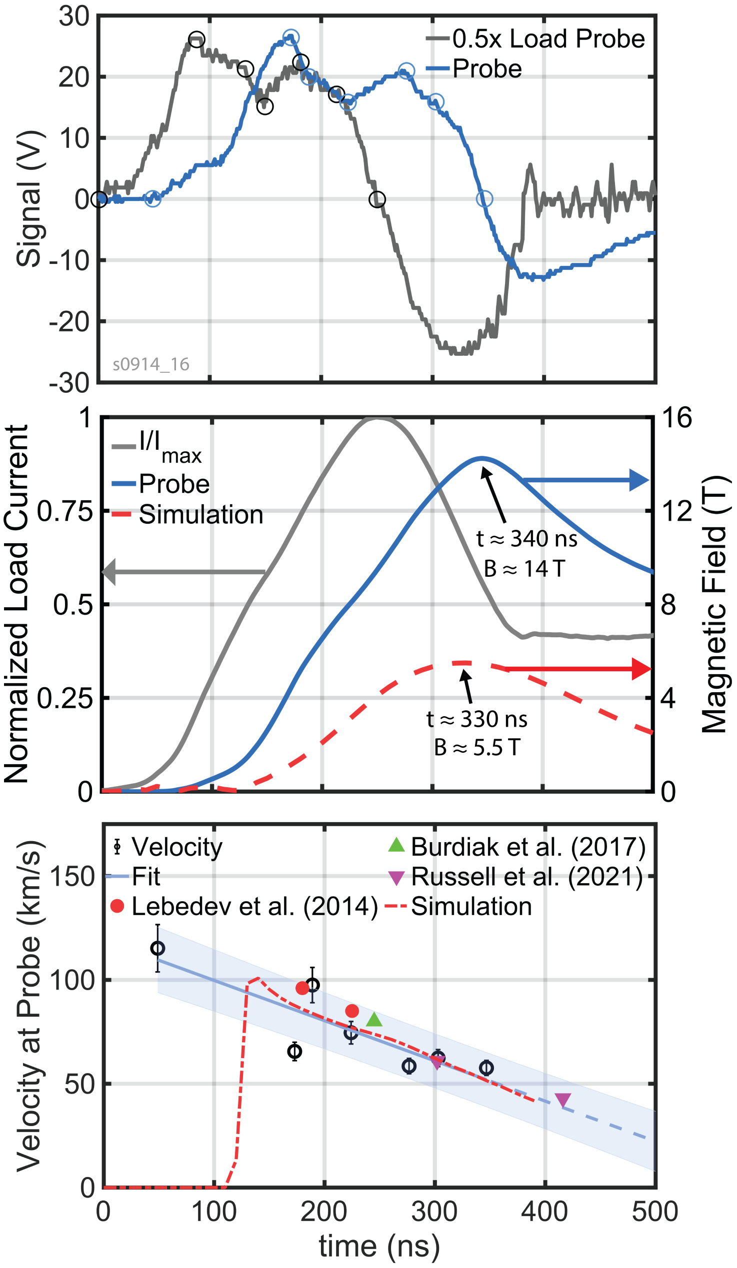

Figure 4-5: Load current and magnetic field measurements from inductive probes. (a) Voltage signal from inductive probes. The grey line represents the signal from the probe located near the magnetically insulated transmission line (MITL). The black line represents the voltage signal from the inductive probe placed in the flow. (b) Normalized load current and the advected post-shock magnetic field. The advected magnetic field is determined from integration of the voltage signal from the probe. (c) Velocity of the plasma at the probe determined from the time of flight of the plasma to the position of the probe. The time of flight is determined from the time interval between the corresponding features on the load and the probe signals respectively, as shown in (a). The blue solid curve is a linear fit through the velocity measurements, and the blue shaded region is the ±1 standard deviation bounds of the fit.

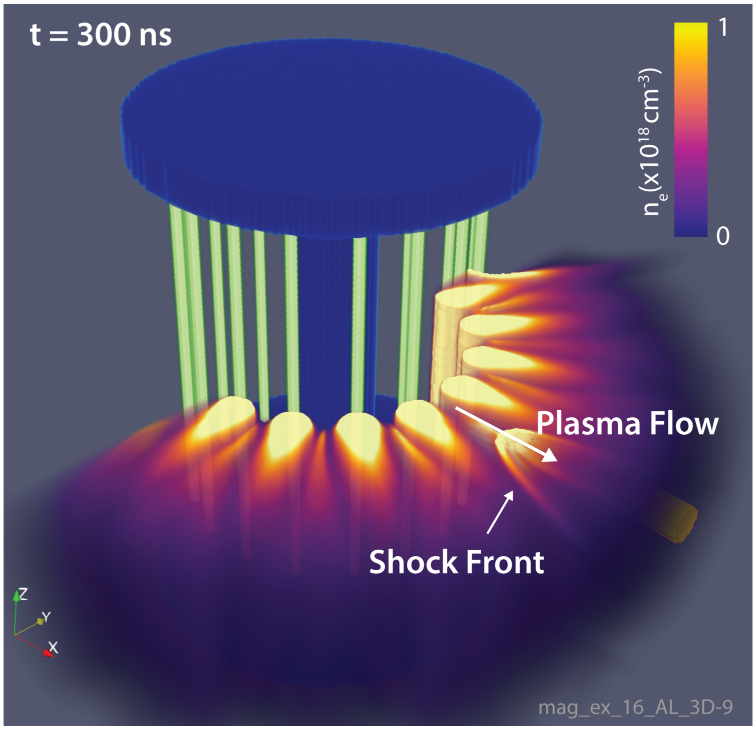

Figure 4-6: GORGON resistive MHD simulation with an electron density slice of the ablating plasma at 300 ns. A detached bow shock is seen ahead of the obstacle. Note that the left half of the electron density slice is clipped for clarity.

4.4 Comparison with Simulation

We perform full 3D simulations of a 16 mm diameter 16 mm tall exploding wire array with 16 equally-spaced 30 µ aluminum wires. A sine-squared current profile (I_{pk} = 1.4 MA, t_{rise} = 240 ns) was applied to the load. The simulation domain is a cuboid with dimensions 60 × 60 × 45 m^3, and a resolution of ≈180 µm. The wire core diameter is set to ≈540 µm. We place a perfectly resistive cylindrical obstacle of radius ∼ 1 mm at 5.5 mm from the array surface. The cylindrical obstacle mimics the inductive B-dot probes in the experiment, and is aligned parallel to the x-axis. The leading edge of the cylinder is a non-conducting sphere of radius ∼ 1 mm, such that the leading edge is located at $x \approx 12.6$ mm. The obstacle is positioned such that the oblique shock centerline is parallel to the obstacle axis. The simulation geometry, together with a slice of the simulated electron density at 300 ns, are shown in Figure 4-6.

Figure 4-7a and Figure 4-8a show the end-on and side-on slices of the simulated electron density through the obstacle mid-plane at 300 ns. Figure 4-7b and 4-8b show the end-on and side-on line-integrated electron density at 300 ns. A detached bow shock is visible ahead of the obstacle in both the electron density slices and the line-integrated maps. In the line-integrated electron density maps, the shock front appears "muted", similar to what we observe in the experimental image. This is because line-integrating obfuscates the intensity of the 3D shock front.

The simulated upstream flow is qualitatively similar to the experimentally observed flow. The electron density is higher closer to the array surface and decreases with distance from the array in both the simulation and experiment. In the end-on plane, the upstream flow in both the simulated and experimentally observed electron density maps are modulated in the azimuthal direction due to the formation of oblique shocks between adjacent plasma jets, while in the side-on plane, the upstream flow is relatively more uniform. The opening half-angle in the end-on plane is larger than in the side-on plane, similar to what is observed in the experiment. Far from the obstacle, the opening half-angle in the side-on plane approaches $\approx 7^o$ in both the simulation and experiment. In the end-on plane, however, the opening half-angle in the end-on plane approaches $\approx 21^o$ in the simulation, and $\approx 30^o$ in the experiment.

We determine the shock angle in the simulation by subtracting the angle the upstream velocity makes with the horizontal from the opening half-angle. The Mach angles from the simulation are $\mu \approx 8°$ in the end-on plane, and $\mu \approx 7°$ in the side-on plane. This corresponds to an upstream Mach number of $7.2 < M_1 < 8.2$.

We can compare these values of the upstream Mach number obtained from shock geometry with those obtained from the fluid properties. We calculate the sonic Mach number $M_S = u_1/C_S$. Here, $C_S = \sqrt{\gamma Z T_e/m_i}$ is the ion sound speed, Z is the ionization of the plasma, T_e is the electron temperature, and m_i is the ion mass. The polytropic index γ typically differs from the ideal fluid value of $5/3$ for a plasma, and is a function of the ion density n_i and electron temperature T_e. The polytropic index of the simulated plasma remains relatively constant at $\gamma \approx 1.13$ throughout the plasma. The upstream flow is supersonic. In the end-on plane, the sound Mach number is modulated between the oblique shocks and the jets, and varies between $4.8 < M_S < 8.2$ upstream of the shock. In the side-on plane, the upstream Mach increases with distance form the array, and varies between $4.8 < M_S < 6.9$ upstream of the shock. This range of Mach numbers is in good agreement with the range of Mach numbers expected from the geometry of the simulated shock ($7.2 < M_1 < 8.2$).

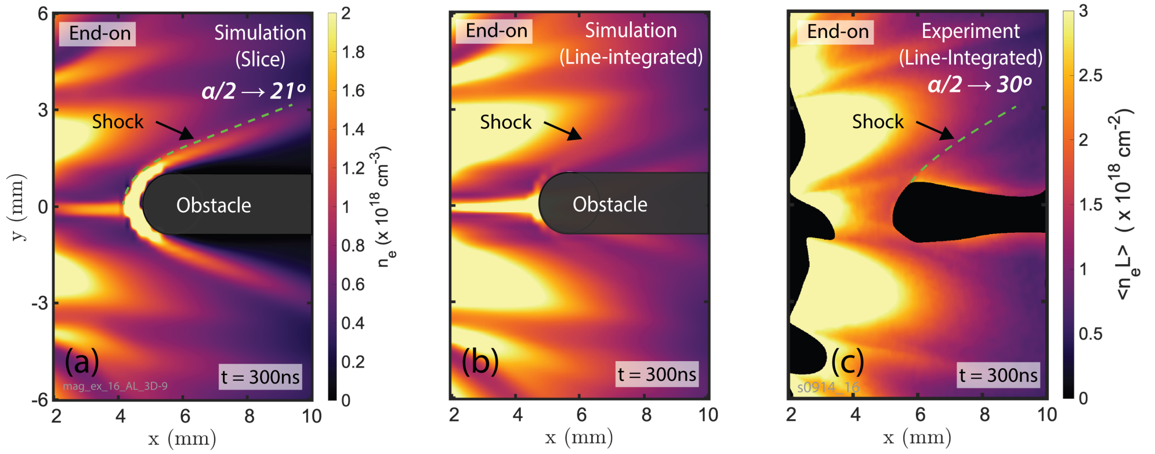

Figure 4-7: (a) End-on slice of electron density at 300 ns from 3D resistive MHD GORGON simulation of the experimental geometry. (b) End-on line-integrated electron density at 300 ns from 3D resistive MHD GORGON simulation of the experimental geometry. (c) Experimental end-on line-integrated electron density at 300 ns from plasma interferometry (reproduced here from Figure 4-3). In each image, the plasma flow is from the left to the right, and the magnetic field lies in the plane of the page. A bow shock, characterized by a discontinuous increase in electron density, is visible ahead of the obstacle. Far from the obstacle, the opening half-angle in the end-on plane approaches ≈ 21^o in the simulation, and ≈ 30^o in the experiment.

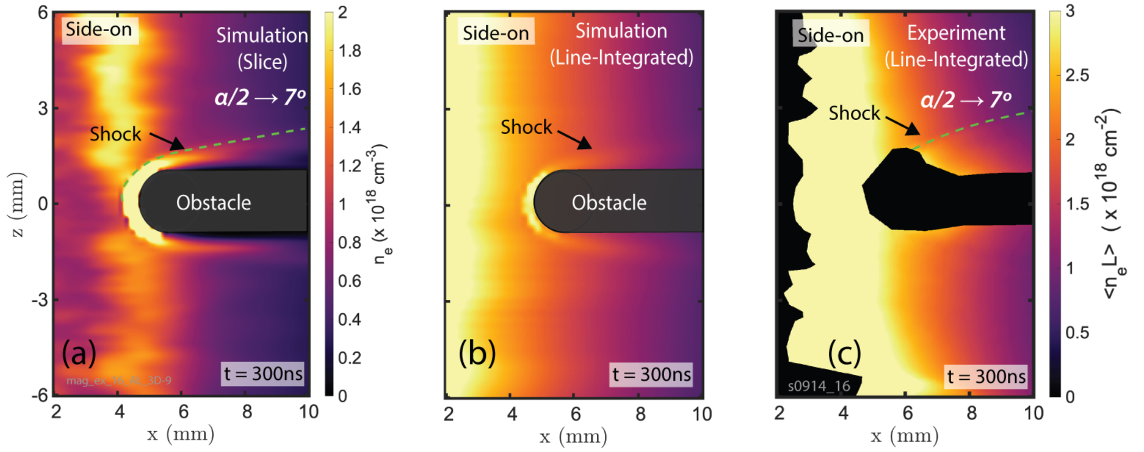

Figure 4-8: (a) Side-on slice of electron density at 300 ns from 3D resistive MHD GORGON simulation of the experimental geometry. (b) Side-on line-integrated electron density at 300 ns from 3D resistive MHD GORGON simulation of the experimental geometry. (c) Experimental side-on line-integrated electron density at 300 ns from plasma interferometry (reproduced here from Figure 4-3). In each image, the plasma flow is from the left to the right, and the magnetic field points into the page. A bow shock, characterized by a discontinuous increase in electron density, is visible ahead of the obstacle. Far from the obstacle, the opening half-angle in the side-on plane approaches ≈ 7^o in both the simulation and experiment.

We also compute the fast Mach number $M_f = u_1/V_f$ of the flow. Note that the fast magnetosonic speed is assumed to be $V_f = \sqrt{C_S^2 + V_A^2}$. The plasma beta of the simulated

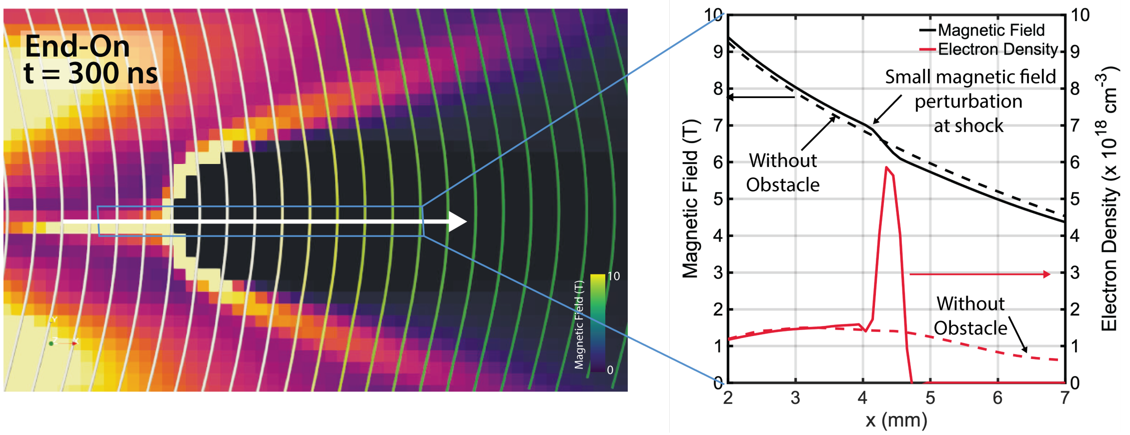

Figure 4-9: (a) Magnetic field lines overlaid on the electron density map generated in GORGON at 300 ns after current start. The magnetic field lines point in the azimuthal direction, and remain mostly unaffected by the shock front, confirming the hydrodynamic nature of the shock. (b) Line-outs of the magnetic field and electron density along the obstacle-axis. The magnetic field exhibits a negligible perturbation at the shock front.

plasma is $\beta \sim 0.1$, so the upstream fast phase velocity is roughly isotropic and the Mach number is approximately equal to the Alfvén Mach number. In the end-on and side-on views, the upstream flow is sub-fast just upstream of the obstacle, and the fast Mach number upstream of the shock increases to 1.1-1.9 away from the obstacle.

The upstream Mach number predicted from shock geometry is in better agreement with the calculated upstream sonic Mach number M_S than with the fast Mach number M_f. This suggests that the simulated shock is hydrodynamic in nature, and that the magnetic field is able to diffuse resistively through the obstacle rather than be compressed ahead of it. We plot the magnetic field lines overlaid onto the simulated electron density map in Figure 4-9a. The magnetic field lines point in the azimuthal direction, and remain mostly unaffected by the shock front, confirming the hydrodynamic nature of the shock. 4-9b shows line-outs of the magnetic field and electron density along the obstacle axis. The magnetic field exhibits a negligible perturbation at the shock front. This can happen if the resistive diffusion length scale is large, such that the magnetic field decouples from the fluid, and diffuses through the obstacle, instead of piling-up, or being compressed by the shock. The calculated resistive diffusion length from the simulation is $L_v \sim 1$ mm. Furthermore, numerical resistivity, introduced due to a finite grid size, can also increase the resistive diffusion length scale.

Finally, we plot the simulated magnetic field at the probe as a function of time, and compare it with the experimentally obtained magnetic field strength in Figure 4-5. The shape

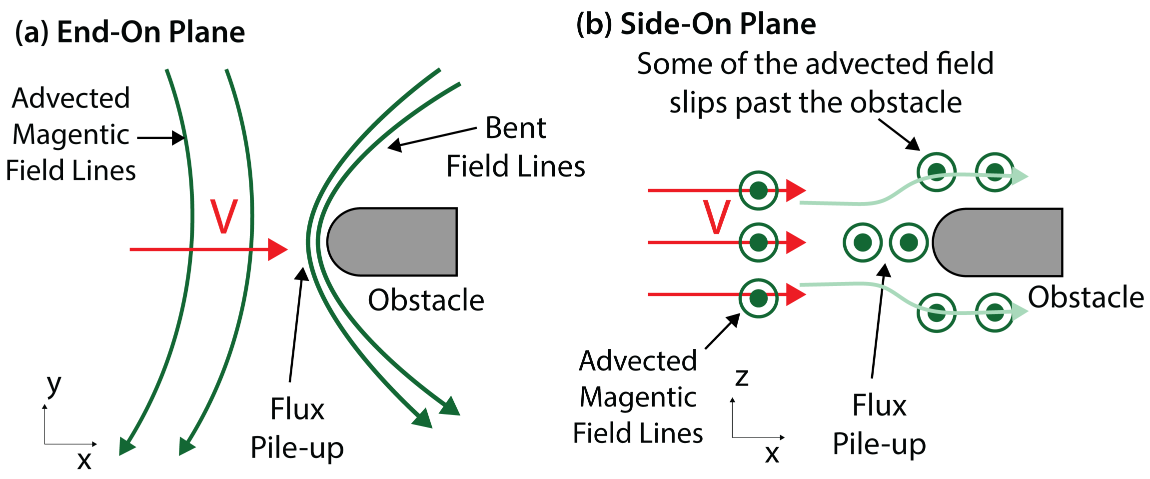

Figure 4-10: (a) Pile-up of magnetic flux ahead of the 3D obstacle in the end-on plane. The field lines drape around the obstacle, and the magnetic tension of the bent field lines opposes the upstream ram pressure. (b) Pile-up and slipping of magnetic field lines ahead of a 3D obstacle in the side-on plane. Some of the field lines will pile-up ahead of the obstacle, and some will slip past the obstacle. If the obstacle is resistive, magnetic field may also resistively diffuse through it. The accumulation of the magnetic field will depend on the competition between the rates of pile-up, diffusion and slipping

of the simulated magnetic field measurement is similar to that of the experimentally observed field. However, the peak simulated field at the probe (~ 5.5 T) is weaker than the experimentally observed peak field (~ 14 T). This suggests that the simulation may not completely capture the dynamics of shock formation in the plasma. The higher post-shock magnetic field observed in the experiment may be due to magnetic field pile-up ahead of the obstacle. This may also explain the higher Mach angle ($\sim 11°$) observed in the end-on plane compared to the side-on plane ($\sim 7°$). When magnetic field lines frozen into the flow approach a resistive obstacle, they may pile-up ahead of the obstacle, slip past it or diffuse through the obstacle. If the rate of slipping and diffusion in small, then the magnetic field will drape around the obstacle. When the field lines pile-up and bend ahead of the obstacle, as shown in Figure 4-10a, the magnetic tension of the bent field lines provides an additional force opposing the ram pressure of the incoming upstream flow, which results in a larger opening angle and stand-off distance of the shock (Burdiak et al. [2017]). The end-on plane represents the plane parallel to the field lines, and this bending and larger opening angle should increase the end-on opening angle. However, in the side-on plane, the magnetic field lines are normal to the plane, so even when the magnetic field lines pile up, the bending of field lines does not affect the side-on shock angle, although we will still see a larger stand-off distance. This is shown in Figure 4-10b. Moreover, the field lines can also slip past the obstacle, as shown in Figure 4-10b, and also diffuse through the obstacle (and the thin layer of hot conductive plasma on the obstacle surface), so the accumulation of the magnetic field will depend on the competition between the rates of pile-up, diffusion and slipping. More experiments and simulations are required to investigate magnetic field pile-up ahead of the inductive probe.

4.5 Future Work

We propose 2 additional diagnostics to better characterize the shock dynamics in future experiments. These are (1) Shadowgraphy/Schlieren Imaging (2) Optical Thompson Scattering.

4.5.1 Shadowgraphy and Schlieren Imaging

Shadowgraphy and Schlieren imaging are imaging techniques that depend on the refraction of light through the plasma. Electron density gradients cause deflection of light rays in a plasma. Light rays are deflected away from high-density regions and towards low-density regions. The magnitude of the deflection depends on the spatial derivative of electron density.

In Shadowgraphy, light that passes through the plasma is simply captured on a detector. High-density regions appear darker than low-density regions in the image. In Schlieren imaging, light that has traveled through the plasma is focused using a converging lens. A stop (or 'knife-edge') is placed at the focal point. This blocks any undeflected rays and only allows deflected rays to pass through and impinge on the detector. This technique is called dark-field Schlieren. The stop can also be displaced by some distance from the focal position. This allows the undeflected rays to pass through and blocks the deflected rays — a technique called bright-field Schlieren.

The intensity of the resulting image is proportional to the spatial derivatives of the electron density in Schlieren and Shadowgraphy imaging. Since bow shocks generate strong density gradients, these techniques can be used to produce high-resolution images of the shock.

4.5.2 Optical Thompson Scattering

We can determine the sound Mach number and direction of the upstream flow using Optical Thompson Scattering (OTS). In OTS, we illuminate a small volume of the plasma

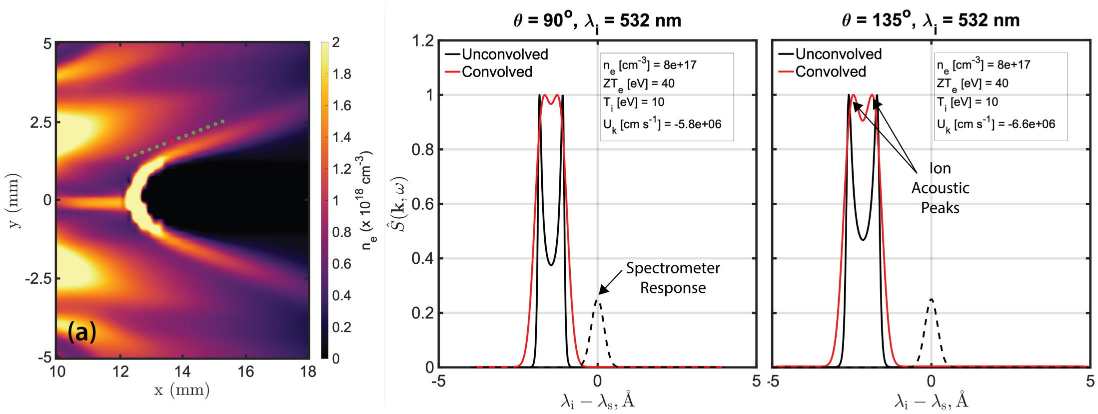

Figure 4-11: Synthetic optical Thompson scattering spectra generated using simulated properties. (a) Position of the TS collection volumes overlaid onto the simulated electron density slice at 300 ns. (b) Synthetic TS spectral density function at $\theta = 90°$ scattering angle. (c) Synthetic TS spectral density function at $\theta = 135°$ scattering angle. The sythetic spectra show well-defined ion acoustic peaks. We can determine the electron and ion temperatures from the peak separation and peak width respectively, and the velocity along the scattering vector from the Doppler shift of the response. Note that the red solid line represents the spectral density function (black solid line) convolved with the spectrometer response (black dashed line). The spectrometer response is assumed to be a $\sigma = 0.2$Å gaussian function.

.

with a laser beam. The incident light is scatted by the plasma in all directions. We collect the scattered radiation at some angle θ to the incident light. The spectrum of the scattered light can give us information about the density, temperature, ionization, and velocity of the plasma. OTS is discussed in more detail in Chapter 3.

The spectral density of the scattered radiation has contributions from both the ion and electron fluids. The scattered radiation also exhibits resonances at the electron plasma wave and ion acoustic wave frequencies. These appear as peaks in the spectral density function. Peaks are typically damped by Landau damping and collisions.

The ion acoustic feature is of particular interest in our application. The ion acoustic peaks are low-frequency features which appear at:

$$\omega_{ac} \simeq \pm k \left(\frac{k^2 \lambda_D^2}{\left(1 + k^2 \lambda_D^2\right)} \left(\frac{Z T_e}{m_i} \right) + \frac{3 T_i}{m_\mathrm{i}} \right)^{1/2} \tag{4.2}$$

Here, k is the wavenumber, λ_D is the Debye length, Z is the ionization, T_e is the electron temperature, T_i is the ion temperature, and m_i is the ion mass.

Ion acoustic peaks are only visible in the spectral density function when $ZT_e/T_1 > 3$. For smaller values of ZT_e/T_1 the peaks are strongly damped. The wavelength separation of the peaks $\Delta\lambda \sim \lambda_i\sqrt{ZT_e/m_i}$ gives us information about the electron temperature. The width of the peak, which depends on the amount of Landau damping, increases with increasing values of ZT_e/T_i. Finally, we determine the velocity along the scattering vector from the Doppler shift of the scattered radiation. By collecting the scattered radiation along two non-parallel scattering vectors, we can determine the direction and magnitude of the upstream in-plane velocity.

Synthetic TS spectra at two different scattering angles $\theta = 90°$ and $\theta = 135°$ are shown in Figure 4-11. The spectra are generated using the plasma parameters in the GORGON simulation at 300 ns. Note that the Thomas-Fermi LTE ionization model used in GORGON typically under-predicts the electron and ion temperatures. Here, we have used more realistic values of electron and ion temperatures ($ZT_e \sim 40$ eV, $T_i \sim 10$ eV) for the simulated spectra. The synthetic spectra show well-defined ion acoustic peaks, and the response is Doppler shifted from the origin. This will allow us to determine the velocity, electron, and ion temperatures in the experiment, and allow us to compare the velocity and temperature determined from the inductive probes.

4.6 Summary

In this chapter, we have presented experimental results and discussion of bow shocks generated in a supersonic magnetized plasma due to collision with inductive probes. The plasma was generated using a pulsed-power driven exploding wire array with 16 equally-separated aluminum wires. An inductive probe was used to measure the post-shock magnetic field in the flow, and laser interferometry was used to image the bow shock and the flow around the probe.

Interferometry images taken at 300 ns after current start show a well-defined detached bow shock ahead of the probe. The bow shock has a 3D structure, with a larger opening angle in the end-on plane than in the side-on plane. Part of this effect is due to the radially diverging nature of the upstream flow. Assuming that the upstream flow points radially outwards from the array center, we subtract the angle of the velocity vector relative to the horizontal from the shock opening half-angle to determine the shock angle. Far from the obstacle, the shock angle asymptotically approaches the Mach angle. From the shock geometry, the Mach angle is 11°±0.5° in the end-on plane, and 7°±0.5° in the side-on plane. These correspond to upstream Mach numbers of 5.2±0.3 (end-on) and 8.2±0.6 (side-on).

Inductive probe measurements show good agreement between the shape of the signal at the load and in the flow. The probe signal reproduces the characteristic "double-bump" that appears in the load signal at a later time, showing that the magnetic field is frozen into the flow. We integrate the probe signal in time to determine the magnetic field strength. The peak magnetic field strength is 14 T and occurs at ~ 345 ns after current start.

We use the time-of-flight of the plasma to the probe to estimate the flow velocity. The flow velocity at the probe is ~ 100 km s^{-1} early in time and decreases to ~ 60 km s^{-1} later in time. The calculated flow velocity is consistent with the flow velocity of reported in literature for pulsed-power driven aluminum plasmas. We use the velocity and the shock geometry to estimate the sound speed, and therefore ZT_e in the flow. The estimated value of ZT_e is 35 ± 14 eV and 14 ± 6 for end-on and side-on values of the Mach number respectively, and includes the value of 42 eV determined using Thompson scattering for a similar plasma.

We compare our results with full 3D resistive MHD simulation in GORGON. The simulation successfully reproduces several features of the experiment. The simulated bow shock has a larger opening angle in the end-on plane than in the side-on plane. We calculate the shock angle by subtracting the velocity angle from the opening half-angle. The Mach angle is side-on plane is 7°, which is in good agreement with the experimentally observed value. The Mach angle is end-on plane is 8°, which is ≈ 3 ° lower than the experimental value. This may be because the simulation may not be accurately capturing the magnetic field- pile-up ahead of the obstacle.

We calculate the sonic Mach number from the simulated plasma parameters, and find that it is in good agreement with the range of upstream Mach numbers expected from the shock geometry. Therefore, the simulation predicts a hydrodynamic shock. Visualization of the simulated magnetic field shows that the magnetic field is mostly unperturbed by the shock front. This may be a result of a very large resistive diffusion length scale, which allows the magnetic field to diffuse through the obstacle and not participate in the shock.

The results presented here provide insight into the physics of 3D magnetized bow shocks, which are of relevance to many astrophysical plasma flows. Furthermore, we use a new diagnostic technique to estimate both the time-resolved velocity and temperature of the plasma, by simultaneously measuring the time of flight of the plasma to the inductive probe, and the geometry of the bow shock.

Chapter 5

Oblique Shocks in Inverse Z-Pinch Wire Arrays

In this chapter, we discuss oblique shocks in a highly collisional magnetized plasma, generated during the ablation phase of the exploding wire array described in Chapter 4 [1]. Standing hydrodynamic-like oblique shocks form when adjacent jets of plasma diverging from the wire cores collide in the azimuthal direction. We use laser interferometry to visualize the oblique shocks and to obtain the line-integrated electron density. Oblique shocks appear as regions of high-density post-shock plasma bounded on either side by oblique shock fronts. The oblique shocks also exhibit a hollow density profile — the electron density is high near the shock fronts, and low near the shock center-line. Treating the shock as a hydrodynamic-like oblique shock, we estimate the upstream sonic Mach number from the observed shock geometry, and compare the experimental results with 2D resistive MHD simulations performed using GORGON.

5.1 Experimental and Diagnostic Setup

The experimental setup is described in Chapter 4. The load is a cylindrical exploding wire array with 16 equally-spaced 30 µm diameter aluminum wires, driven by the MAGPIE generator (1.4 MA, 250 ns). We use an end-on Mach-Zehnder laser interferometry system (532 nm Nd:YAG) to visualize the oblique shocks.

---

[1] The experimental data reported here were collected by personnel at the MAGPIE facility, Imperial College London, in 2016. The author is responsible for the analysis and interpretation of the collected data.

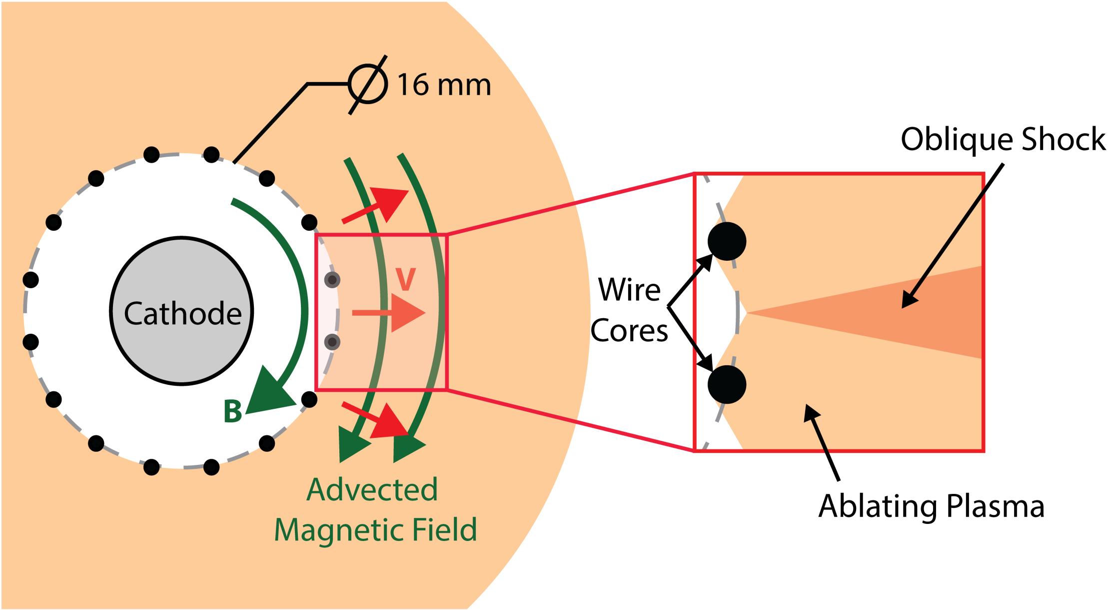

Figure 5-1: End-on (xy-plane) view of the experimental geometry, showing a cylindrical array of 16 equally-spaced 30 μm Al wires around a central cathode. The array diameter is 16 mm and the array height is 16 mm. Collision of the azimuthally expanding plasma from the wire cores results in the formation of oblique shocks between the ablating plasma jets.

5.2 Oblique Shock Morphology

Figure 5-2 shows the line-integrated end-on electron density map obtained from laser interferometry at 300 ns after current start. Oblique shocks form between plasma jets ablating from the wire cores, and appear as dense regions of post-shock plasma bounded by oblique shock fronts. The shocks exhibit a hollow density profile — the electron density is lower at the shock center-line and higher at the oblique shock fronts. The oblique shocks form due to the supersonic collision of adjacent azimuthally-expanding plasma jets. The coronal plasma accelerates radially outwards from the array center under the action of both the $\mathbf{j} \times \mathbf{B}$ and the pressure gradient ∇p force. The $\mathbf{j} \times \mathbf{B}$ force only acts in the radial direction, and does not accelerate the plasma in the azimuthal direction. The plasma expands in the azimuthal direction due to its thermal pressure. Adjacent jets collide supersonically and form oblique shock, as observed in Figure 5-2a. We take lineouts of the line-integrated electron density along the azimuthal direction at radial locations R = 12 mm, 12.5 mm, and 13.0 mm. The electron density is ~2x higher along the center of the ablating jets than in the oblique shocks. The electron density rises sharply at the oblique shock fronts. The post-shock electron density is mostly uniform close to the array ($R \leq\sim 12$ mm), but the density profile becomes hollower away from the array at $R \geq\sim 12.5$ mm.

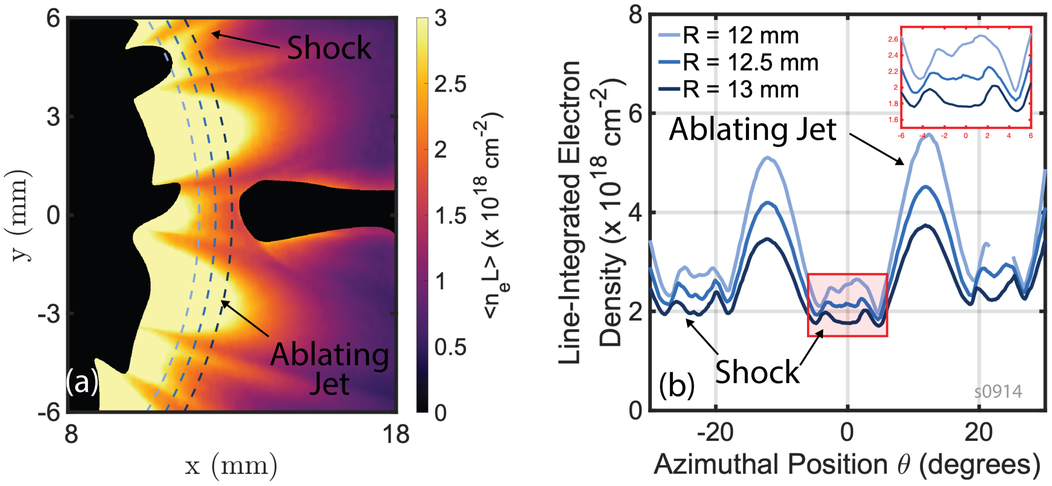

Figure 5-2: (a) End-on line-integrated electron density map obtained from laser interferometry. Oblique shocks form between the ablating plasma jets from the wire cores, and appear as dense regions of post-shock plasma bounded by oblique shock fronts. The oblique shocks exhibit a hollow density profile with high density near the shock fronts and low density near the shock center-line. We use a coordinate system centered on the array axis. (b) Lineouts of the line-integrated electron density along the azimuthal direction at radial distances of R = 12 mm, 12.5 mm and 13 mm from the array center (dashed blue lines in (a)). The electron density rises sharply at the oblique shock fronts. Close to the array (R = 12 mm), the post-shock electron density is mostly uniform, but the density profile becomes hollow at $R \geq 12.5$ mm.

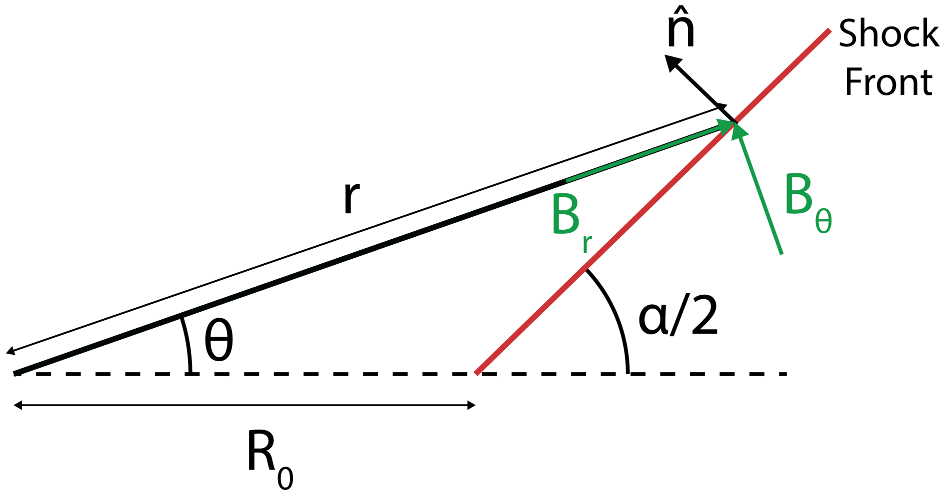

Figure 5-3: Schematic of the oblique shock geometry with the radial and azimuthal components of the upstream magnetic field. In the limit of small $\alpha/2 - \theta$ and $B_r/B_\theta \ll 1$, the upstream magnetic filed is approximately parallel to the shock normal, and the shock becomes a hydrodynamic-like oblique shock.

Let us examine whether we expect the shock to be hydrodynamic (magnetic field is not compressed) or magnetohydrodynamic (magnetic field is compressed). Consider an oblique shock front which forms at an angle $\alpha/2$ from the horizontal at a radial position R_0 from the array center, as illustrated in Figure 5-3. In the exploding array, the oblique shocks form close to the array surface, so R_0 is approximately the radius of the exploding wire array. We call the angle between the two oblique shock fronts α the opening angle of the shock. At an arbitrary radial length r, the shock front is located at an azimuthal position θ. From the geometry, we can relate the shock opening half-angle $\alpha/2$ and the azimuthal position θ of the shock at some r using:

$$\tan(\alpha/2) = \frac{r\cos\theta\tan\theta}{r\cos\theta - R_0} \tag{5.1}$$

Let the shock normal and shock tangent be represented by the unit normal vectors $\hat{\mathbf{n}}$ and $\hat{\mathbf{t}}$ respectively. Then the tangential and normal components of the magnetic field at the shock front are:

$$\begin{aligned} \mathbf{B_t} &= [B_r\cos(\alpha/2-\theta) - B_\theta\sin(\alpha/2-\theta)]\,\hat{\mathbf{t}} \\ \mathbf{B_n} &= [(B_r\sin(\alpha/2-\theta) + B_\theta\cos(\alpha/2-\theta)]\,\hat{\mathbf{n}} \end{aligned} \tag{5.2}$$

Here, B_r and B_θ are the radial and azimuthal components of the upstream magnetic field. In the small angle limit $\alpha/2-\theta \equiv \zeta << 1$, the expressions reduce to:

$$\begin{aligned} B_t &\approx B_r - B_\theta\zeta \\ B_n &\approx B_r\zeta + B_\theta \approx B_\theta \end{aligned} \tag{5.3}$$

We see that the magnetic field normal to the shock front reduces to the azimuthal field. Across a shock front, the normal magnetic field remains continuous, i.e. $[\![B_n]\!] = 0$, so we expect the azimuthal magnetic field to be continuous across the shock front. The radial field B_r contributes to the tangential field, which obeys $[\![\hat{\mathbf{n}}\times(\mathbf{u}\times\mathbf{B})]\!] = \mathbf{0}$, and can be discontinuous across the shock front. Finally, in the limit of small radial magnetic field $B_r/B_\theta \ll 0$, such as in a cylindrical wire array, the tangential magnetic field becomes small compared to the normal magnetic field $B_t/B_n \sim B_r/B_\theta - \zeta \ll 1$. We can approximate the shock as a parallel shock ($B_t \to 0$), and the MHD shock reduces to a hydrodynamic oblique shock. Therefore, we expect the oblique shocks to be hydrodynamic-like in the exploding wire array.

In a hydrodynamic oblique shock, the upstream velocity $\mathbf{u_1}$, which forms an angle θ_{u1} with the horizontal, is deflected by an angle ϕ across the shock front, as illustrated in Figure 5-4a. The angle at which the shock front forms relative to the upstream velocity is called the shock angle σ. Across the shock front, the tangential velocity remains continuous, while the normal velocity decreases abruptly. In Figure 5-4a, the shock front

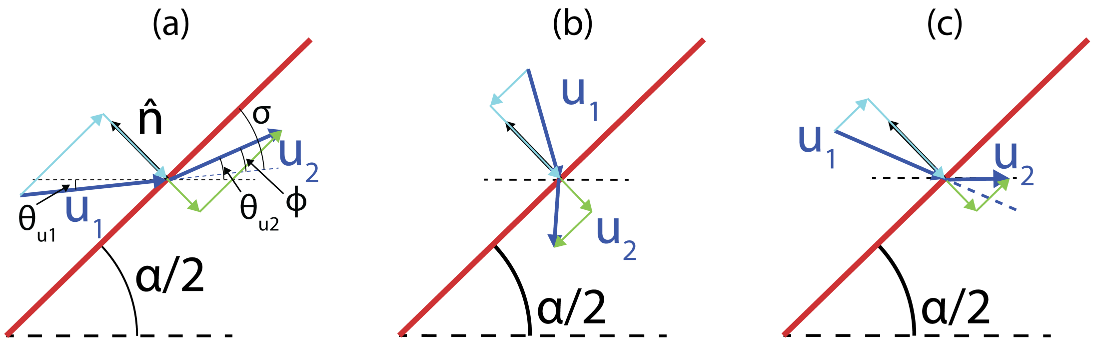

Figure 5-4: (a) The upstream velocity makes an angle θ_{u1} with the horizontal, and is deflected by an angle ϕ across the shock front. The tangential velocity remains continuous across the shock front while the normal velocity decreases abruptly, which causes the velocity vector to deflected counter-clockwise away from the horizontal. The shock front forms at an angle σ to the upstream velocity. (b) The upstream velocity makes a negative angle to the horizontal and the magnitude of this angle is $|\theta_{u1}| > \pi/2 - \alpha/2$. In this case, the tangential velocity is in the negative direction, and the velocity vector is deflected clockwise away from the horizontal. (c) The upstream velocity makes a negative angle to the horizontal and the magnitude of this angle is $|\theta_{u1}| \leq \pi/2 - \alpha/2$. In this case, the tangential velocity is in the positive direction, and the velocity vector is deflected counter-clockwise towards the horizontal.

deflects the velocity vector counter-clockwise away from the horizontal. We can show that the shock geometry satisfies the following relations:

$$\begin{aligned} \theta_{u1} &= \theta_{u2} - \phi \\ \sigma &= \alpha/2 - \theta_{u1} \\ \text{Where} \qquad \theta_{u1,2} &= \tan^{-1}\left(\frac{u_y}{u_x}\right)_{1,2} \end{aligned} \tag{5.4}$$

The deflection and shock angles can be related using the upstream sonic Mach number $M_1 = u_1/C_S$ and the polytropic index γ (ratio of specific heats) of the plasma (Kundu et al. [2012]):

$$\tan\phi = 2\cot\sigma \frac{M_1^2 \sin^2\sigma - 1}{M_1^2(\gamma + \cos 2\sigma) + 2} \tag{5.5}$$

Thus, for a plasma of polytropic index γ, if we know the shock and deflection angles, we can estimate the upstream Mach number from the shock geometry. From Equation(s) 5.4, we see that the shock angle σ and the deflection angle ϕ depend on the opening half-angle $\alpha/2$, and the upstream and downstream velocity angles $\theta_{u1,2}$. We can measure the opening half-angle $\alpha/2 = 10° \pm 1.4°$ directly from the shock geometry shown in Figure 5-2.

We do not know the values of the velocity angles $\theta_{u1,2}$. However, we can still estimate the upstream Mach number if we make some simplifying assumptions. Due to the symmetry of the system, we assume that the post-shock velocity is parallel to the shock center-line, i.e. $\theta_{u2} = 0$. If the upstream velocity makes an positive angle $\theta_{u1} > 0$ with the horizontal, as illustrated in Figure 5-4a, then the velocity vector will always be deflected away from the shock center-line, and it is not possible to satisfy $\theta_{u2} = 0$. Similarly, when the upstream velocity angle is negative $\theta_{u1} < 0$, but the magnitude of the velocity angle is $|\theta_{u1}| > \pi/2 - \alpha/2$, the velocity vector will be deflected clockwise away from the shock center-line, and the post-shock velocity will not be parallel to the horizontal. This scenario is illustrated in 5-4b, where the tangential components of the upstream and downstream velocity are negative. The only situation in which the velocity vector is deflected towards the shock center-line is when the upstream velocity angle is negative $\theta_{u1} < 0$ and its magnitude is $|\theta_{u1}| \leq \pi/2 - \alpha/2$. In this case, as depicted in Figure 5-4c, the tangential components of the upstream and downstream velocity are positive, and the velocity vector is deflected counter-clockwise towards the shock center-line.

By setting $\theta_{u2} = 0$, we can simplify Equation(s) 5.4. The deflection angle becomes $\phi = -\theta_{u1}$, while the shock angle becomes $\sigma = \alpha/2 + \phi$. We must now determine possible values of the upstream velocity angle θ_{u1}. One limiting case is that of $\theta_{u1} = \phi = 0$, for which the velocity vector remains undeflected. In this case, the shock angle is equal to the shock opening half-angle $\alpha/2$, and corresponds to the Mach angle $\mu = \sin^{-1}(1/M_1)$. Therefore, the upstream Mach number M_1 for $\phi = 0$ is simply:

$$M_1|_{\phi=0} = \frac{1}{\sin(\alpha/2)} = 5.8 \pm 0.9 \tag{5.6}$$

What is the maximum possible magnitude of θ_{u1}? We already know that the magnitude of θ_{u1} must satisfy $|\theta_{u1}| \leq \pi/2 - \alpha/2$ for the velocity vector to be deflected towards the shock center-line. Furthermore, the deflection angle ϕ must be less than some maximum deflection angle $\phi_{\max}$ beyond which an attached oblique shock solution does not exist. This imposes an additional upper bound on the value of θ_{u1}. The value of $\phi_{\max}$ depends on the upstream Mach number, and can be less than the geometrically-imposed bound of $\pi/2 - \alpha/2$. For example, for an upstream Mach number of $M_1 \sim 5$, $\phi_{\max} \approx 60°$. For our system, we can also expect values of θ_{u1} to be much smaller than $\phi_{\max}$. This is because the magnetic pressure, which accelerates the plasma in the radial direction, dominates the thermal pressure, which causes the azimuthal expansion, such that

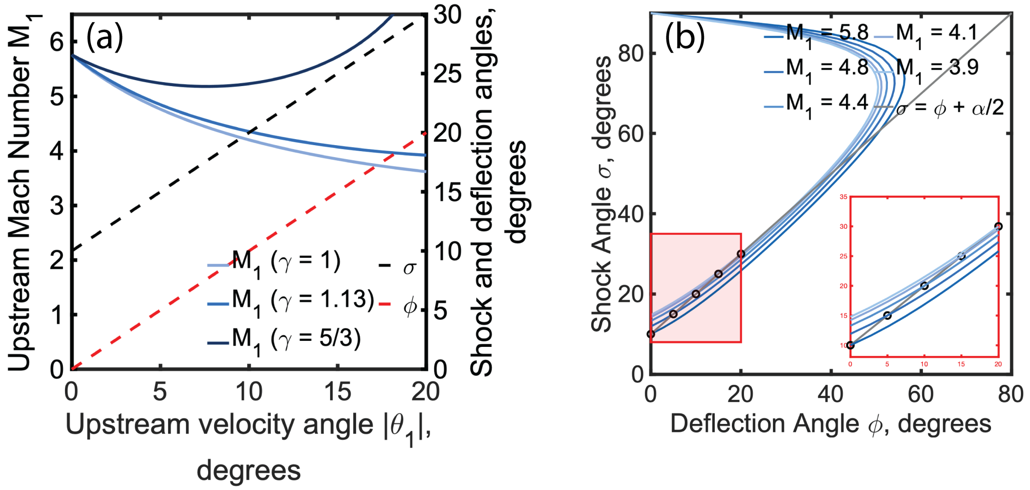

Figure 5-5: (a) Upstream Mach number as a function of the upstream velocity angle θ_{u1} for the case $\theta_{u2} = 0$ and $\alpha/2 \approx 10$ degree. The upstream Mach number for $\gamma = 1$, 1.13 and 5/3 are represented by the blue curves. The deflection and shock angles are represented by the red and black dashed lines respectively. For the given shock geometry, we expect the upstream Mach number to very between $4 < M_1 < 6$ for $\gamma = 1.13$. (b) $\sigma - \phi - M_1$ diagram representing possible upstream Mach number curves for possible values of shock and deflection angles at $\gamma = 1.13$. The blue curves represent the solution of Equation 5.5 for different M_1. The grey line represents the geometric relationship between the shock and deflection angles. Possible solutions of the upstream Mach number can be determined from the points of the grey and blue curves.

the upstream velocity will approach the shock front at shallow angles rather than steep angles. Using Equation 5.5, we calculate the expected upstream Mach number in the range $0 \leq |\theta_{u1}| \leq 20°$, as shown in Figure 5-5a. We calculate the upstream Mach number for $\gamma = 1.13$, which is the expected value of the polytropic index for an aluminum plasma with $n_e \sim 10^{18}$ cm^{-3} and $T_e \sim 10$ eV (Drake et al. [1998]; Swadling et al. [2013]). The calculated upstream Mach number varies between $4 < M_1 < 6$ for the given oblique shock geometry. The Mach number curves for the isothermal $\gamma = 1$ and the adiabatic $\gamma = 5/3$ cases are also shown in Figure 5-5a.

We can gain additional insight by representing the solution using a $\sigma - \phi - M_1$ diagram, as shown in 5-5b. The blue curves represent the solution of Equation 5.5 for different M_1. For a given upstream Mach number, possible solutions of the shock angle σ vary between σ =90° (normal shock) to $\sigma = 1/\mu$ (Mach shock). For both these cases, there is no deflection of the velocity vector, i.e. $\phi = 0$. For constant M_1, a straight oblique shock solution only exists for $\phi \leq \phi_{\max}$, and for $\phi < \phi_{\max}$ and constant M_1, there are two possible solutions for the shock angle σ. If the solution lies above the $\phi = \phi_{\max}$ line, the shock is said to be strong, otherwise it is said to be weak. For a strong shock, the downstream flow is always subsonic, while for a weak shock, the downstream flow is usually super-

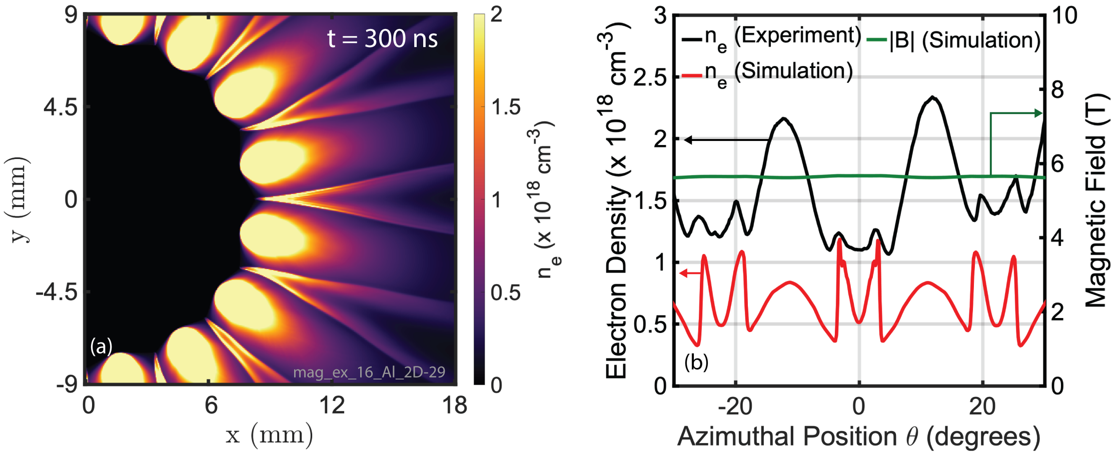

Figure 5-6: (a) Simulated electron density map from 2D resistive MHD GORGON simulation at 300 ns after current start, showing oblique shocks with hollow density profiles. (b) Line-out of the simulated electron density along the azimuthal direction at radial distances of R = 13 mm from the array center. We compare the line-out of electron density from the simulation (red line) with the line-averaged electron density measured using laser interferometry from the experiment (black line). The magnetic field (green line) changes negligibly across the shock fronts.

sonic, except for in a narrow range where ϕ is close to ϕ_{max}.

The grey line in Figure 5-5b represents the geometric relationship between σ and ϕ based on the observed shock geometry. To determine the upstream Mach number for a given deflection angle, we look for the Mach number for which the blue and grey curves intersect. We observe that for higher values of the deflection angle, the upstream Mach number must decrease, which is consistent with what we observe in Figure 5-5a for $\gamma = 1.13$. We also expect the deflection angle to be smaller than the maximum possible deflection angle, such that the oblique shock is weak, and the post-shock flow remains supersonic.

5.3 Comparison with Simulation

We perform 2D resistive MHD simulations of a 16 mm diameter exploding wire array with 16 equally-spaced 30 µm aluminum wires using GORGON. A sine-squared current profile (I_{pk} = 1.4 MA, t_{rise} = 240 ns) is applied to the load. The simulation domain is a square with dimensions 60 × 60 mm^2, and a resolution of $\Delta x \approx 40\,\mu$m. The wire core diameter is set to ~120 µm.

Figure 5-6a shows the simulated electron density map at 300 ns after currents start.

Oblique shock fronts, characterized by sharp discontinuities in electron density, form between the streams of ablating plasma. The shock opening-half angle is $\alpha/2 = 9° \pm 1.5°$, which is in good agreement with the experimentally observed shock opening half-angle. The simulated oblique shocks also exhibit a hollow profile similar to the experimentally observed shocks, although the ratio of the post-shock electron density between the shock fronts and the shock center-line is larger for the simulated shock fronts than for the experimentally observed shocks. We compare the line-out of the electron density from the simulation with the line-averaged electron density from the experiment, as shown in Figure 5-6b. We compute the line-averaged electron density by dividing the line-integrated electron density obtained from laser interferometry by the height of the array. The simulation predicts a ~1.5-2.5x smaller electron density than that observed in the experiment. In the simulation, the post-shock electron density jumps by ~ 2x compared to the density just upstream of the shock. The post-shock density near the shock fronts ($\sim 1 \times 10^{18}$ cm^{-3}) is larger than that in the ablating jets ($\sim 0.7 \times 10^{18}$ cm^{-3}), while in the experiment, the post-shock density is smaller than that in the jets. Figure 5-6b also shows that the magnetic field remains relatively unchanged across the shock front, which confirms that the shock is predominantly hydrodynamic in nature.

It is possible to determine the velocity angles directly from the simulation. The angles formed by the upstream and downstream velocity with the horizontal are $\theta_{u1} \approx -4°$ and $\theta_{u2} \approx 1$ °. The values of the velocity angles from the simulation are consistent with our assumption that the upstream velocity approaches the shock front at a shallow angle, and that the downstream velocity is deflected towards the shock center-line, and is approximately parallel to it. From Equation(s) 5.4, the deflection and shock angles are $\phi \approx 5°$ and $\sigma \approx 13°$. For $\gamma \approx 1.13$, the expected upstream Mach number is $M_{s,1} \approx 5.8$.

We can compare this value of the upstream Mach number obtained from the shock geometry with that obtained from the simulated fluid properties. In order to do so, we calculate the ion sound speed $C_s = \sqrt{\gamma Z T_e / m_i}$ of the plasma. Here, Z is the ionization level, T_e is the electron temperature, and m_i is the ion mass. The values computed for different γ are summarized in Table 5.1. The Mach number calculated from the sound speed is higher than that calculated from the shock geometry for the simulated oblique shocks. One possible explanation for this discrepancy could be significant radiative cooling of the post-shock plasma. The post-shock plasma is hot and dense, and will therefore lose internal energy, and hence pressure, due to radiative losses. The lower post-shock pressure will result in a smaller opening half-angle, and thus, a smaller shock angle. The effect is that the grey line in the $\sigma - \phi - M_1$ diagram (Figure 5-5b) will shift downwards, and we will need a larger M_1 to produce the same deflection across the shock front. This would explain why the geometry of the oblique shock predicts a smaller upstream Mach number than that calculated directly from the fluid properties of the upstream plasma.

Table 5.1: Upstream Mach number determined from shock geometry and fluid properties from GORGON simulation. The experimental Mach numbers are calculated for a deflection angle of 5°

	Simulation			Experiment
γ	C_s ($\mathrm{km\,s^{-1}}$)	M_S (Fluid)	M_S (Geometry)	M_S (Geometry)
1.0	7.5	8.8	5.7 $\pm$0.9	4.7
1.13	8.0	8.3	5.8 $\pm$0.9	4.8
1.67	9.7	6.8	6.4 $\pm$1.3	5.2

5.4 Summary and Future Work

In this chapter, we have presented experimental results and discussion of oblique shocks generated in a supersonic magnetized plasma due to collision azimuthally expanding jets of ablating plasma in an exploding wire array. The plasma was generated using a pulsed-power driven exploding wire array with 16 equally-separated aluminum wires. End-on Mach-Zehnder laser interferometry was used to diagnose the line-integrated electron density.

Interferometry images taken at 300 ns after current start show well-defined oblique shocks between streams of plasma ablating from the wire cores. The oblique shocks appear as sharp discontinuities in the electron density, and exhibit a hollow density structure, where the electron density is high close to the shock fronts and lower near the shock center-line. The shock opening half-angle, measured from the shock geometry, was observed to be $\alpha/2 = 10° \pm 1.4°$.

In order to estimate the upstream Mach number of the flow, we apply simplifying assumptions. We assume that the shock is hydrodynamic-like, because the component of the magnetic field tangential to the shock front is expected to be small compared to that normal to the shock front. We also assume that the post-shock velocity is approximately parallel to the shock center-line, and that the upstream velocity approaches the shock front at shallow angles with the center-line. With these assumptions, we estimate an upstream sonic Mach number in the range $4.5 < M_1 < 6$ for deflection angles between $0° < \phi < 10°$.

We compare our results with 2D resistive MHD simulations in GORGON. The simulation successfully reproduces important features of the experiment. The simulated oblique shocks exhibit hollow density profiles, and have an opening half-angle of $\alpha/2 = 9° \pm 1.5°$, which is in good agreement with the experimentally observed geometry. The angles formed by the upstream and downstream velocity with the horizontal in the simulation are $\theta_{u1} \approx -4°$ and $\theta_{u2} \approx 1\,°$. The values of the velocity angles from the simulation are consistent with our assumption that the upstream velocity approaches the shock front at a shallow angle, and that the downstream velocity is deflected towards the shock centerline and is approximately parallel to it. We use the velocity angles and the shock geometry from the simulation to determine the expected upstream sonic Mach number $M_{s,1} \sim 6$. We can also compare the Mach number determined from the shock geometry to the one directly computed from the plasma ion sound speed. The Mach number calculated from the sound speed is higher than that calculated from the shock geometry for the simulated oblique shocks.

In order to compare the experimentally observed oblique shock geometry with the expected geometry from the plasma sound speed, we must determine the upstream Mach number, velocity, temperature, and the direction of the upstream and downstream velocity in the plasma. We can do this using the ion feature of Optical Thompson scattering, which allows us to determine the ion and electron temperatures from the width and separation of the ion acoustic peaks, and the velocity along the scattering vector from the Doppler shift of the scattered signal. By collecting the scattered light along two different directions, we can also determine the velocity angle. We can collect the scattered radiation along multiple control volumes across the shock front, which will allow us to determine how the velocity, temperature, and sound speed change across the oblique shock.

Chapter 6

Conclusions

The results presented in this thesis provide insight into the physics of 3D magnetized bow shocks and quasi-2D oblique plasma shocks, which are of relevance to many astrophysical plasma flows, such as in extrastellar and protostellar jets (Smith [2012]; Smith et al. [2003]; Remington et al. [2006]). Magnetohydrodynamic shocks can exhibit complex structures, where the frozen-in magnetic field can also be compressed along with the density, and the orientation of the upstream magnetic field can modify the shock dynamics (Goedbloed et al. [2010]; De Sterck et al. [1998]). Furthermore, the magnetic field may also pile up, slip past or diffuse through a resistive obstacle, further complicating the shock dynamics (Burdiak et al. [2017]; Suttle et al. [2019]).

We generate a supersonic and super-Alfvénic collisional plasma flow using a pulsed-power driven 16-wire Aluminum wire array, and the interaction of the plasma flow with inductive probes generates detached bow shocks (Figure 5-1). Interferometry images taken at 300 ns after current start show a well-defined detached bow shock ahead of the probe (Figure 4-3) . The bow shock has a 3D structure, with a larger opening angle in the end-on plane than in the side-on plane. Part of this effect is due to the radially diverging nature of the upstream flow, so to calculate the shock angle, we must account for the direction of the upstream velocity. Far from the obstacle, the shock angle asymptotically approaches the Mach angle, which represents the shock angle for an infinitesimally weak shock. From the shock geometry, the Mach angle is 11°±0.5° in the end-on plane, and 7°±0.5° in the side-on plane. These correspond to upstream Mach numbers of 5.2±0.3 (end-on) and 8.2±0.6 (side-on). The Mach angle is ~ 3° higher in the end-on plane than in the side-on plane, which suggests that line-bending and pile-up of magnetic flux, as illustrated in Figure 4-10, which can result in larger opening angles in the end-on plane, may play a role in the shock dynamics.

We also introduce a novel technique to estimate the flow velocity and temperature of pulsed-power driven plasmas, via simultaneous imaging of inductive probes and measurement of the inductive probe signal. Using the time-of-flight of the plasma to the probe, we estimate the time-resolved flow velocity, which varies from $\sim 100\ \mathrm{km\,s^{-1}}$ early in time to $\sim 60\ \mathrm{km\ s^{-1}}$ later in time (Figure 4-5). The calculated flow velocity closely matches the flow velocity of $50-100\ \mathrm{km\,s^{-1}}$ reported in literature using Thompson scattering measurements for similar pulsed-power driven Aluminum plasmas (Burdiak et al. [2017], Lebedev et al. [2014]), and with our 3D resistive MHD simulations. Furthermore, from the velocity and the shock geometry, we estimate the ion sound speed, and therefore the product of the electron temperature and ionization ZT_e of the plasma. The estimated value of ZT_e is 35 ± 14 eV and 14 ± 6 for end-on and side-on values of the Mach number respectively, and includes the value of 42 eV determined using Thompson scattering for a similar plasma (Burdiak et al. [2017], Lebedev et al. [2014]).

We also investigate the formation of standing oblique shocks due to collision azimuthally expanding jets of ablating plasma in the exploding wire array. Interferometry images show well-defined oblique shocks between streams of plasma ablating from the wire cores. The oblique shocks exhibit a hollow density structure, where the electron density is high close to the shock fronts and lower near the shock center-line (Figure 5-2). The shock opening half-angle, measured from the shock geometry, is $\alpha/2 = 10° \pm 1.4°$.

We estimate an upstream sonic Mach number in the range $4.5 < M_1 < 6$ for deflection angles between $0° < \phi < 10°$ (Figure 5-5a). Representing the solution on a $\sigma - \phi - M_1$ diagram (Figure 5-5b) shows that the oblique shocks are weak shocks, and that the post-shock velocity will remain supersonic. This analysis of the oblique shock is based on certain simplifying assumptions. We assume that the shock is hydrodynamic-like, because the component of the magnetic field tangential to the shock front is expected to be small compared to that normal to the shock front. We also assume that the post-shock velocity is approximately parallel to the shock center-line, and that the upstream velocity approaches the shock front at shallow angles with the center-line. 2D resistive MHD simulations of an exploding wire array justify these assumptions.

Future work will investigate the effect of magnetic field pile-up on the shock dynamics of bow shocks, and directly determine the velocity direction and temperature, and hence the Mach number, of the upstream flows for both oblique and bow shocks. To do this, we aim to implement Faraday polarimetry and Thompson Scattering. Using the ion feature of Optical Thompson scattering (Figure 4-11), we expect to resolve well-defined ion acoustic peaks, which will help us determine the ion and electron temperatures from the peak width and separation, and the flow velocity from the overall Doppler shift. We also aim to better measure the shock angle using refractive-index based techniques such as laser shadowgraphy and Schlieren imaging. The experimental campaign will be supported by resistive MHD simulations in GORGON, where we perform 3D simulations on finer grids to decrease the effect of numerical diffusivity, which will allow us to better understand the role of magnetic field pile-up in 3D bow shock dynamics.

Appendix A

Derivation of the Electromagnetic Wave Dispersion Relation in Plasmas

Here, a derivation of the wave dispersion relation in plasmas based on the treatment by Hutchinson [2002] is presented.

An electromagnetic wave obeys Maxwell's equations:

$$\nabla \times \mathbf{B} = \mu_0 \mathbf{j} + \mu_0 \epsilon_0 \frac{\partial \mathbf{E}}{\partial t} \tag{A.1}$$

$$\nabla \times \mathbf{E} = -\frac{\partial \mathbf{B}}{\partial t} \tag{A.2}$$

Taking the curl of A.2 and substituting A.1, we get:

$$\nabla \times \nabla \times \mathbf{E} = -\frac{\partial}{\partial t} \nabla \times \mathbf{B} \tag{A.3}$$

$$\nabla \times \nabla \times \mathbf{E} = -\frac{\partial}{\partial t} (\mu_0 \mathbf{j} + \mu_0 \epsilon_0 \frac{\partial \mathbf{E}}{\partial t}) \tag{A.4}$$

If we express the electric and magnetic fields as a superposition of uniform homogeneous zero-th order components and time and space varying first order components (of the form $\sim e^{-i\omega t} e^{i\mathbf{k}\cdot\mathbf{x}}$), we can express the wave equation as:

$$\mathbf{k} \times (\mathbf{k} \times \mathbf{E}) = -\frac{i\omega}{c^2}\left(\frac{\mathbf{j}}{\epsilon_0} - i\omega\mathbf{E}\right) \tag{A.5}$$

Where we have made the substitution $c^2 = 1/\mu_0\epsilon_0$. Making the substitution $\mathbf{k} \times (\mathbf{k} \times \mathbf{E}) = \mathbf{k}(\mathbf{k} \cdot \mathbf{E}) - \mathbf{k^2}\mathbf{E}$, we get:

$$\mathbf{k}(\mathbf{k} \cdot \mathbf{E}) - k^2\mathbf{E} + \frac{\omega^2}{c^2}\mathbf{E} + \frac{i\omega}{c^2\epsilon_0}\mathbf{j} = 0 \tag{A.6}$$

In a vacuum, $\mathbf{j} = 0$ and $\nabla \times \mathbf{E} = 0$, so the dispersion relation for an electromagnetic wave propagating in vacuum becomes:

$$\omega^2 = c^2 k^2 \tag{A.7}$$

In a medium, the current $\mathbf{j} = \sigma \cdot \mathbf{E}$ can be written as the dot product of the conductivity tensor and the electric field. Thus, we get:

$$\left(\mathbf{kk} + (\frac{\omega^2}{c^2} - k^2)\mathbf{I} + \frac{i\omega}{c^2\epsilon_0}\boldsymbol{\sigma}\right) \cdot \mathbf{E} = 0 \tag{A.8}$$

Introducing the dielectric tensor $\boldsymbol{\epsilon} = \mathbf{I} + i\boldsymbol{\sigma}/(\omega\epsilon_0)$, we can write:

$$\left(\mathbf{kk} - k^2\boldsymbol{I} + \frac{\omega^2}{c^2}\boldsymbol{\epsilon}\right) \cdot \boldsymbol{E} = 0 \tag{A.9}$$

We can determine an expression for the conductivity tensor $\boldsymbol{\sigma}$, and hence for the dielectric tensor $\boldsymbol{\epsilon}$ from:

$$\boldsymbol{j} = \sum_s \boldsymbol{j}_s = \sum_s n_s q_s \boldsymbol{v}_s \equiv \sum_s \boldsymbol{\sigma}_s \cdot \boldsymbol{E} \tag{A.10}$$

Where n_s, q_s and $\boldsymbol{v_s}$ are the number density, charge and the velocity of species s (electron and ion) in the plasma. From the plasma fluid momentum equation, we can determine the velocity as a function of the electric field. Here, we assume a cold plasma and neglect collisions.

$$m_s \frac{D\boldsymbol{v}_s}{Dt} = q_s \left(\mathbf{E} + \boldsymbol{v}_s \times \mathbf{B}\right) \tag{A.11}$$

Assuming the zero-th order magnetic field is $\boldsymbol{B}_0 = B_0 \hat{\boldsymbol{z}}$, and that the zero-th order velocity and electric fields are zero, we get:

$$m_s \frac{\partial \boldsymbol{v}_s}{\partial t} = q_s \left(\mathbf{E} + \boldsymbol{v}_s \times \mathbf{B}_0\right) \tag{A.12}$$

$$-i m_s \omega \begin{pmatrix} v_x \\ v_y \\ v_z \end{pmatrix}_s = q_s \begin{pmatrix} E_x \\ E_y \\ E_z \end{pmatrix} + q_s \begin{pmatrix} v_y B_0 \\ -v_x B_0 \\ 0 \end{pmatrix}_s \tag{A.13}$$

Or:

$$v_{x,s} = \frac{q_s}{m_s} \left(\frac{i\omega E_x - \Omega_s E_y}{\omega^2 - \Omega_s^2} \right) \tag{A.14}$$

$$v_{y,s} = \frac{q_s}{m_s} \left(\frac{i\omega E_y + \Omega_s E_x}{\omega^2 - \Omega_s^2} \right) \tag{A.15}$$

$$v_{z,s} = \frac{q_s}{m_s} \left(\frac{i E_z}{\omega} \right) \tag{A.16}$$

Here, $\Omega = qB_0/m$ is the cyclotron frequency. The current density $\boldsymbol{j}$ is:

$$j_{x,s} = \epsilon_0 \frac{q_s^2 n_s}{m_s \epsilon_0} \left(\frac{i\omega E_x - \Omega_s E_y}{\omega^2 - \Omega_s^2} \right) = \epsilon_0 \omega_{p_s}^2 \left(\frac{i\omega E_x - \Omega_s E_y}{\omega^2 - \Omega_s^2} \right) \tag{A.17}$$

$$j_{y,s} = \epsilon_0 \frac{q_s^2 n_s}{m_s \epsilon_0} \left(\frac{i\omega E_y + \Omega_s E_x}{\omega^2 - \Omega_s^2} \right) = \epsilon_0 \omega_{p_s}^2 \left(\frac{i\omega E_y + \Omega_s E_x}{\omega^2 - \Omega_s^2} \right) \tag{A.18}$$

$$j_{z,s} = \epsilon_0 \frac{q_s^2 n_s}{m_s \epsilon_0} \left(\frac{iE_z}{\omega} \right) = \epsilon_0 \omega_{p,s}^2 \left(\frac{iE_z}{\omega} \right) \tag{A.19}$$

Here, $\omega_p = \sqrt{q^2 n/(\epsilon_0 m)}$ is the plasma frequency. Thus, the current denisty j can be represented as:

$$\boldsymbol{j}_s = \boldsymbol{\sigma}_s \cdot \boldsymbol{E} = \epsilon_0 \omega_{p,s}^2 \begin{bmatrix} \frac{i\omega}{\omega^2-\Omega_s^2} & \frac{-\Omega_s}{\omega^2-\Omega_s^2} & 0 \\ \frac{\Omega_s}{\omega^2-\Omega_s^2} & \frac{i\omega}{\omega^2-\Omega_s^2} & 0 \\ 0 & 0 & i/\omega \end{bmatrix} \tag{A.20}$$

And the dielectric tensor $\boldsymbol{\epsilon}$ is:

$$\boldsymbol{\epsilon} = \mathbf{I} + i \frac{\sum_s \boldsymbol{\sigma}_s}{\omega \epsilon_0} = \begin{bmatrix} S & -iD & 0 \\ iD & S & 0 \\ 0 & 0 & P \end{bmatrix} \tag{A.21}$$

Where:

$$S = 1 - \sum_s \frac{\omega_{p,s}^2}{\omega^2 - \Omega_s^2} \tag{A.22}$$

$$D = \sum_s \frac{\Omega_s}{\omega} \frac{\omega_{p,s}^2}{\omega^2 - \Omega_s^2} \tag{A.23}$$

$$P = 1 - \sum_s \frac{\omega_{p,s}^2}{\omega^2} \tag{A.24}$$

In the case, where the ion contribution is small, i.e. $\omega\ \Omega_i >> 1$, we can approximate S, P and D as functions of the electron contribution only.

Assuming the wavevector k is in the yz plane and forms an angle θ with the unperturbed magnetic field $B_0\hat{z}$, the dyadic product kk becomes:

$$kk = k^2 \begin{bmatrix} \sin^2\theta & 0 & \sin\theta\cos\theta \\ 0 & 0 & 0 \\ \sin\theta\cos\theta & 0 & \cos^2\theta \end{bmatrix} \tag{A.25}$$

We can now construct the dispersion matrix as:

$$\boldsymbol{D} = \left(\boldsymbol{kk} - k^2\boldsymbol{I} + \frac{\omega^2}{c^2}\boldsymbol{\epsilon}\right) \tag{A.26}$$

$$D = \begin{bmatrix} k^2\sin^2\theta - k^2 + \frac{\omega^2}{c^2}S & -iD\frac{\omega^2}{c^2} & k^2\sin\theta\cos\theta \\ iD\frac{\omega^2}{c^2} & -k^2 + \frac{\omega^2}{c^2}S & 0 \\ k^2\sin\theta\cos\theta & 0 & k^2\cos^2\theta - k^2 + \frac{\omega^2}{c^2}P \end{bmatrix} \tag{A.27}$$

$$D = \begin{bmatrix} -k^2\cos^2\theta + \frac{\omega^2}{c^2}S & -iD\frac{\omega^2}{c^2} & k^2\sin\theta\cos\theta \\ iD\frac{\omega^2}{c^2} & -k^2 + \frac{\omega^2}{c^2}S & 0 \\ k^2\sin\theta\cos\theta & 0 & -k^2\sin^2\theta + \frac{\omega^2}{c^2}P \end{bmatrix} \tag{A.28}$$

Multiplying with c^2/ω^2 throughout, and using the relation $\boldsymbol{N} = \boldsymbol{k}c/\omega$ for the refractive index n:

$$\boldsymbol{D_n} \cdot \boldsymbol{E} = \begin{bmatrix} -N^2\cos^2\theta + S & -iD & N^2\sin\theta\cos\theta \\ iD & -N^2 + S & 0 \\ N^2\sin\theta\cos\theta & 0 & -N^2\sin^2\theta + P \end{bmatrix} \cdot \boldsymbol{E} = 0 \tag{A.29}$$

For non-trivial solutions the determinant of the dispersion matrix must be zero, i.e $det(\boldsymbol{D_n}) = 0$.

For the case where the unperturbed magnetic field is small i.e. $\Omega/\omega \approx 0$, and considering only the electron contribution, we get:

$$S = 1 - \frac{\omega_{p,e}^2}{\omega^2 - \Omega_e^2} \approx 1 - \frac{\omega_{p,e}^2}{\omega^2} = P \tag{A.30}$$

$$D = \frac{\Omega_e}{\omega}\frac{\omega_{p,e}^2}{\omega^2 - \Omega_e^2} \approx 0 \tag{A.31}$$

$$P = 1 - \frac{\omega_{p,e}^2}{\omega^2} \tag{A.32}$$

The dispersion tensor is:

$$\det\begin{bmatrix} -N^2\cos^2\theta + P & 0 & N^2\sin\theta\cos\theta \\ 0 & -N^2 + P & 0 \\ N^2\sin\theta\cos\theta & 0 & -N^2\sin^2\theta + P \end{bmatrix} = 0 \tag{A.33}$$

The only non-trivial solution is:

$$n^2 = P \tag{A.34}$$

Or

$$\omega^2 = c^2k^2 + w_p^2 \tag{A.35}$$

This wave propagating through the plasma is termed the ordinary wave. For the case where the wave vector is perpendicular to the unperturbed magnetic field, i.e. $\theta = \pi/2$, the determinant of the dispersion tensor is:

$$\det\begin{bmatrix} S & -iD & 0 \\ iD & -N^2 + S & 0 \\ 0 & 0 & -N^2 + P \end{bmatrix} = 0 \tag{A.36}$$

$$(P - n^2)\left(S(S - n^2) - D^2\right) = 0 \tag{A.37}$$

The solutions are:

$$N^2 = P \tag{A.38}$$

$$N^2 = \frac{S^2 - D^2}{S} \tag{A.39}$$

The first solution represents an ordinary (O) wave, while the second solution represents the extraordinary (X) wave.

Similarly, when the wave vector is along the unperturbed magnetic field $\theta = 0$, we get:

$$\det \begin{bmatrix} -N^2+S & -iD & 0 \\ iD & -N^2+S & 0 \\ 0 & 0 & P \end{bmatrix} = 0 \tag{A.40}$$

$$P((S-N^2)^2 - D^2) = 0 \tag{A.41}$$

The solutions are:

$$P = 0, \quad N^2 = S+D, \quad N^2 = S-D \tag{A.42}$$

The solutions represent the electron plasma waves, and the right and left circularly polarized waves respectively. We can verify that the last two expressions result in circularly polarized waves by substituting $N^2 = S \pm D$ into the dispersion relation.

$$\frac{E_x}{E_y} = \frac{iD}{S-(S \pm D)} = \pm i \tag{A.43}$$

The dispersion relation or the right and left circularly polarized waves can be written as:

$$R = S + D = 1 - \frac{\omega_{pe}^2}{\omega(\omega + \Omega_e)} \tag{A.44}$$

$$L = S - D = 1 - \frac{\omega_{pe}^2}{\omega(\omega - \Omega_e)} \tag{A.45}$$

Here, we have assumed that the ion contribution is small compared to the electron contribution.

These solutions apply for the case of a constant and uniform background medium. The Fourier transformation $\sim e^{-i\omega t} e^{i\boldsymbol{k}\cdot\boldsymbol{x}}$ no longer applies in media with spatial gradients. However, for the case where the medium is slowly varying, the WKB (Wentzel, Kramers Brillouin) approximation can be used:

$$E \sim \exp\left(\int \boldsymbol{k}\cdot \boldsymbol{dl}\right) \exp(-i\omega t) \tag{A.46}$$

The WKB approximation is valid when:

$$\frac{|\nabla k|}{k^2} << 1 \tag{A.47}$$

Appendix B

Derivation of the Thompson scattering Spectral Density Function

An electromagnetic wave incident on an electron causes it to accelerate. The accelerating charge then emits electromagnetic radiation. This is the scattered electromagnetic field. In a particular scattering volume, the total scattered field is due to the contribution of all electrons within the volume. The time-averaged power is then measured using a spectrometer. Here, we derive the power spectrum for Thompson scattering. the derivationin based on the treatnet by Sheffield et al. [2010] and Hutchinson [2002].

B.1 Scattered Power Spectrum

The scattered electric field $\mathbf{E_s}$ at position $R\hat{\mathbf{s}}$ in the far-field ($R >> L$) due to particle of charge q moving with velocity $\mathbf{v} = \boldsymbol{\beta} c$ is given by:

$$\mathbf{E_s}(\mathbf{R}, t) = \frac{q}{cR}\left[\frac{\hat{\mathbf{s}} \times \hat{\mathbf{s}} - \boldsymbol{\beta} \times \boldsymbol{\beta}}{(1 - \hat{\mathbf{s}} \cdot \dot{\boldsymbol{\beta}})^3}\right]_{ret} \tag{B.1}$$

In the non-relativistic limit $\beta \rightarrow 0$, the scattered field becomes:

$$\mathbf{E_s}(\mathbf{R}, t) = \frac{q}{cR}\left[\hat{\mathbf{s}} \times (\hat{\mathbf{s}} \times \dot{\boldsymbol{\beta}})\right]_{ret} \tag{B.2}$$

Here, the values are calculated at retard ted time $t' \approx t - R/c + \mathbf{r} \cdot \hat{\mathbf{s}}/c$ due to the time it takes the wave to reach the observer at $\mathbf{R}$.

In the low-temperature limit, assuming $\mathbf{B} = 0$, the acceleration due to a monochromatic incident field $\mathbf{E_i} = \mathbf{E_{i0}} \mathbf{e}^{\mathbf{k_i}\cdot\mathbf{r}-\omega_\mathbf{i}\mathbf{t}'}$ is:

$$\dot{\boldsymbol{\beta}} = \frac{-eE_{io}}{m_e c} \exp(\mathbf{k_i} \cdot \mathbf{r} - \omega_i t')\mathbf{\hat{E}_{io}} \tag{B.3}$$

And the scattered field from a single electron is:

$$\mathbf{E_s}(\mathbf{R}, t) = \frac{r_e E_{i0}}{R} \left[\mathbf{\hat{s}} \times (\mathbf{\hat{s}} \times \mathbf{\hat{E}_{io}})\right]_{ret} \exp(\mathbf{k_i} \cdot \mathbf{r} - \omega_i t') \tag{B.4}$$

Where $r_e = e^2/m_e c^2$ is the classic electron radius.

The total scattered field is the contribution from all electrons in the scattering volume.We define the total scattered field $\mathbf{E_s^T}$ as:

$$\mathbf{E_s^T}(\mathbf{R}, t) = \int d\mathbf{r} \int d\mathbf{v} F(\mathbf{r}, \mathbf{v}, t')\mathbf{E_s}(\mathbf{R}, t) \tag{B.5}$$

Where $F(\mathbf{r}, \mathbf{v}, t') = \delta(\mathbf{v} - \mathbf{v_j})\delta(\mathbf{r} - \mathbf{r_j})$ is the point distribution function of the electrons at time t'.

The total scattered power along $\mathbf{\hat{s}}$ is calculated by the area integral of the energy flux or Poynting vector. For an electromagnetic wave, the energy flux along $\mathbf{\hat{s}}$ is

$$\mathbf{q} = (c/4\pi)\mathbf{E_s}\mathbf{B} \cdot \mathbf{\hat{s}} = (c/4\pi)|E_s^T|^2 \tag{B.6}$$

We are interested in the time-averaged power per unit solid angle over time T, which is:

$$\frac{d\bar{P}}{d\Omega_s} = \frac{cR^2}{4\pi} \lim_{T\to\infty} \frac{1}{T} \int_{-T/2}^{T/2} |\mathbf{E_s^T}(\mathbf{t})|^\mathbf{2} \tag{B.7}$$

Using Percival's theorem, we get:

$$\frac{d\bar{P}}{d\Omega_s d\omega_s} = \frac{cR^2}{4\pi} \lim_{T\to\infty} \frac{1}{2\pi T} |\mathbf{E}_s^T(\omega_s)|^2 \tag{B.8}$$

Here, $\mathbf{E}^{\mathbf{T}}_{\mathbf{s}}(\omega_{\mathbf{s}})$ is the Fourier transform of $\mathbf{E}^{\mathbf{T}}_{\mathbf{s}}(\mathbf{t}')$, which is:

$$\mathbf{E}^{\mathbf{T}}_{\mathbf{s}}(\omega_{\mathbf{s}}) = \int_{-\infty}^{+\infty} dt e^{i\omega_s t} \mathbf{E}^{\mathbf{T}}_{\mathbf{s}}(\mathbf{t}') \tag{B.9}$$

we can now combine Equations B.8, B.9, B.5 and B.4, to get:

$$\frac{d\bar{P}}{d\Omega_s d\omega_s} = \frac{cR^2}{4\pi} \lim_{T\to\infty} \frac{1}{2\pi T} \left| \int dt e^{i\omega_s t} \int d\mathbf{r} \int d\mathbf{v} F \frac{r_e}{E_{i0}} R \left[\hat{\mathbf{s}} \times (\hat{\mathbf{s}} \times \hat{\mathbf{E}}_{\mathbf{io}}) \right] \exp(i[\mathbf{k_i} \cdot \mathbf{r} - \omega_i t']) \right|^2 \tag{B.10}$$

Carrying out the integral over velocity space, and simplifying we get:

$$\frac{d\bar{P}}{d\Omega_s d\omega_s} = \frac{cE_{i0}^2 r_e^2}{4\pi} \left[\hat{\mathbf{s}} \times (\hat{\mathbf{s}} \times \hat{\mathbf{E}}_{\mathbf{io}}) \right]^2 \lim_{T\to\infty} \frac{1}{2\pi T} \left| \int dt \int d\mathbf{r} n_e(\mathbf{r}, t') e^{i\mathbf{k_i}\cdot\mathbf{r}} e^{-i\omega_i t'} e^{i\omega_s t} \right|^2 \tag{B.11}$$

Substituting for retarded time $t = t' + R/c - \hat{\mathbf{s}} \cdot \mathbf{r}/c$, the exponential terms can be simplified:

$$e^{-i\omega_s t} e^{i\mathbf{k_i}\cdot\mathbf{r}} e^{-i\omega_i t'} = e^{i\omega^- t'} e^{-i\mathbf{k}^-\cdot\mathbf{r}} e^{ik_s R} \tag{B.12}$$

Where $\omega^- = \omega_s - \omega_i$ and $\mathbf{k}^- = \mathbf{k_s} - \mathbf{k_i}$ are the scattering frequency and wave vector respectively.

Next, we perform a inverse Fourier transform of the electron density $n_e(\mathbf{r}, t')$ in time and space.

$$n_e(\mathbf{r}, t') = \int_{-\infty}^{+\infty} \frac{d\mathbf{k}}{(2\pi)^3} \int_{\infty}^{+\infty} \frac{d\omega}{2\pi} e^{i\mathbf{k}\cdot\mathbf{r}} e^{-i\omega t'} n_e(\mathbf{k}, \omega) \tag{B.13}$$

Where, $W = \omega - i\gamma$ is combination of the real and imaginary frequencies. Therefore, we get:

$$\begin{gathered} \frac{d\bar{P}}{d\Omega_s d\omega_s} = \frac{cE_{i0}^2 r_e^2}{4\pi} \left[\hat{\mathbf{s}} \times (\hat{\mathbf{s}} \times \hat{\mathbf{E}}_{\mathbf{io}}) \right]^2 e^{ik_s R} \lim_{T\to\infty} \frac{1}{2\pi T} \\ \left| \int dt' \int d\mathbf{r} \int \frac{d\mathbf{k}}{(2\pi)^3} \int \frac{d\omega}{2\pi} n_e(\mathbf{k}, \omega) e^{i((\mathbf{k}-\mathbf{k}^-)\cdot\mathbf{r}} e^{-i(\omega-\omega^-)t'} \right|^2 \end{gathered} \tag{B.14}$$

Performing the integral over time and space gives us:

$$\int dt' e^{-i(\omega-\omega^{-})t'} = 2\pi\delta(\omega-\omega^{-}) \tag{B.15}$$

$$\int d\mathbf{k} e^{-i(\mathbf{k}-\mathbf{k}^{-})\cdot\mathbf{r}} = (2\pi)^3\delta(\mathbf{k}-\mathbf{k}^{-}) \tag{B.16}$$

And then performing the integral over $\mathbf{k}$ and ω space gives us:

$$\int d\mathbf{k}\int d\omega n_e(\mathbf{k},\omega)\delta(\omega-\omega^{-})(2\pi)^3\delta(\mathbf{k}-\mathbf{k}^{-}) = n_e(\mathbf{k}^{-},\omega^{-}) \tag{B.17}$$

Thus, the power spectrum becomes:

$$\frac{d\bar{P}}{d\Omega_s d\omega_s} = \frac{cE_{i0}^2 r_e^2}{4\pi}\left[\hat{\mathbf{s}}\times(\hat{\mathbf{s}}\times\hat{\mathbf{E}}_{\mathbf{io}})\right]^2 e^{ik_sR}\lim_{T\to\infty}\frac{1}{2\pi T}|n_e(\mathbf{k}^{-},\omega^{-})|^2 \tag{B.18}$$

Redefining $\mathbf{k}=\mathbf{k}^{-}$ and $\omega=\omega^{-}$, and introducing the spectral density function $S(\mathbf{k},\omega)$:

$$S(\mathbf{k},\omega) \equiv \lim_{T\to\infty, V\to\infty}\frac{1}{TV}\left\langle\frac{|n_{\mathrm{e}}(\mathbf{k},\omega)|^2}{n_{eo}}\right\rangle \tag{B.19}$$

Where $n_{e0} = NV$ is the mean electron density, and N is the total number of electron in scattering volume V. Finally, we can express the ensemble-averaged power spectrum as:

$$\left\langle\frac{d\bar{P}}{d\Omega_s d\omega_s}\right\rangle = \frac{q_{in}r_e^2}{2\pi}\left[\hat{\mathbf{s}}\times(\hat{\mathbf{s}}\times\hat{\mathbf{E}}_{\mathbf{io}})\right]^2 e^{ik_sR}NS(\mathbf{k},\omega) \tag{B.20}$$

Where $q_{in} = cE_{i0}^2/(4\pi)$ is the magnitude of the incident energy flux.

B.2 Spectral Density Function

Next we determine the spectral density function $S(\mathbf{k},\omega)$ for a collisionless unmagnetized plasma. We start by expressing the distribution function F_s of species s as the superposition of a mean distribution F_0 and a fluctuating distribution F_1.

$$F_s = F_0 + F_1 \tag{B.21}$$

The evolution of a colissionless plasma is described by the Vlasov equation. The zero-th and first order fields become:

$$\frac{\partial F_0}{\partial t} + \mathbf{v}\cdot\nabla F_0 = 0 \tag{B.22}$$

$$\frac{\partial F_1}{\partial t} + \mathbf{v}\cdot\nabla F_1 + \frac{q}{m}\mathbf{E_1}\cdot\nabla_{\mathbf{v}} F_0 = 0 \tag{B.23}$$

The Poisson equation becomes:

$$\nabla^2\phi_1 = -4\pi\rho_{e,1}(\mathbf{r},t) \tag{B.24}$$

Where ϕ is the electric potential and $\rho_{e,1} = (Zen_{i,1} - en_{e,1})$ is the charge density.

If we assume that the potential varies as $\phi_1 e^{i\mathbf{k}\cdot\mathbf{r}}$, and take the inverse Fourier transform of the charge density, then we can represent the first order potential as:

$$\phi_1 = 4\pi\int \frac{d\mathbf{k}}{k^2(2\pi)^3} e^{i\mathbf{k}\cdot\mathbf{r}}\rho_{e,1}(\mathbf{k},t) \tag{B.25}$$

The electric field then becomes:

$$\mathbf{E}_1 = -\nabla\phi_1 = \frac{-i4\pi}{(2\pi)^3}\int \frac{d\mathbf{k}}{k^2}\mathbf{k}e^{i\mathbf{k}\cdot\mathbf{r}}\rho_{e,1}(\mathbf{k},t) \tag{B.26}$$

Next we take the Fourier-Laplace transform of Equation B.23. For the first term we get:

$$\int d\mathbf{r}\int_0^\infty dt\frac{\partial F_1}{\partial t}e^{-i\mathbf{k}\cdot\mathbf{r}}e^{iWt} = \int_0^\infty dt\frac{\partial F_1(\mathbf{k},t)}{\partial t}e^{iWt} \tag{B.27}$$

$$\begin{aligned}\int_0^\infty dt\frac{\partial F_1(\mathbf{k},t)}{\partial t}e^{iWt} &= \frac{\partial}{\partial t}\int_0^\infty dtF_1(\mathbf{k},t)e^{iWt} - iW\int_0^\infty dtF_1(\mathbf{k},t)e^{iWt} \\ &= \left[F_1(\mathbf{k},t)e^{iWt}\right]_0^\infty - iWF_1(\mathbf{k},W) \\ &= -F_1(\mathbf{k},0) - iWF_1(\mathbf{k},W)\end{aligned} \tag{B.28}$$

Similarly, the Fourier-Laplace transform of the second term is:

$$\int dt\int d\mathbf{r}\mathbf{v}\cdot\frac{\partial F_1}{\partial\mathbf{r}}e^{-i\mathbf{k}\cdot\mathbf{r}}e^{iWt} = \mathbf{v}\cdot\int d\mathbf{r}\frac{\partial F_1(\mathbf{r},W)}{\partial\mathbf{r}}e^{-i\mathbf{k}\cdot\mathbf{r}} \tag{B.29}$$

$$\begin{aligned}\int d\mathbf{r}\frac{\partial F_1(\mathbf{r},W)}{\partial \mathbf{r}}e^{-i\mathbf{k}\cdot\mathbf{r}} &= \frac{\partial}{\partial \mathbf{r}}\int d\mathbf{r}F_1(\mathbf{r},W)e^{-i\mathbf{k}\cdot\mathbf{r}} + i\mathbf{k}\int d\mathbf{r}F_1(\mathbf{r},W)e^{-i\mathbf{k}\cdot\mathbf{r}}\\ &= \left[F_1(\mathbf{r},W)e^{-i\mathbf{k}\cdot\mathbf{r}}\right]_{-\infty}^{+\infty} + i\mathbf{k}F_1(\mathbf{k},W)\\ &= i\mathbf{k}F_1(\mathbf{k},W)\end{aligned} \tag{B.30}$$

Finally, we look at the last term.

$$\int dt\int d\mathbf{k}e^{-i\mathbf{k}\cdot\mathbf{r}}e^{iWt}\frac{q}{m}\mathbf{E_1}(\mathbf{k}',t)\cdot\nabla_{\mathbf{v}}F_0 = \frac{q}{m}\int d\mathbf{r}e^{-i\mathbf{k}\cdot\mathbf{r}}\mathbf{E_1}(\mathbf{k}',W)\cdot\nabla_{\mathbf{v}}F_0 \tag{B.31}$$

$$\frac{q}{m}\int d\mathbf{r}e^{-i\mathbf{k}\cdot\mathbf{r}}\mathbf{E_1}(\mathbf{k}',W)\cdot\nabla_{\mathbf{v}}F_0 = \frac{-i4\pi}{(2\pi)^3}\frac{q}{m}\int d\mathbf{r}\int\frac{d\mathbf{k}'}{k'^2}\mathbf{k}'e^{i\mathbf{k}'-\mathbf{k}\cdot\mathbf{r}}\rho_{e,1}(\mathbf{k}',W)\cdot\nabla_{\mathbf{v}}F_0 \tag{B.32}$$

Performing the integral over r-space and then k-space, we get:

$$\begin{aligned}\frac{q}{m}\int d\mathbf{r}e^{-i\mathbf{k}\cdot\mathbf{r}}\mathbf{E_1}(\mathbf{k}',W)\cdot\nabla_{\mathbf{v}}F_0 &= \frac{-i4\pi q}{m}\int\frac{d\mathbf{k}'}{k'^2}\mathbf{k}'\rho_{e,1}(\mathbf{k}',W)\cdot\nabla_{\mathbf{v}}F_0\delta(\mathbf{k}'-\mathbf{k})\\ &= \frac{-i4\pi q}{k^2 m}\rho_{e,1}(\mathbf{k},W)\mathbf{k}\cdot\nabla_{\mathbf{v}}F_0\end{aligned} \tag{B.33}$$

Therefore, the Fourier-Laplace transform of Equation B.23 is:

$$-F_1(\mathbf{k},0) - iWF_1(\mathbf{k},W) + i\mathbf{v}\cdot\mathbf{k}F_1(\mathbf{k},W) - \frac{i4\pi q}{k^2 m}\rho_{e,1}(\mathbf{k},W)\mathbf{k}\cdot\nabla_{\mathbf{v}}F_0 = 0 \tag{B.34}$$

Re-arranging, we get:

$$F_1(\mathbf{k},W) = i\frac{F_1(\mathbf{k},0)}{W-\mathbf{v}\cdot\mathbf{k}} - \left(\frac{4\pi q}{k^2 m}\right)\frac{\rho_{e,1}(\mathbf{k},W)\mathbf{k}\cdot\nabla_{\mathbf{v}}F_0}{W-\mathbf{v}\cdot\mathbf{k}} \tag{B.35}$$

Summing over all velocities, we get:

$$n_{1e}(\mathbf{k},W) = -i\sum_{j=1}^{N}\frac{e^{i\cdot\mathbf{r_{0,j}}}}{W-\mathbf{v_0}\cdot\mathbf{k}} + \frac{\chi_e(\mathbf{k},W)}{e}\{Zen_{1i}(\mathbf{k},W) - en_{1e}(\mathbf{k},W)\} \tag{B.36}$$

$$n_{1i}(\mathbf{k},W) = -i\sum_{l=1}^{N/Z}\frac{e^{i\cdot\mathbf{r_{0,l}}}}{W-\mathbf{v_0}\cdot\mathbf{k}} - \frac{\chi_i(\mathbf{k},W)}{Ze}\{Zen_{1i}(\mathbf{k},W) - en_{1e}(\mathbf{k},W)\} \tag{B.37}$$

Where the susceptibility of species p is defined as:

$$\chi_p(\mathbf{k},\omega) \equiv \int_{-\infty}^{+\infty} d\mathbf{v} \frac{4\pi Z_p^2 e^2 n_{po}}{m_{\mathrm{i}} k^2} \frac{\mathbf{k}\cdot\partial \hat{f}_{po}/\partial \mathbf{v}}{W - \mathbf{v_0}\cdot\mathbf{k}} \tag{B.38}$$

Finally solving the system of equations B.36-B.37:

$$\begin{split} n_{1e}(\mathbf{k},W) = -\,i \Bigg[\sum_{j=1}^{N} \frac{e^{i\mathbf{k}\cdot\mathbf{r}_j(0)}}{W - \mathbf{v_0}\cdot\mathbf{k}} - \frac{\chi_e}{\epsilon} \sum_{j=1}^{N} \frac{e^{i\mathbf{k}\cdot\mathbf{r}_j(0)}}{W - \mathbf{v_0}\cdot\mathbf{k}} \\ + \frac{Z\chi_e}{\epsilon} \sum_{l=1}^{N/Z} \frac{e^{i\mathbf{k}\cdot\mathbf{r}_l(0)}}{W - \mathbf{v_0}\cdot\mathbf{k}} \Bigg] \end{split} \tag{B.39}$$

The first term represents the contribution from free electrons, the second term represents contribution from the correlation of electrons with other electrons, and the last term represents the contribution from the electrons dressing ions.

Finally, we take the ensemble average to determine the spectral density function:

$$S(\mathbf{k},\omega) = \frac{2\pi}{k} \left|1 - \frac{\chi_e}{\epsilon}\right|^2 \hat{f}_{eo}\left(\frac{\omega}{k}\right) + \frac{2\pi Z}{k} \left|\frac{\chi_e}{\epsilon}\right|^2 \hat{f}_{io}\left(\frac{\omega}{k}\right) \tag{B.40}$$

Here, $\epsilon = 1 + \chi_e + \chi_i$ is the dielectric function, and $\hat{f}_0$ is the unperturbed 1D normalized distribution function. Therefore, we can determine the spectral density function given the species distribution function, and the electron and ion susceptibility functions.

B.3 Electric Susceptibility

Next, we determine an analytical function for the susceptibility.We start with the Vlasov equation for a collisonless unmagnetized plasma.

$$\frac{\partial f}{\partial t} + \mathbf{v}\cdot\nabla f + \frac{q}{m}\mathbf{E}\cdot\nabla_{\mathbf{v}} f = 0 \tag{B.41}$$

We linearize the Vlasov equation using $f = f_0 + f_1, \mathbf{E} = \mathbf{E_1}$, keep only the first order terms, and express the time- and space-varying first-order terms as Fourier components:

$$\begin{aligned} &\frac{\partial f_1}{\partial t} + \mathbf{v}\cdot\nabla f_1 + \frac{q}{m}\mathbf{E_1}\cdot\nabla_{\mathbf{v}} f_0 = 0 \\ &-i\omega f_1 + \mathbf{v}\cdot i\mathbf{k} f_1 = -\frac{q}{m}\mathbf{E_1}\cdot\nabla_{\mathbf{v}} f_0 \\ &f_1 = \frac{-iq}{m}\left(\frac{\mathbf{E_1}\cdot\nabla_{\mathbf{v}} f_0}{\omega - \mathbf{v}\cdot\mathbf{k}}\right) \end{aligned} \tag{B.42}$$

The perturbed current density is:

$$\mathbf{j_1} = \int d\mathbf{v} q\mathbf{v} f_1 = \frac{-iq^2}{m}\int d\mathbf{v}\left(\frac{\mathbf{v_1}\mathbf{E_1}\cdot\nabla_{\mathbf{v}} f_0}{\omega - \mathbf{v}\cdot\mathbf{k}}\right) \tag{B.43}$$

We take the velocity and perturbed electric field to be along k, and let $\hat{f}_k = n_0 f_k$ be the 1D normalized distribution distribution for the isotropic distribution $f_0(\mathbf{v})$.

$$j_1 = \frac{-iq^2 n_0}{m}\int dv\left(\frac{v\partial_v \hat{f}_k}{\omega - vk}\right)E_1 \equiv \sigma E_1 \tag{B.44}$$

In a linear dielectric medium, the current density is the time-rate of change of the polarization current $\mathbf{P}$.

$$\mathbf{j_1} = \frac{1}{4\pi}\frac{\partial \mathbf{P_1}}{\partial t} = \frac{-i\omega\chi\mathbf{E_1}}{4\pi} \tag{B.45}$$

Thus, the susceptibility can be expressed in terms of the conductivity as:

$$\chi = \frac{\omega_p^2}{k^2}\int_{-\infty}^{\infty} dv \frac{\partial_v \hat{f}_k}{\omega/k - v} \tag{B.46}$$

Where $\omega_p = \sqrt{4\pi n_0 q^2/m}$ is the plasma frequency.

For a Maxwellian distribution,

$$\hat{f} = \left(\frac{1}{\pi v_{th}^2}\right)^{1/2} \exp(-v^2/v_{th}^2) \tag{B.47}$$

Where $v_{th} \equiv \sqrt{2k_b T/m}$ is the thermal velocity.

Thus, for species s, the susceptibility χ_s can be written as:

$$\begin{aligned} \chi_s &= \frac{\omega_{p,s}^2}{k^2} \frac{2}{\sqrt{\pi}} \int_{-\infty}^{\infty} dv \frac{v_{th,s}^{-3} v \exp(-v^2/v_{th,s}^2)}{v-\omega/k} \\ \chi_s &= \frac{\omega_{p,s}^2}{k^2 v_{th,s}^2} \frac{2}{\sqrt{\pi}} \int_{-\infty}^{\infty} dx \frac{x e^{-x^2}}{x-\omega/(k v_{th,s})} \end{aligned} \tag{B.48}$$

Here, we have made the substitution $x = v/v_{th}$. Simplifying, we get:

$$\chi_s = \frac{1}{\lambda_D^2 k^2} \left(\frac{n_{0,s} q_s^2 T_e}{n_{0,e} e^2 T_i} \right) w\left(\frac{\omega}{k v_{th,s}} \right) \tag{B.49}$$

Where:

$$w(z_0) \equiv \frac{1}{\sqrt{\pi}} \int_{-\infty}^{\infty} dz \frac{z e^{-z^2}}{z - z_0} \tag{B.50}$$

And $\lambda_D = \sqrt{k_b T_e/(4\pi n_{e,0} e^2)}$ is the Debye length. Here, $n_{s,0}$ is the unperturbed density of charged species s. For electro-neutrality to hold $n_{0,s}/n_{0,e} = e/q_s$, so we can simplify Equation B.49 as:

$$\chi_s = \frac{1}{(\lambda_D k)^2} \left(\frac{Z_s T_e}{T_i} \right) w\left(\frac{\omega}{k v_{th,s}} \right) \tag{B.51}$$

The function $w(z_0)$ has a simple pole at $z = z_0$, and can be evaluated to be:

$$w(z_0) = 1 + i\sqrt{\pi} z_0 e^{-z_0^2} - 2 z_0 e^{-z_0^2} \int_0^{z_0} e^{z^2} dz = 1 + i\sqrt{\pi} z_0 e^{-z_0^2} - 2 z_0 D_+(z_0) \tag{B.52}$$

Here, $D_+(x)$ is the Dawson function defined as:

$$D_+(x) = e^{-x^2} \int_0^x e^{t^2} dt \tag{B.53}$$

B.4 Thompson Scattering Summary

To summarize, the scattered power spectrum for a non-relativistic, unmagnetized collisionless plasma is a function of the spectral density function $S(\mathbf{k}, \omega)$:

$$\left\langle \frac{d\bar{P}}{d\Omega_s d\omega_s} \right\rangle = \frac{c E_{i0}^2/(4\pi) r_e^2}{2\pi} \left[\hat{\mathbf{s}} \times (\hat{\mathbf{s}} \times \hat{\mathbf{E}}_{\mathbf{io}}) \right]^2 e^{i k_s R} N S(\mathbf{k}, \omega) \tag{B.54}$$

$$S(\mathbf{k},\omega) = \frac{2\pi}{k}\left|1-\frac{\chi_e}{\epsilon}\right|^2 \hat{f}_{eo}\left(\frac{\omega}{k}\right) + \frac{2\pi Z}{k}\left|\frac{\chi_e}{\epsilon}\right|^2 \hat{f}_{io}\left(\frac{\omega}{k}\right) \tag{B.55}$$

The dielectric function ϵ and the electric susceptibilities χ_s are defined as:

$$\chi_s = \frac{1}{(\lambda_D k)^2}\left(\frac{Z_s T_e}{T_i}\right) w\left(\frac{\omega}{k v_{th,s}}\right) \tag{B.56}$$

$$w(z_0) = 1 + i\sqrt{\pi} z_0 e^{-z_0^2} - 2z_0 D_+(z_0) \tag{B.57}$$

$$\epsilon = 1 + \chi_e + \chi_i \tag{B.58}$$

The 1D normalized Maxwellian distribution is:

$$\hat{f}_s = \left(\frac{1}{\pi v_{th,s}^2}\right)^{1/2} \exp(-v^2/v_{th,s}^2) \tag{B.59}$$

$$v_{th,s} = \sqrt{\frac{2k_b T_s}{m_s}} \tag{B.60}$$

The scattering wave vector is:

$$\begin{aligned} \mathbf{k} &= \mathbf{k_s} - \mathbf{k_i} \\ k &= \sqrt{k_i^2 + k_s^2 - 2k_s k_i \cos\theta} \end{aligned} \tag{B.61}$$

The scattering frequency is:

$$\begin{aligned} \omega &= \omega_s - \omega_i \\ \omega_{s,i} &= \sqrt{c^2 k_{i,s}^2 + \omega_{pe}^2} \end{aligned} \tag{B.62}$$

$$\omega_{pe} = \left(\frac{4\pi n e^2}{m_e}\right)^{1/2} \tag{B.63}$$

When the electron fluid is non-stationary and moves with a velocity $\mathbf{V}$, the scattered frequency is Doppler shifted by $\mathbf{V}\cdot\mathbf{k}$. The scattered frequency is then:

$$\omega_s = \sqrt{c^2 k_s^2 + \omega_{pe}^2} + \mathbf{V}\cdot\mathbf{k} \tag{B.64}$$

Bibliography

D. J. Ampleford, C. A. Jennings, G. N. Hall, S. V. Lebedev, S. N. Bland, S. C. Bott, F. Suzuki-Vidal, J. B. Palmer, J. P. Chittenden, M. E. Cuneo, A. Frank, E. G. Blackman, and A. Ciardi. Bow shocks in ablated plasma streams for nested wire array z-pinches: A laboratory astrophysics testbed for radiatively cooled shocks. *Physics of Plasmas*, 17(5):1–7, 2010.

J. D. Anderson. *Fundamentals of Aerodynamics.* Boston: McGraw-Hill, 2001.

B. S. Bauer, V. L. Kantsyrev, N. Le Galloudec, R. Presura, G. S. Sarkisov, A. S. Shlyaptseva, S. Batie, W. Brinsmead, H. Faretto, B. Le Galloudec, A. Oxner, M. Al-Shorman, D. A. Fedin, S. Hansen, and I. Paraschiv. Two-terawatt Zebra z-pinch at the Nevada Terawatt Facility. *Digest of Technical Papers-IEEE International Pulsed Power Conference*, 2(June 2014):1045–1047, 1999.

T. R. Boehly, R. S. Craxton, T. H. Hinterman, J. H. Kelly, T. J. Kessler, S. A. Kumpan, S. A. Letzring, R. L. McCrory, S. F. Morse, W. Seka, S. Skupsky, J. M. Soures, and C. P. Verdon. The upgrade to the OMEGA laser system. *Review of Scientific Instruments*, 66(1):508–510, 1995.

S. C. Bott-Suzuki, L. S. Caballero Bendixsen, S. W. Cordaro, I. C. Blesener, C. L. Hoyt, A. D. Cahill, B. R. Kusse, D. A. Hammer, P. A. Gourdain, C. E. Seyler, J. B. Greenly, J. P. Chittenden, N. Niasse, S. V. Lebedev, and D. J. Ampleford. Investigation of radiative bow-shocks in magnetically accelerated plasma flows. *Physics of Plasmas*, 22(5), 2015.

T. J. M. Boyd and J. J. Sanderson. *The Physics of Plasmas.* Cambridge University Press, 2003.

G. C. Burdiak, S. V. Lebedev, S. N. Bland, T. Clayson, J. Hare, L. Suttle, F. Suzuki-Vidal, D. C. Garcia, J. P. Chittenden, S. Bott-Suzuki, A. Ciardi, A. Frank, and T. S. Lane. The structure of bow shocks formed by the interaction of pulsed-power driven magnetised plasma flows with conducting obstacles. *Physics of Plasmas*, 24(7), 2017.

F. F. Chen. *Introduction to plasma physics.* New York: Plenum Press, 1974.

G. Chen. *Nanoscale Energy Transport and Conversion: A Parallel Treatment of Electrons, Molecules, Phonons, and Photons.* MIT-Pappalardo Series in Mechanical Engineering. Oxford University Press, 2005.

M. Chiaberge. Merging galaxies break radio silence, 2015.

J. P. Chittenden and C. A. Jennings. Development of instabilities in wire-array Z pinches. *Physical Review Letters*, 101(5):1–4, 2008.

J. P. Chittenden, S. V. Lebedev, B. V. Oliver, E. P. Yu, and M. E. Cuneo. Equilibrium flow structures and scaling of implosion trajectories in wire array Z pinches. *Physics of Plasmas*, 11(3):1118–1127, 2004.

J. P. Chittenden, B. D. Appelbe, F. Manke, K. McGlinchey, and N. P. Niasse. Signatures of asymmetry in neutron spectra and images predicted by three-dimensional radiation hydrodynamics simulations of indirect drive implosions. *Physics of Plasmas*, 23(5), 2016.

E. Choi, P. J. Wiita, and D. Ryu. Hydrodynamic Interactions of Relativistic Extragalactic Jets with Dense Clouds. *The Astrophysical Journal*, 655(2):769–780, 2007.

A. Davidhazy. An Overview of High Speed Photographic Imaging. 2015.

H. De Sterck and S. Poedts. Intermediate shocks in three-dimensional magnetohydrodynamic bow-shock flows with multiple interacting shock fronts. *Physical Review Letters*, 84(24):5524–5527, 2000.

H. De Sterck, B. C. Low, and S. Poedts. Complex magnetohydrodynamic bow shock topology in field-aligned low-β flow around a perfectly conducting cylinder. *Physics of Plasmas*, 5(11):4015–4027, 1998.

C. Deeney, T. J. Nash, R. B. Spielman, J. F. Seaman, G. C. Chandler, K. W. Struve, J. L. Porter, W. A. Stygar, J. S. McGurn, D. O. Jobe, T. L. Gilliland, J. A. Torres, M. F. Vargas, L. E. Ruggles, S. Breeze, R. C. Mock, M. R. Douglas, D. L. Fehl, D. H. McDaniel, M. K. Matzen, D. L. Peterson, W. Matuska, N. F. Roderick, and J. J. MacFarlane. Power enhancement by increasing the initial array radius and wire number of tungsten [Formula Presented] pinches. *Physical Review E - Statistical Physics, Plasmas, Fluids, and Related Interdisciplinary Topics*, 56(5):5945–5958, 1997.

R. Drake. *High-Energy-Density Physics. Fundamentals, Inertial Fusion and Experimental Analysis.* 2013.

R. P. Drake, S. G. Glendinning, K. Estabrook, B. A. Remington, R. McCray, R. J. Wallace, L. J. Suter, T. B. Smith, J. J. Carroll, R. A. London, and E. Liang. Observation of forward shocks and stagnated ejecta driven by high-energy-density plasma flow. *Physical Review Letters*, 81(10):2068–2071, 1998.

G. C. Duncan and P. A. Hughes. Simulations of relativistic extragalactic jets. *The Astrophysical Journal*, 436:L119, 1994.

J. M. Foster, B. H. Wilde, P. A. Rosen, R. J. R. Williams, B. E. Blue, R. F. Coker, R. P. Drake, A. Frank, P. A. Keiter, A. M. Khokhlov, J. P. Knauer, and T. S. Perry. High-Energy-Density Laboratory Astrophysics Studies of Jets and Bow Shocks. *The Astrophysical Journal*, 634(1):L77–L80, 2005.

J. P. Freidberg. *Ideal MHD.* Cambridge University Press, 2014.

J. L. Giuliani and R. J. Commisso. A Review of the Gas-Puff Z-Pinch as an X-Ray and Neutron Source. *IEEE Transactions on Plasma Science*, 43(8):2385–2453, 2015.

J. P. Goedbloed, R. Keppens, and S. Poedts. *Advanced Magnetohydrodynamics: With Applications to Laboratory and Astrophysical Plasmas.* Cambridge University Press, 2010.

E. Goldstein, M. L. Goldstein, J. T. Gosling, E. W. Greenstadt, C. A. Gurgiolo, T. Hada, J. D. Huba, K. Hudson, J. R. Kan, P. J. Kellogg, A. J. Lazarus, M. A. Lee, R. P. Lepping, R. P. Lin, K. Papadopoulos, G. K. Parks, G. Paschmann, K. B. Quest, P. Rodriguez, C. T. Russell, J. A. V. Allen, K. P. Wenzel, R. T. Woo, and C. S. W. The. A Quarter Century of Collisionless Shock Research. 1984.

M. G. Haines, E. G. Blackman, and T. Gardiner. Laboratory astrophysics and collimates stellar outflows: The production of radiatively cooled hypsersonic plasm ajets. *The Astrophysical Journal, 564 : 113È119, 2002 January 1 (2002.*, 1:113–119, 2002.

M. G. Haines, T. W. Sanford, and V. P. Smirnov. Wire-array z-pinch: A powerful x-ray source for ICF. *Plasma Physics and Controlled Fusion*, 47(12 B), 2005.

J. Hare, G. Burdiak, S. Bland, J. Clayson, T; Halliday, S. Merlini, D. Russell, R. Smith, N. Stuart, L. Suttle, E. Tubman, and S. Lebedev. Generating and diagnosing turbulence in pulsed-power driven magnetised plasmas. *Proceedings of the 62nd Annual Meeting of the APS Division of Plasma Physics*, 2020.

J. D. Hare, L. G. Suttle, S. V. Lebedev, N. F. Loureiro, A. Ciardi, J. P. Chittenden, T. Clayson, S. J. Eardley, C. Garcia, J. W. Halliday, T. Robinson, R. A. Smith, N. Stuart, F. Suzuki-Vidal, and E. R. Tubman. An experimental platform for pulsed-power driven magnetic reconnection. *Physics of Plasmas*, 25(5), 2018.

J. D. Hare, J. MacDonald, S. N. Bland, J. Dranczewski, J. W. Halliday, S. V. Lebedev, L. G. Suttle, E. R. Tubman, and W. Rozmus. Two-colour interferometry and Thomson scattering measurements of a plasma gun. *Plasma Physics and Controlled Fusion*, 61(8), 2019.

P. Hartigan, J. Raymond, and J. Meaburn. Observations and shock models of the jet and Herbig-Haro objects HH 46/47. *The Astrophysical Journal*, 362:624, 1990.

A. J. Harvey-Thompson, S. V. Lebedev, S. N. Bland, J. P. Chittenden, G. N. Hall, A. Marocchino, F. Suzuki-Vidal, S. C. Bott, J. B. Palmer, and C. Ning. Quantitative analysis of plasma ablation using inverse wire array Z pinches. *Physics of Plasmas*, 16(2), 2009.

A. J. Harvey-Thompson, S. V. Lebedev, S. Patankar, S. N. Bland, G. Burdiak, J. P. Chittenden, A. Colaitis, P. De Grouchy, G. N. Hall, E. Khoory, M. Hohenberger, L. Pickworth,

F. Suzuki-Vidal, R. A. Smith, J. Skidmore, L. Suttle, and G. F. Swadling. Optical Thomson scattering measurements of cylindrical wire array parameters. *Physics of Plasmas*, 19(5):1–11, 2012.

J. Huba. A plasma formulary for physics, technology, and astrophysics. *IEEE Electrical Insulation Magazine*, (1), 2013.

I. H. Hutchinson. *Principles of Plasma Diagnostics*. 2002.

J. Kane, D. Arnett, B. A. Remington, S. G. Glendinning, G. Bazan, R. P. Drake, B. A. Fryxell, R. Teyssier, and K. Moore. Scaling supernova hydrodynamics to the laboratory. *Physics of Plasmas*, 6(5 I):2065–2071, 1999.

P. K. Kundu, I. M. Cohen, and D. R. Dowling, editors. *Chapter 15 - Compressible Flow*. Academic Press, Boston, fifth edition edition, 2012.

S. V. Lebedev, R. Aliaga-Rossel, S. N. Bland, J. P. Chittenden, A. E. Dangor, M. G. Haines, and I. H. Mitchell. The dynamics of wire array Z-pinch implosions. *Physics of Plasmas*, 6(5 I):2016–2022, 1999.

S. V. Lebedev, F. N. Beg, S. N. Bland, J. P. Chittenden, A. E. Dangor, M. G. Haines, K. H. Kwek, S. A. Pikuz, and T. A. Shelkovenko. Effect of discrete wires on the implosion dynamics of wire array Z pinches. *Physics of Plasmas*, 8(8):3734–3747, 2001.

S. V. Lebedev, J. P. Chittenden, F. N. , Beg, S. N. Bland, C. A, A. D, H. S, M. G. Haines, E. G. Blackman, and T. Gardiner. The Astrophysical Journal, 564 : 113E119, 2002 January 1 (2002. 1:113–119, 2002.

S. V. Lebedev, D. J. Ampleford, S. N. Bland, S. C. Bott, J. P. Chittenden, J. Goyer, C. Jennings, M. G. Haines, G. N. Hall, D. A. Hammer, J. B. Palmer, S. A. Pikuz, T. A. Shelkovenko, and T. Christoudias. Physics of wire array Z-pinch implosions: Experiments at Imperial College. *Plasma Physics and Controlled Fusion*, 47(5 A), 2005.

S. V. Lebedev, L. Suttle, G. F. Swadling, M. Bennett, S. N. Bland, G. C. Burdiak, D. Burgess, J. P. Chittenden, A. Ciardi, A. Clemens, P. De Grouchy, G. N. Hall, J. D. Hare, N. Kalmoni, N. Niasse, S. Patankar, L. Sheng, R. A. Smith, F. Suzuki-Vidal, J. Yuan, A. Frank, E. G. Blackman, and R. P. Drake. The formation of reverse shocks in magnetized high energy density supersonic plasma flows. *Physics of Plasmas*, 21(5), 2014.

S. V. Lebedev, A. Frank, and D. D. Ryutov. Exploring astrophysics-relevant magnetohydrodynamics with pulsed-power laboratory facilities. *Reviews of Modern Physics*, 91 (2):25002, 2019.

R. D. McBride, W. A. Stygar, M. E. Cuneo, D. B. Sinars, M. G. Mazarakis, J. J. Leckbee, M. E. Savage, B. T. Hutsel, J. D. Douglass, M. L. Kiefer, B. V. Oliver, G. R. Laity, M. R. Gomez, D. A. Yager-Elorriaga, S. G. Patel, B. M. Kovalchuk, A. A. Kim, P. A. Gourdain, S. N. Bland, S. Portillo, S. C. Bott-Suzuki, F. N. Beg, Y. Maron, R. B. Spielman, D. V. Rose, D. R. Welch, J. C. Zier, J. W. Schumer, J. B. Greenly, A. M. Covington, A. M. Steiner, P. C. Campbell,

S. M. Miller, J. M. Woolstrum, N. B. Ramey, A. P. Shah, B. J. Sporer, N. M. Jordan, Y. Y. Lau, and R. M. Gilgenbach. A Primer on Pulsed Power and Linear Transformer Drivers for High Energy Density Physics Applications. *IEEE Transactions on Plasma Science*, 46(11):3928–3967, 2018.

C. W. Mendel, D. B. Seidel, and S. E. Rosenthal. A simple theory of magnetic insulation from basic physical considerations. *Laser and Particle Beams*, 1(3):311–320, 1983.

G. Miley. The Structure of Extended Extragalactic Sources. (1966):165–218, 1980.

G. H. Miller, E. I. Moses, and C. R. Wuest. The National Ignition Facility: Enabling fusion ignition for the 21st century. *Nuclear Fusion*, 44(12), 2004.

I. H. Mitchell, J. M. Bayley, J. P. Chittenden, J. F. Worley, A. E. Dangor, M. G. Haines, and P. Choi. A high impedance mega-ampere generator for fiber z-pinch experiments. *Review of Scientific Instruments*, 67(4):1533–1541, 1996.

M. Moran, H. Shapiro, D. Boettner, and M. Bailey. *Fundamentals of Engineering Thermodynamics*. Wiley, 2010.

B. Nasini. Hubble Snaps Speedy Star Jets, 2021.

S. M. Petrinec and C. T. Russell. Hydrodynamic and MHD equations across the bow shock and along the surfaces of planetary obstacles. *Space Science Reviews*, 79(3-4): 757–791, 1997.

B. A. Remington, J. Kane, R. P. Drake, S. G. Glendinning, K. Estabrook, R. London, J. Castor, R. J. Wallace, D. Arnett, E. Liang, R. McCray, A. Rubenchik, and B. Fryxell. Supernova hydrodynamics experiments on the Nova laser. *Physics of Plasmas*, 4(5 /2): 1994–2003, 1997.

B. A. Remington, R. P. Drake, and D. D. Ryutov. Experimental astrophysics with high power lasers and Z pinches. *Reviews of Modern Physics*, 78(3):755–807, 2006.

H. F. Robey, T. S. Perry, R. I. Klein, J. O. Kane, J. A. Greenough, and T. R. Boehly. Experimental investigation of the three-dimensional interaction of a strong shock with a spherical density inhomogeneity. *Physical Review Letters*, 89(8):085001/1–085001/4, 2002.

C. Russel. Planetary Bow Shocks. *Collisionless Shocks in the Heliosphere: Reviews of Current Research*, (1), 1985.

D. D. Ryutov. The physics of fast Z pinches. *Reviews of Modern Physics*, 72(1):168, 2000.

J. Sheffield, D. Froula, S. H. Glenzer, and N. C. L. Jr. *Plasma Scattering of Electromagnetic Radiation, Second Edition - Theory and Measurement Techniques*. 2010.

D. B. Sinars, M. A. Sweeney, C. S. Alexander, D. J. Ampleford, T. Ao, J. P. Apruzese, and et al. Review of pulsed power-driven high energy density physics research on Z at Sandia. *Physics of Plasmas*, 27(7), 2020.

D. L. Smith, P. Ingwersen, L. F. Bennett, J. D. Boyes, D. E. Anderson, J. B. Greenly, R. N. Sudan, and D. A. Hammer. COBRA accelerator pulsed-power driver for Cornell/Sandia ICF research. *Digest of Technical Papers-IEEE International Pulsed Power Conference*, 2(August):1449–1454, 1995.

M. Smith and C. Norman. Extrastellar Jets - Trajectories. *Royal Astronomical Society*, pages 148–162, 1981.

M. D. Smith. *Astrophysical Jets and Beams.* 2012.

M. D. Smith, T. Khanzadyan, and C. J. Davis. Anatomy of the Herbig – Haro object HH7 bow shock. *Royal Astronomical Society*, 536:524–536, 2003.

J. R. Spreiter and A. Y. Alksne. Plasma flow around the magnetosphere. *Reviews of Geophysics*, 7(1-2):11–50, 1969.

J. R. Spreiter and S. S. Stahara. Magnetohydrodynamic and gasdynamic theories for planetary bow waves. *Collisionless Shocks in the Heliosphere: Reviews of Current Research*, (1):85–107, 1985.

L. G. Suttle, G. C. Burdiak, C. L. Cheung, T. Clayson, J. W. D. Halliday, J. D. Hare, S. Rusli, D. R. Russell, E. R. Tubman, A. Ciardi, N. F. Loureiro, J. Li, A. Frank, and S. V. Lebedev. Interactions of magnetized plasma flows in pulsed-power driven experiments. *Plasma Physics and Controlled Fusion*, 62(1):014020, dec 2019.

L. G. Suttle, J. D. Hare, J. W. Halliday, S. Merlini, D. R. Russell, E. R. Tubman, V. Valenzuela-Villaseca, W. Rozmus, C. Bruulsema, and S. V. Lebedev. Collective optical Thomson scattering in pulsed-power driven high energy density physics experiments (invited). *Review of Scientific Instruments*, 92(3), 2021.

F. Suzuki-Vidal, S. V. Lebedev, M. Krishnan, M. Bocchi, J. Skidmore, G. Swadling, A. J. Harvey-Thompson, G. Burdiak, P. De Grouchy, L. Pickworth, L. Suttle, S. N. Bland, J. P. Chittenden, G. N. Hall, E. Khoory, K. Wilson-Elliot, R. E. Madden, A. Ciardi, and A. Frank. Laboratory astrophysics experiments studying hydrodynamic and magnetically-driven plasma jets. *Journal of Physics: Conference Series*, 370(1), 2012.

F. Suzuki-Vidal, S. V. Lebedev, M. Krishnan, J. Skidmore, G. F. Swadling, M. Bocchi, A. J. Harvey-Thompson, S. Patankar, G. C. Burdiak, P. de Grouchy, L. Pickworth, S. J. Stafford, L. Suttle, M. Bennett, S. N. Bland, J. P. Chittenden, G. N. Hall, E. Khoory, R. A. Smith, A. Ciardi, A. Frank, R. E. Madden, K. Wilson-Elliot, and P. Coleman. Interaction of radiatively cooled plasma jets with neutral gases for laboratory astrophysics studies. *High Energy Density Physics*, 9(1):141–147, 2013.

F. Suzuki-Vidal, S. V. Lebedev, A. Ciardi, L. A. Pickworth, R. Rodriguez, J. M. Gil, G. Espinosa, P. Hartigan, G. F. Swadling, J. Skidmore, G. N. Hall, M. Bennett, S. N. Bland, G. Burdiak, P. De Grouchy, J. Music, L. Suttle, E. Hansen, and A. Frank. Bow shock fragmentation driven by a thermal instability in laboratory astrophysics experiments. *Astrophysical Journal*, 815(2):96, 2015.

G. F. Swadling, S. V. Lebedev, N. Niasse, J. P. Chittenden, G. N. Hall, F. Suzuki-Vidal, G. Burdiak, A. J. Harvey-Thompson, S. N. Bland, P. De Grouchy, E. Khoory, L. Pickworth, J. Skidmore, and L. Suttle. Oblique shock structures formed during the ablation phase of aluminium wire array z-pinches. *Physics of Plasmas*, 20(2), 2013.

M. D. Van Dyke. The Supersonic Blunt-Body Problem - Review and Extension. *Journal of the Aerospace Sciences*, 25(8):485–496, 1958.

M. Verigin, J. Slavin, A. Szabo, G. Kotova, and T. Gombosi. Planetary bow shocks : Asymptotic MHD Mach cones. (1):33–38, 2003.